Dissertation

submitted to the

Combined Faculties for the Natural Sciences and for Mathematics

of the Ruperto-Carola University of Heidelberg, Germany

for the degree of

Doctor of the Natural Sciences

put forward by

M.Sc. Christian Meyer

born in Mönchengladbach

Oral examination: 17.04.2018

The lowest rotational quantum states of hydroxyl anions probed by electron photodetachment in a cryogenic storage ring

Christian Meyer

Referees:

Prof. Dr. Andreas Wolf

Prof. Dr. Matthias Weidemüller

Die tiefsten Quantenzustände der Rotation in Hydroxylanionen untersucht durch photoinduzierte Elektronablösung in einem Tieftemperatur-Speichering:

Der elektrostatische Tieftemperatur-Speichering [32] in Heidelberg bietet eine Umgebung, in der Ionen-Strahlen bis zu Stunden unter interstellaren Bedingungen gespeichert werden können. Ein niedriger Strahlungshintergrund und eine Restgasteilchendichte von < 140 cm^{-3} werden erreicht, indem die experimentellen Kammern des Tieftemperatur-Speicherings mit flüssigem Helium auf 6 K abgekühlt werden. In einer solchen Umgebung kühlen intern angeregte infrarot-aktive Moleküle durch Photonenabstrahlung in ihre tiefsten Rotations- und Vibrationsniveaus. Das Strahlungskühlen eines Rotations-angeregten OH^--Strahls bei 60 keV wird nahe der photoinduzierten Elektronablösungsschwelle untersucht. Hiermit werden Strahlungslebensdauern der niedrigsten Rotationszustände $(193(3)_{\text{stat}}(3)_{\text{sys}}$ s für $J = 1)$ durch exponentielle Zerfälle gemessen und Übergangsdipolmomente bestimmt. Theoretische Berechnungen [84, 90] für das Übergangsdipolmoment im Vibrationsgrundzustand weichen ungefähr $(7 \pm 1)\%$ vom experimentellen Wert $d_{v=0} = 0.971(10)$ D ab. Die Korrelation zwischen den Rotationsenergieniveaus und deren entsprechende Strahlungslebensdauern wird verwendet, um die Besetzung der einzelnen Niveaus und deren Wirkungsquerschnitt bei Elektronenablösung zu bestimmen. Im stationären Zustand wird ein intern kalter OH^--Strahl mit mehr als 90% der Besetzung im Rotationsgrundzustand erreicht. Dies entspricht einer effektiven internen Temperatur von 15 K.

The lowest rotational quantum states of hydroxyl anions probed by electron photodetachment in a cryogenic storage ring:

The Heidelberg electrostatic Cryogenic Storage Ring (CSR) [32] provides an environment for storing ion beams up to hours under interstellar conditions. A low radiative background and a residual particle density of < 140 cm^{-3} is achieved by cooling the experimental chambers of the CSR down to 6 K by liquid helium. In such an environment internally excited infrared-active molecules cool to their lowest rovibrational levels by emitting photons. The radiative cooling of a rotationally hot OH^- beam at 60 keV is probed by near-threshold photodetachment. Thereby the radiative lifetimes of the lowest rotational states $(193(3)_{\text{stat}}(3)_{\text{sys}}$ s for $J = 1)$ are measured directly by the exponential decays and the rotational transition dipole moment is determined. Calculations [84, 90] for the transition dipole moment in the vibrational ground state deviate about $(7 \pm 1)\%$ from the experimental value of $d_{v=0} = 0.971(10)$ D. The correlation between the rotational energy levels and their corresponding radiative lifetimes is used to reveal the individual level populations and their relative photodetachment cross sections. In the steady state an internally cold OH^- beam is reached with more than 90% of the population in the rovibrational ground state, corresponding to an effective internal temperature of 15 K.

Contents

Abbreviations

COMPACT	COld Movable PArticle CounTer
CSR	Cryogenic Storage Ring
CTF	Cryogenic Trap for Fast ion beams
CW	Continuous Wave
DESIREE	Double ElectroStatic Ion-Ring ExpEriment
EA	Electron Affinity
FWHM	Full Width at Half Maximum
MCP	Multi-Channel Plate
MISS	Middleton Ion Sputter Source
MPIK	Max-Planck-Institut für Kernphysik
NICE	Neutral Imaging in Cold Environment
OPO	Optical Parameteric Oszillator
RICE	RIKEN Cryogenic Electrostatic ring

1 Anions and cold molecules: an overview

This chapter gives an overview about the production, probing techniques and physical applications of molecular anions in their lowest rovibrational quantum states. We start with the methods to cool molecules to temperatures of a few Kelvin (see section 1.1). Molecules in this temperature regime are ideal to study chemical reactions under insterstellar conditions. The next section 1.2 motivates the cooling of molecules by explaining the formation and destruction pathways of molecular anions in interstellar space.

In contrast to cations and neutrals the outer electron in anions is bound by a shallow binding potential. The resulting molecular properties of anions are explained in the section 1.3. In many molecules the covalent binding between the atoms is affected to a rather low extent by the additional electron bound to the neutral. In these cases photons can directly detach the electron and neutralize the molecule. At the threshold photon energy, the detachment process becomes highly sensitive to the rotational excitation of molecular anions. Thus, the internal states of molecular anions become accessible for laser diagnostic methods. In this context, section 1.4 deals with the developments in photodetachment spectroscopy.

In order to study molecular processes like the radiative rotational cooling of OH^- it is essential to store molecules as long as possible. We discuss such storage of beams in the current research in section 1.5. In this work we focus on beam storage in space free from matter and radiation using an electrostatic cryogenic storage ring. Hence, in the last section 1.6 we give an overview about the development in the field of electrostatic storage devices and their applications.

1.1 Cooling atoms and molecules

Cooling means controlling the degrees of freedom of a particle ensemble. Cold atoms and molecules have lead to rapid advances in various physical fields: atomic, molecular and optical physics, chemistry, quantum information science, condensed matter physics, nuclear physics and astrophysics [17]. Due to large energy splittings between the lowest electronic states, atoms are normally not excited at room temperature. Hence, the temperature in atomic ensembles is defined by its velocity spread. The velocity distribution can be reduced for example by laser cooling

[69, 16, 57], by evaporative cooling or even by acceleration like in fast-beam laser spectroscopy experiments (e.g. Collaps at CERN [2]).

But in order to get cold molecules we have to cool the internal degrees of freedom: the vibrations and rotations. In comparison to atoms, molecules are more complex, but in particular cold molecules introduce many new research options [22]. Nevertheless the achievement of laser cooling of the first diatomic molecule had to wait until the year 2010 [80]. Still a large set of molecules can not directly be cooled by laser light. Thus, the internal temperature in a molecular ensemble is often reduced by inelastic collisions with other particles. Temperatures down to ∼20 K are reached by cooling the molecules with cold helium buffer gas in a radiofrequency trap [65]. Letting the molecules collide with laser cooled atoms, molecular temperatures below 1 K have been achieved (sympathetic laser cooling) [64]. But exothermic reactions between the coolant and the molecule can inhibit the cooling process [21], which is especially the case for many anions. The temperatures reached by collisional cooling are of the order of a few Kelvin and thus comparable to those measured in interstellar clouds. Internal and external temperature in the same molecular ensemble in space as well as in experiments are not necessarily equivalent. For this reason, the optimal experimental setup for laboratory astrochemistry allows to cool the molecular rotations and vibrations independent of its kinetic energy.

The new cryogenic storage rings [32, 60, 76] support - opposed to many types of ion traps - a way to cool the internal degrees of freedom in a matter-free environment. Due to a low radiative background and long storage times in such devices infrared-active molecules lower their internal temperature to a few Kelvin by emitting photons. Hence the population distribution of the molecular ensemble changes during the cool down. The internal temperature dependence for molecular reactions can be determined by monitoring the corresponding rates over time. Furthermore the kinetic temperature in a molecular ensemble can be controlled separately by acceleration and in the Cryogenic Storage Ring by means of the electron cooler [86]. In comparison to the collisional cooling the new storage rings provide a method to study molecular reactions under vacuum condition, closely reflecting a low-density astrophysical environment.

1.2 Laboratory astrochemistry

Astrochemistry aims at explaining the formation and the abundance of molecules in the interstellar medium [82]. Since interstellar clouds (99% gaseous) [28] are not accessible, the molecular species are identified by spectrometry and molecular processes are combined to large chemical models to calculate abundances in such environments. Thus it is crucial to know reaction rate coefficients. Low densities of 1 to 500 particles per cm^3 and temperatures of a few Kelvin [82] lead to an

unusual chemistry in interstellar clouds. Hence room temperature measurements can lead to erroneous conclusions [28], when using the Arrhenius equation to model the temperature T effects in reaction rate coefficients $k(T)$ [82]. Thus laboratory astrochemistry tries to measure molecular processes under interstellar conditions.

To obtain molecules of a few Kelvin they can be produced in an expansion source or cooled by collisions after production. The resulting molecular *kinetic* temperature of ions, on the one hand, can be measured by the Doppler profile of narrow spectral lines in traps [74] or, in anion beams, by Doppler broadening of the photodetachment threshold (see, e.g. figure 5 in [83]). *Internal* temperatures in molecules on the other hand are determined in the interstellar medium by comparing the strength of rotational transition lines [82]. There, Einstein coefficients and thus transition dipole moments are needed to reveal the rotational population distribution. Calculations of molecular transition dipole moments are assumed to reach precisions of several percent [82], but theoretical results have rarely been confirmed by experiment. Only very recently, the first direct measurements on the dipole moment have been performed for pure rotational transitions [54, 75].

In order to induce reaction rates, stored molecules collide in experiments with photons, electrons and other particles. Even though in interstellar chemistry, gas phase reactions of cations and neutrals play a crucial role, also anions were recently found in interstellar space. Anions can be easily destroyed by radiation. Nevertheless, the first anion C_6H^- has been detected in 2006 [51]. The smallest observed anion in space is the closed shell molecule CN^- [1]. All detected ions have in common that the Electron Affinity of their corresponding neutral is rather large. CN^- can be formed in dense interstellar clouds by charge transfer from polycyclic aromatic hydrocarbons PAH^- to CN. Another important gas phase reaction is the dissociative electron attachment [67]

$$e^- + AB \rightarrow A^- + B. \tag{1.1}$$

But for most species the dissociative electron attachment is an endothermic reaction [67] which is inhibited in cold environments. Thus anions might also be produced by radiative attachment [67]

$$e^- + A \rightarrow A^- + h\nu, \tag{1.2}$$

which is the inverse process of photodetachment. For this reason photodetachment measurements may be used to infer reaction rates for radiative attachment.

Today molecular ion beams can be stored in cryogenic electrostatic storage rings like the Cryogenic Storage Ring [32] at the Max-Planck-Institut für Kernphysik (MPIK) in Heidelberg. Such devices provide conditions like in interstellar clouds. Merged beam experiments on cold molecular ions will lead to experimental results, which can directly serve as parameters for modeling the astrochemical processes.

1.3 Anions

Anions are atomic or molecular systems which have an additional electron bound to a neutral particle. While the electrons in neutral atoms and positive ions are bound by the long-range Coulomb field of the core ($V(r) \propto r^{-1}$), the outermost electron in an anion is attracted by electron correlations and by polarizing the electron cloud (polarization potential $V(r) \propto r^{-4}$). The typical shallow potential in atomic anions allows only a limited number of bound electronic states, many simple negative atomic ions have only one electronic bound state. Excited states below the Electron Affinity have been found in C^-, Si^- and Ge^- [6]. But only anions with complex electronic shell structures like in Os^- and La^- have bound electronic states of an opposite-parity electronic configuration and can be considered as a candidate for laser cooling [63, 88].

For molecular anions, additional effects enter through different symmetry properties of the molecular states and the influence of permanent dipole moments. To simplify the picture we focus on diatomic molecules. OH^- molecules have a shift between the center of mass and the center of charge along the binding axis, which results in a static dipole moment [90]. By vibrating, the molecule changes its binding length and thereby its dipole moment. Similarly, the dipole moment changes by rotation of the molecule. Since an oscillating dipole radiates, the molecule can cool its excited rotational and vibrational states by emitting photons. By measuring radiative lifetimes of the internal molecular states we determine the Einstein coefficient and thus the transition dipole moment, which depends also on the electronic configuration. If we compare the neutral OH with the OH^- anion, the binding length and thus the position of the atomic cores remains nearly unchanged [10], but the dipole moment varies significantly [84, 90]. Hence, the additional electron in the OH^- changes in first approximation only the charge configuration in the electron shell. By this, the transition dipole moment is a sensitive quantity to test electron correlation in theoretical calculations. The implementation of electron correlations in molecular and atomic calculation can be quite challenging. We find in this thesis differences of the order of 7% between the theoretical values for OH^- dipole moment [84] and experimental results.

In the interstellar space anions like C_6H^- [51] have been found, although most anions can be easily neutralized by radiation. Absolute photodetachment cross sections are needed to model anionic abundances in interstellar space by formation and destruction processes. Absolute experimental photodetachment cross sections for many anions are often linked by normalization to the O^- anion [40]. Thus, absolute cross sections for the O^- anion have been measured to a rather large extent [11, 40, 49]. The photodetachment process itself has simplified the probing of molecular processes in-vacuo and has lead to a large variety of applications for anions in ion physics experiments (see section 1.4).

1.4 Photodetachment

Classically the interaction between photons and matter is studied by observing the absorption spectra. In order to obtain a sufficient signal the particle density in the interaction zone has to be rather high compared to ion densities achievable in ion beams. Moreover, in this high density regime particles interact with each other, leading to shifts in measured quantities like the position. To determine the free-space absorption frequency these shifts are calculated by theoretical modeling. Today, line shifts are reduced by measuring for example the absorption spectra of C_{60}^+ and C_{60}^- in a weakly-interacting cold helium matrix [46], but systematic uncertainties still remain. Thus measurement in-vacuo can most directly reflect the properties of isolated systems in free space.

For anions, photon-particle interaction can lead to neutralization by photodetachment of the electron. There the surplus electron of an anion is released by the photo-electric effect. In comparison to photofragmentation or photo-ionization of neutrals and cations, photodetachment cross sections are large and can reach even a few wavenumbers above the threshold photon energies given by the electron affinity with a typical magnitude of 10 to 100 Mb [66]. Already in the 50's, Branscomb measured already the absolute photodetachment cross sections of H^-, D^- and O^- by measuring the electron flux with a collector [12, 11]. He used a lamp at a temperature around 3300 K as a light source in combination with filters to achieve spectral resolution. With such simple experiments he determined also the electron affinity of OH^- and the binding shift between OH^- and OH [10].

The photon energy dependence of a photodetachment transition is often described by the Wigner threshold law [92]

$$\sigma \propto (E - E_t)^{l+1/2}, \tag{1.3}$$

where $(E - E_t)$ represents the kinetic energy of the released electron and l is the angular momentum of its partial wave. For OH^- in the ground state Σ^+ ($l = 0$) the threshold should rise as $(E-E_t)^{0.5}$, but experiments have found threshold exponents of ~ 0.2. This was explained by mixing of Λ doublet states in the OH molecule [26]. Since the Wigner threshold law includes only effects of the longest range potential between the neutral and the electron, the validity of the Wigner threshold law even for atomic anions depends on the strength of short range interactions like dipole polarizability, which are rather large in Li and K [72]. Thus more advanced models include multipole forces and polarization, e.g. the modified effective range theory of Watanabe and Green [89]. As a result the threshold behavior carries a lot of information about the interaction between neutral and electron, but needs sophisticated theoretical background to reveal the interaction properties.

Additionally photodetachment spectroscopy can be used to understand the level structure of the anion. Each transition for the anion to the neutral opens up a

threshold in the photodetachment spectrum. By assigning the photodetachment thresholds to their corresponding anionic states we can determine the energy splittings between them [41]. In contrast to atomic anions, molecular negative ions have many populated states at room temperature due to their internal degrees of freedom. Hence, the photodetachment spectrum is more complex, but yields information on the rotational structure. Rotational constants for the OH^- molecule have been determined by resolving the fine structures in the photodetachment spectrum of OH^- [42, 78].

Another way to obtain anionic properties is to measure the kinetic energy of the released electron. Hence, some research groups developed photodetachment experiments employing an electron energy spectrometer [81, 14]. Since the electron is much lighter than the produced neutral particle, the electron carries almost all of the released reaction energy. Hence, photon electron spectroscopy allows to determine the state of the interacting anion. This was applied in various electron affinity measurements on diatomic molecular anions [19, 18, 14]. Another way to measure the electron spectrum is to image the spatial distribution of electrons on a Multi-Channel Plate (MCP) detector [30]. By analyzing the electronic spectrum on the MCP, Goldfarb *et al* [30] determined with high precision the Electron Affinity of the OH and the rotational constants for OH^-. The idea of monitoring the kinetic energy of the electron by the spatial distribution on a MCP detector lead to the first implementation of such a detector in an electrostatic cryogenic ion beam trap [45].

In these studies, photodetachment has been mainly applied to measure molecular parameters. But the strength of the thresholds in the photodetachment spectrum is directly proportional to the populations of the addressed states. Otto *et al* [65] cooled an OH^- ensemble in a 22-pole-trap by helium buffer gas and fitted the near-threshold photodetachment spectrum with transition intensities [79] estimated by the Wigner threshold law to reveal the rotational population distribution. With this technique called rotational state or photodetachment thermometry, Hauser *et al* measured the cross section of cold inelastic rotational collision of OH^- in a helium buffer gas [34].

With the upcoming electrostatic cryogenic storage rings in Stockholm [76], Heidelberg [32] and Tokyo [60], photodetachment became a versatile tool to monitor ion beams for storage times up to hours in collision free environments. For example Bäckström *et al* measured the decay of a metastable state in $^{32}S^-$ ion of 503 ± 54 s lifetime [3]. Furthermore time-resolved photodetachment thermometry discussed in this thesis lead to the first direct measurements of rotational cooling in-vacuo [54] and were recently complemented by depletion studies of rotational levels by photodetachment [75].

Photodetachment has been also applied to more complex quantum systems like clusters to monitor internal cooling processes. The laser excites the anion to a

metastable state which decays by emitting an electron. This process is called delayed photodetachment. The decay rate of the metastable ion changes rapidly with its internal energy. Radiative cooling is observed by changes in the decay rate of the metastable ions. A prominent example is the detection of a low lying electronic state in C_6^- by observing fluorescence decay in the storage ring at Tokyo Metropolitan University [43]. Furthermore cooling of internal degrees of freedom in Co_4^- clusters have been measured by delayed photodetachment in the Cryogenic Trap for Fast ion beams (CTF) at the MPIK [13].

To summarize, photodetachment has evolved from a purely spectroscopic tool for measuring electron affinities and rotational constants to a probing technique which resolves and disentangles decay processes in-vacuo by time-resolved spectroscopy.

1.5 Storage of molecular ions

To study processes and properties of molecular ions they are confined in all three dimensions by magnetic or electric fields. The most common storage device for molecular ions is the radiofrequency trap. In such traps molecules are stored by an oscillating electric multipole field combined with an electrostatic field. Those traps can be applied to a large set of molecules by tuning the offset and amplitude of the oscillating field to a stable orbit [23]. Furthermore ions in a radiofrequency trap can be cooled by buffer gas and exposed to laser light from all directions. The oscillating electric field leads to micromotions of the ions in the trap. By colliding with other particles molecular ions can heat up internally. Thus, many radiofrequency traps have instead of a quadrupole a higher pole (often a 22-pole) field, reducing the micromotion [91]. But still this effect remains.

To cool ions further down magneto-optical traps are used. Here ions are stored by radiation pressure in a magnetic field [69]. To transfer the momentum of the photon to the particle the laser has to address a closed dipole transition. The internal structure in molecules and the non-existence of dipole transitions in many anions makes the type of trap impracticable for molecular anions. Nevertheless molecules can reduce their internal excitation by collisions with laser-cooled atoms [64]. But reactions with the coolant can inhibit the cooling process like dissociative attachment between OH^- and rubidium [21].

Another possibility to store molecular ions are Penning traps. Those are normally used for atomic ion in precision mass measurements, but they have also been applied to molecular ions [24]. But neutral products, e.g. induced by photodetachment, are difficult to detect in Penning traps.

Electrostatic storage devices are another technique for storing molecular ions. In contrast to radiofrequency and magneto-optical traps the kinetic temperature of the

ions is well decoupled from the internal degrees of freedom in the molecule. Thus the next section 1.6 deals with electrostatic storage devices and their application.

1.6 Electrostatic storage devices

Many molecular properties and interactions have been studied in merged beam experiments at magnetic storage rings with an ion energy in the MeV range [73]. Due to the high velocity the energy between the stored and colliding particles can be precisely tuned. Magnetic storage devices are limited by the charge-to-mass ratio of the ions they can store. Thus the options for investigating heavy atoms and molecules in magnetic storage rings are limited. Another important drawback of magnetic storage devices is the presence of magnetic fields that can mix close-lying states with the same magnetic quantum number. By using purely electrostatic fields, the effect of state mixing can be significantly reduced in specific cases [93].

In order to study more complex molecules and to avoid magnetic state mixing, the first electrostatic storage ring was taken in operation at Aarhus in the year 1997 [56]. At almost the same time the first linear electrostatic trap (Zajfman trap) was set up in Israel [94]. Those facilities are already quite compact compared to the former magnetic devices and can store molecules of a given energy independent of their mass. With further advancement the electrostatic storage devices got smaller and more compact [4, 77]. The compact size allowed the research groups in Stockholm and in Tokyo to build up electrostatic rings like the Double ElectroStatic Ion-Ring ExpEriment (DESIREE) [76] and the RIKEN Cryogenic Electrostatic ring (RICE) [60], which are fully contained in an isolation vacuum to cool the experimental chambers to cryogenic temperatures. Thus very low residual gas densities are reached allowing to store ion beams for several hours.

Simultaneously with these developments, the motivation to study internally cold complex molecules in merged beam experiments triggered the construction of the Cryogenic Storage Ring (CSR) at the MPIK in Heidelberg [32]. In contrast to other electrostatic storage devices, ions in the CSR can reach kinetic energies of up to 300 keV to measure reactions with a well-defined collision energy in merged-beams experiments. Similar to the design ideas of other cryogenic storage rings the ultra cold vacuum chambers provide an environment in which infrared-active molecules can cool to the temperature of the surrounding beam enclosure.

In order to test the cooling in cryogenic storage devices a simple, well-studied molecule with a large dipole moment is desired which can be state-selective probed by laser light in a reasonable wavelength range. Due to the related studies described in this thesis, we choose the molecule OH^-.

Chapter 2 introduces the rotational cooling of linear molecules in a broad-band radiation field. Here the photon interactions between rotational states are described

by the Einstein coefficients depending on the corresponding level structure and line intensities. The modeled radiative rates are combined to simulate the rotational cooling. To monitor the decay of the rotational populations the OH^- molecule in the CSR is probed by photodetachment. Thus, chapter 3 describes the process of the electron photodetachment from the electronic ground state of a closed-shell anion into its corresponding neutral molecule. Here the electronic structures of both molecular species are introduced to assign the rotational structures in the photodetachment spectra to the transitions. Furthermore the intensities for photodetachment transitions are calculated and combined with a Wigner-type dependence to model the relative rotational cross section close to the Electron Affinity. To reveal the rotational populations the relative cross sections are measured at various photon energies. Therefore chapter 4 deals with the experimental concept to monitor cross section ratios at multiple wavenumbers over time. The time-structure of the cross section ratios is pre-analyzed and fitted with a combined cooling and probing model. In chapter 5 the fit results are analyzed, revealing radiative lifetimes of rotational states and relative, population-independent photodetachment cross sections. The experimental results are compared to the predicted values in chapter 2 and 3. In chapter 6 the results of this work are discussed with regard to the advances in photodetachment spectroscopy and the potential of cryogenic electrostatic storage devices.

2 Radiative cooling of rotational states in linear molecules

This chapter describes the rotational cooling of linear molecules such as OH^- in broad-band radiation fields. The fundamental interactions between the molecule and the radiation field are explained in detail (see section 2.1). Transition rates depend strongly on the energy splitting between the rotational states. Thus, section 2.2 deals with the rotational structure of a linear molecule. To model the intensities for the rotational transitions the degeneracy of states and the difference between the permanent and the transition dipole moment have to be considered (see section 2.3). The radiative rotational dynamics are analyzed and discussed (see section 2.4).

2.1 Interaction of light with matter

Molecules in-vacuo equilibrate with the environmental radiation field by emitting and absorbing photons. Thus, the measured internal population distribution in equilibrium depends on the photon energy density of the radiative field. In a two-state system (see figure 2.1) only photons which are in resonance with the transition

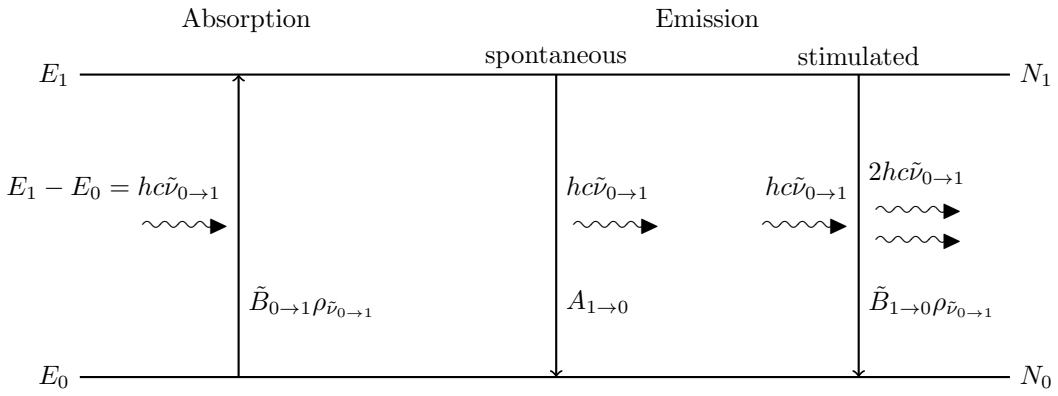

Figure 2.1: The two state system represents the three fundamental photon matter interactions: Absorption and stimulated and spontaneous emission. The transition rates are given by Einstein coefficients $\tilde{B}_{0\to1}$, $\tilde{B}_{1\to0}$, $\tilde{A}_{1\to0}$ (see equation 2.3, 2.4 and 2.5) and the photon energy density $\rho_{\tilde{\nu}_{0\to1}}$ (see equation 2.1) at resonance.

energy $\Delta E = E_1 - E_0 = hc\tilde{\nu}_{0\to1}$ can drive the transition and thereby change the population distribution. In general, quantized systems such as molecules are only sensitive to photons, which are in resonance with one of their transitions. Hence, it is essential to know the photon energy density at those resonant frequencies in the experimental storage device, which is considered as a cavity with rigid opaque walls. Since this thesis deals mostly with spectroscopic properties of molecules the energy scale is chosen to be in wavenumbers (cm^{-1}).

2.1.1 Radiation field in thermal and non-thermal cavities

In a cavity at temperature T (thermal cavity) the radiation field is described by a blackbody emitter. According to Planck the photon spectral energy density is [68]

$$\rho_{\tilde{\nu}} d\tilde{\nu} = \frac{8\pi hc\tilde{\nu}^3}{e^{hc\tilde{\nu}/kT} - 1} d\tilde{\nu}. \tag{2.1}$$

Ideally the cavity itself is thermalized, but local thermal temperature gradients have to be expected. Not only different coupling strengths of the various parts of the experimental beamline with the thermal bath, e.g. the liquid helium reservoir of the closed-cycle refrigeration system, but also openings to the injection beamline at room temperature lead to a position dependent radiative field. Since the oscillation frequency of the molecular ensemble in the storage device is much higher than the radiative transition rate, an effective radiative field described by a linear combination of several blackbody radiators is considered:

$$\rho^{\mathrm{eff}}_{\tilde{\nu}} = \sum_T a_T \rho_{\tilde{\nu}}(T). \tag{2.2}$$

Here the linear coefficients a_T represent the fractions of the different thermal radiation fields.

To understand the effects of combined radiation fields the spectra of non-thermal and thermal cavities are compared (see figure 2.2). The intensity and the range of the spectral energy density is very sensitive to thermal changes (see figure 2.2). If only $a_{300\ \mathrm{K}} = 0.1\%$ of radiation modes are excited according to 300 K, the combined radiation field is dominated by the 300 K radiator across the spectral range only reduced by the linear coefficient $a_{300\ \mathrm{K}}$ (see figure 2.2). Thus, molecular temperatures in such a field depend on the addressed mode in the photon frequency spectrum. For a molecular transition of a few wavenumbers the population ratio agrees in the combined radiation field with a 10 K temperature. But at the crossing of the green and purple line in figure 2.2 the energy density in the combined radiation field matches a thermal distribution at 50 K.

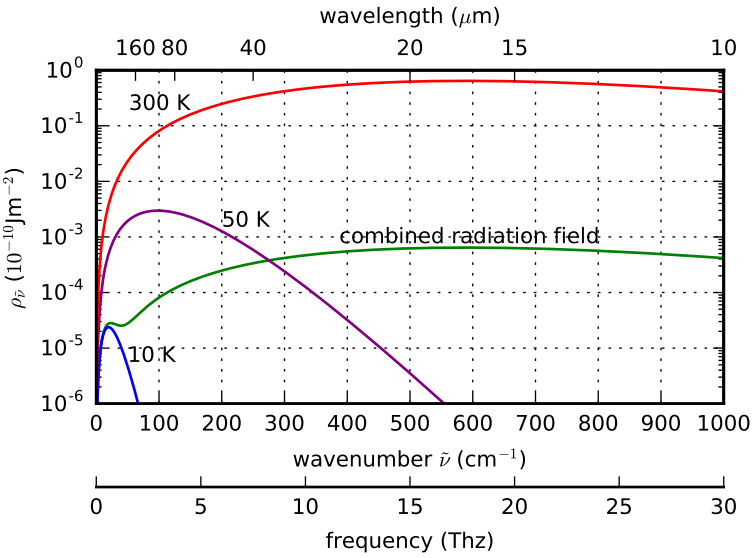

Figure 2.2: The spectral distributions of the photon energy density for thermal cavities at 10 K (blue line), 50 K (purple line) and 300 K (red line) respectively are shown. Additionally a radiation field combined with a 99.9% 10 K and 0.1% 300 K field is included (green line).

2.1.2 Einstein A and B coefficients

Light can change the state of a system in three different manners: absorption, spontaneous emission and stimulated emission. While photon absorption and stimulated emission are driven by an external radiation field, the spontaneous emission is a random process depending only on the atomic or molecular properties. In case of a broad-band radiation field, the processes are described by the Einstein coefficients for absorption, spontaneous emission and stimulated emission. A detailed description can be found in the concise summary by Bernath [5].

A radiative field with the photon spectral energy density $\rho_{\tilde{\nu}_{0\to1}}$ at the resonant frequency $\tilde{\nu}_{0\to1}$ drives a transition from the ground state (0) to the excited state (1). The absorption rate is

$$\left.\frac{dN_1}{dt}\right|_{\text{abs}} = \tilde{B}_{0\to1}\rho_{\tilde{\nu}_{0\to1}}N_0. \tag{2.3}$$

Here the Einstein coefficient of absorption $\tilde{B}_{0\to1}$ represents the coupling strength between the two-state system and the radiation field. Instead of exciting the system by photon absorption the radiative field can also induce a transition from the excited

to the ground state with the stimulated emission rate

$$\left.\frac{dN_1}{dt}\right|_{\text{stim}} = -\tilde{B}_{1\to0}\rho_{\tilde{\nu}_{0\to1}}N_0 \tag{2.4}$$

in which $\tilde{B}_{1\to0}$ is the Einstein coefficient of stimulated emission. Thus, processes induced by the radiative field are described by the Einstein coefficients B, which are equal disregarding a possible degeneracy of states. In the third process an excited state decays by spontaneous emission of a photon with a rate

$$\left.\frac{dN_1}{dt}\right|_{\text{spont}} = -A_{1\to0}N_0. \tag{2.5}$$

Here, $A_{1\to0}$ is defined as the Einstein coefficient for spontaneous emission. Its inverse $\tau_1 = 1/A_{1\to0}$ is the radiative lifetime of the excited state. In the absence of a radiative field the decay of the excited state directly reveals the Einstein coefficient for spontaneous emission. At equilibrium the rates of all three processes are balanced:

$$\frac{dN_1}{dt} = \sum_p \left.\frac{dN_1}{dt}\right|_p = 0, \tag{2.6}$$

where p denotes the processes of absorption, spontaneous and stimulated emission. In radiatively dominated regimes the Einstein coefficients define the population ratio of the states

$$\frac{N_1}{N_0} = \frac{\tilde{B}_{0\to1}\rho_{\tilde{\nu}_{0\to1}}}{A_{1\to0} + \tilde{B}_{1\to0}\rho_{\tilde{\nu}_{0\to1}}}. \tag{2.7}$$

Comparing the state of equilibrium with the Boltzmann distribution

$$\frac{N_1}{N_0} = \frac{g_1}{g_0}e^{-hc\tilde{\nu}_{0\to1}/kT}, \tag{2.8}$$

the energy density in the photon spectrum at thermal equilibrium is defined by

$$\rho_{\tilde{\nu}_{0\to1}} = \frac{A_{1\to0}}{\tilde{B}_{1\to0}}\frac{1}{\frac{\tilde{B}_{0\to1}}{\tilde{B}_{1\to0}}\frac{g_0}{g_1}e^{hc\tilde{\nu}_{0\to1}/kT} - 1}. \tag{2.9}$$

To match the photon energy density distribution of a blackbody radiator (see equation 2.1) the Einstein coefficients need to fulfill the following relations:

$$\frac{\tilde{B}_{0\to1}}{\tilde{B}_{1\to0}} = \frac{g_1}{g_0} \qquad \text{and} \qquad \frac{A_{1\to0}}{\tilde{B}_{1\to0}} = 8\pi hc\tilde{\nu}^3_{0\to1}. \tag{2.10}$$

Thus the lifetime of an excited state can be determined by measuring the absorption rate and vice versa.

The spectral energy density of a blackbody radiator

$$\rho_{\tilde{\nu}} = 8\pi hc\tilde{\nu}^3 n_{\tilde{\nu}} \tag{2.11}$$

can also be written in terms of the photon occupation number $n_{\tilde{\nu}}$ which follows the Bose-Einstein statistics [8]

$$n_{\tilde{\nu}} = \frac{1}{e^{hc\tilde{\nu}/kT} - 1} > 0 \tag{2.12}$$

in quantum gases like blackbody photon radiation fields. Here, the photon occupation number $n_{\tilde{\nu}}$ describes the number of photons in a single mode at frequency $\tilde{\nu}$. The rate constants induced by the radiative field can be written in terms of the Einstein coefficient of spontaneous emission by using the relations 2.10 and equation 2.11:

$$B_{1\to0}\rho_{\tilde{\nu}_{0\to1}} = A_{1\to0}n_{\tilde{\nu}_{0\to1}} \qquad \text{and} \qquad B_{0\to1}\rho_{\tilde{\nu}_{0\to1}} = \frac{g_1}{g_0}A_{1\to0}n_{\tilde{\nu}_{0\to1}}. \tag{2.13}$$

While the Einstein coefficients determine the interaction between a photon and the system, the photon occupation number $n_{\tilde{\nu}}$ quantifies the radiative field. The relations of the Einstein coefficient 2.13 are also valid for non-thermal broad-band radiative fields. Hence the ratio in the steady state is

$$\frac{N_1}{N_0} = \frac{g_1}{g_0}\frac{n_{\tilde{\nu}_{0\to1}}}{1 + n_{\tilde{\nu}_{0\to1}}} < 1, \tag{2.14}$$

which is independent of the photon coupling strength. As a consequence the photon occupation numbers at the corresponding transition frequencies determine the steady state ratios. Furthermore, the molecular system quantizes the relevant photon field spectrum.

To relate the molecular properties to the Einstein coefficients we have to understand the coupling between the electromagnetic waves and the molecule. In weak photon fields molecules couple to photons via their dipole moments. By using perturbation theory Bernath [5] derives the following equation for the Einstein coefficient of spontaneous emission

$$\tilde{A}_{0\to1} = \frac{16\pi^3 d_{10}^2 \tilde{\nu}_{0\to1}^3}{3\epsilon_0 h}. \tag{2.15}$$

Equation 2.15 in combination with the relations 2.10 link the observed rates to the transition dipole moment

$$d_{ij} = \left|\langle\Psi_i|\hat{d}|\Psi_j\rangle\right| = \left|\int \Psi_i^* \hat{d}\Psi_j dV\right| \tag{2.16}$$

of atoms and molecules in a non-polarized light field. Here $\hat{d} = -e\vec{r}$ represents the dipole operator and Ψ_i the wave function of the state i. As a result the photon coupling between two quantum states depends on the transition dipole moment, which is discussed in detail for rotational transitions in section 2.3.

2.1.3 Doppler broadening in electrostatic storage devices

At non-relativistic velocities an object moving at a constant velocity v parallel (-) or anti-parallel (+) to an electromagnetic wave with frequency ν_0 observes a Doppler shifted frequency of

$$\nu_D = \nu_0 \frac{c \pm v}{c}. \tag{2.17}$$

Hence a molecular ensemble with a velocity spread Δv leads to a spectral broadening of the absorption lines. The velocity probability distribution P_v can be transformed into a spectral line shape

$$P_\nu = P_v \frac{dv}{d\nu_D} = \frac{c}{\nu_0} P_v. \tag{2.18}$$

The longitudinal velocity distribution P_v in storage devices can be measured by the frequency spectrum of the Schottky pick-up. In the CSR the Gaussian frequency distribution of a 60 keV Ar^+ beam was observed with a maximal standard deviation of $\sigma_f = 200$ Hz [86]. The frequency broadening at Full Width at Half Maximum (FWHM) $\Delta f = \sqrt{2\ln 2}\sigma_f$ in the Schottky spectrum is connected to the momentum uncertainty Δp by the slip factor η:

$$\frac{\Delta f}{f} = \eta \frac{\Delta p}{p} = \eta \frac{\Delta v}{v}. \tag{2.19}$$

The slip factor for the employed quadrupole settings of the CSR is about $\eta = 0.6$ [31]. With the linear transformation 2.19 the shape of the distribution is conserved. The standard deviation of the longitudinal Gaussian velocity distribution is

$$\sigma_v = \frac{v\sigma_f}{\eta f}. \tag{2.20}$$

in the longitudinal direction. Thus, the velocity spread depends on the mean velocity

$$v = \sqrt{\frac{2E_{kin}}{m}} \tag{2.21}$$

at which the ions are stored. Here E_{kin} is the mean kinetic energy of the ion beam. In the velocity frame of the ions the spectral line shape including Doppler broadening is

$$P_\nu = \frac{1}{\sqrt{2\pi\sigma_{\nu_D}^2}} e^{\left(\frac{\nu-\nu_D}{\sqrt{2}\sigma_{\nu_D}}\right)^2} \text{ with } \frac{\sigma_{\nu_D}}{\nu_0} = \frac{\sigma_v}{c}. \tag{2.22}$$

Since all singly charged molecules are stored with identical settings of the storage ring, the frequency spectrum measured at the Schottky pickup applies to a large number of molecules. Thus the Doppler broadening for a 60 keV OH^- beam can be adapted to

$$\begin{aligned}\frac{\Delta\tilde{\nu}_D}{\tilde{\nu}_0} &= \frac{\Delta\nu_D}{\nu_0} = \sqrt{2\ln 2}\frac{v_0\sigma_f}{c\eta f} \\ &= \sqrt{2\ln 2}\frac{\sqrt{2\cdot 60\text{ keV}}\cdot 200\text{ Hz}}{\sqrt{17\text{ u}}\cdot 0.6\cdot 178\text{ kHz}\cdot\ c} = 3.84\cdot 10^{-7}.\end{aligned} \tag{2.23}$$

For the transition between the lowest rotational states of OH^- ($\tilde{\nu} = 37.5\text{ cm}^{-1}$ $\hat{=}$1.12 Thz, see table 2.1) the maximal transition line Doppler broadening is $\Delta\nu_D =$ 0.43 MHz.

2.1.4 Effects of line shape functions in broad-band radiation fields

Up to now the absorption and emission lines of a molecular ensemble are expected to be infinitesimally small, which is forbidden due to the Heisenberg uncertainty principle [36]. Hence, Einstein coefficients are often folded by a lineshape function.

To determine the shape and the width $\Delta\nu$ of the lineshape the dominating broadening mechanism has to be found. An excited state decaying exponentially with the lifetime τ has a natural lineshape of a Lorentzian function with a FWHM of

$$\Delta\tilde{\nu}_n = \frac{1}{2\pi c\tau} \tag{2.24}$$

in the frequency spectrum [5]. Most rotational transitions in molecules have a natural linewidth below $\Delta\tilde{\nu}_n/c = 1$ Hz, which is negligibly small in comparison to Doppler broadening $\Delta\tilde{\nu}_D = 3.84\cdot 10^{-7}\tilde{\nu}$ at THz photon energies in the CSR (see section 2.1.3). Effects like transit-time and power broadening (see pages 31-34 in [5]) can be disregarded for long interaction times in weak broad-band radiation fields. Pressure broadening (see pages 27-28 in [5]) is absent in a vacuum environment. Thus, the linewidth is dominated by Doppler broadening.

If the spectral intensities of the radiation field are constant over the width of the lineshape, the effect of transition line broadening cancels out in the Einstein coefficients. To approximate the effect of the Doppler lineshape on the transition rates the variation of the photon occupation number (see equation 2.12) is calculated by

$$\frac{\Delta n}{n} = \frac{hc\tilde{\nu}}{kT}\frac{1}{1-e^{-hc\nu/(kT)}}\frac{\Delta\tilde{\nu}}{\tilde{\nu}}. \tag{2.25}$$

For a 10 K blackbody radiation field the absorption rate of the lowest rotational state in OH^- is shifted by only $\frac{\Delta n}{n} \approx 4 \cdot 10^{-6}$. Thus, Einstein coefficients for broad-band radiation fields are often assumed to be constant over the lineshape. For this reason radiative rotational cooling can be modeled without folding the Einstein coefficient with the proper lineshape function.

2.2 Rotational level structure

To model the rotational transition rates the structure and rotational effect of the system have to be analyzed in order to determine the transition energies. Starting with the simplest model of a quantum mechanical rotator (see section 2.2.1) effects such as a varying bond length (see section 2.2.2) are discussed. Both models are limited to cases of a vanishing electronic moment ($^1\Sigma$ state).

2.2.1 Rigid rotator

The simplest model of a quantum mechanical rotator is called the rigid rotator. Here, the masses m_1 and m_2 are point-like particles bonded at a constant length r. In such a model the finite size of atoms and the centrifugal distortion in a diatomic molecule are neglected. Both simplifications are well justified, since the finite size of a nucleus ($\sim 10^{-14}$ m) is around 4 magnitudes smaller than the bond length ($\sim 10^{-10}$ m) and the spring constants of covalent bonds such as for the OH^- molecule are rather strong [5]. The latter one will be discussed later in terms of the derived centrifugal coefficient.

In classical mechanics the rotational energy of a rigid body is given by

$$E_{rot} = \frac{L^2}{2I} = \frac{1}{2} I \omega^2 \tag{2.26}$$

Here $L = I\omega$ is the angular momentum and $I = \sum m_i r_i^2$ is the moment of inertia about the rotating axis with the angular velocity ω. Free molecules rotate about their center of mass

$$S = \sum m_i r_i = 0. \tag{2.27}$$

The distances r_1 and r_2 of the masses m_1 and m_2 to the center of mass (rotating axis) are given by

$$r_1 = \frac{m_2}{m_1 + m_2} r \qquad \text{and} \qquad r_2 = \frac{m_1}{m_1 + m_2} r. \tag{2.28}$$

Combining these relations with the moment of inertia I one obtains

$$I = m_1 r_1 + m_2 r_2 = \frac{m_1 m_2}{m_1 + m_2} r. \tag{2.29}$$

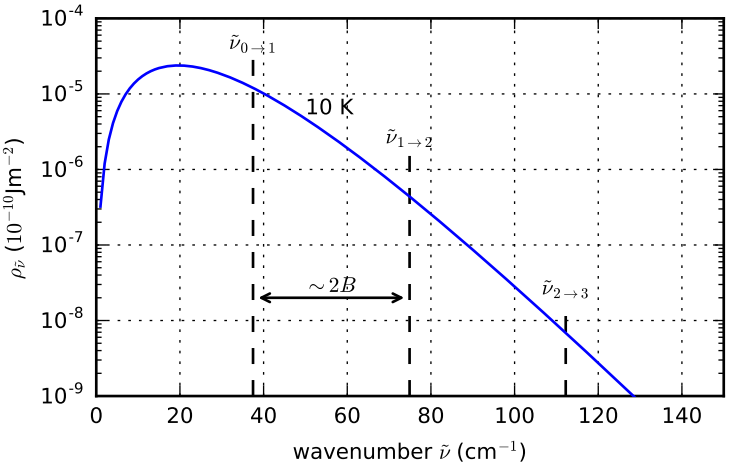

Figure 2.3: Here the spectral distribution of the photon energy density for a thermal cavity at 10 K is shown. The photon frequencies $\tilde{\nu}_{J\to J+1}$ for the lowest three rotational transitions of the OH^- molecule are marked by dashed lines. See figure 2.2 to compare with other thermal radiation fields.

Hence, the rigid rotator has the same energy as a point-like particle with the mass

$$\mu = \frac{m_1 m_2}{m_1 + m_2} \tag{2.30}$$

rotating about at a distance r. μ is often called the reduced mass.

Since the rigid rotator has no potential along the internuclear axis, wave functions are identical to the angular solutions $\Psi_{JM} = Y_{JM}(\theta, \phi)$ (spherical harmonics) of the hydrogen atom. Equivalent to the hydrogen atom the rotational states are characterized by the rotational and magnetic quantum number J and M, respectively. The values of the rotational quantum number are integer numbers $\{0, 1, 2, \cdots\}$ and for each rotational state $2J + 1$ different values of the magnetic quantum number $M \in \{J, J-1, \cdots, -J\}$ exist. To derive the rotational energy levels E_J the Hamiltonian of the rigid rotator is obtained by replacing the angular momentum L with the quantum mechanical operator $\hat{J}$ in equation 2.26 and employing the relation of the spherical harmonics

$$\hat{J} Y_{JM}(\theta, \phi) = \hbar^2 J(J+1) Y_{JM}(\theta, \phi). \tag{2.31}$$

The eigenvalues of the rigid rotator, being the rotational energy levels,

$$E_J = \frac{\hbar^2 J(J+1)}{2I} = \frac{\hbar^2 J(J+1)}{2\mu r^2} \tag{2.32}$$

increase in a good approximation quadratically with increasing J and are independent of the magnetic quantum number M. Thus, each rotational state has a degeneracy of $2J + 1$. The energy splitting of rotational levels

$$\Delta E_J = E_J - E_{J-1} = \frac{\hbar^2 J}{\mu r^2} \tag{2.33}$$

increases linearly with J. Hence, the spectral distance between two adjacent rotational transition lines in molecular spectroscopy is twice the rotational constant

$$B = \frac{\hbar^2}{2\mu r^2} = \frac{\hbar^2}{2I}. \tag{2.34}$$

Thus, rotational transitions in a molecule sample the photon frequency space of the radiative field with a spacing of $2B$ (see figure 2.3). Thus the molecule determines the relevant photon frequencies in the radiation field.

Raman spectroscopy [37] and fine-structure photodetachment spectroscopy [14] are two experimental techniques to reveal the rotational molecular constant B. Thus, it is common to indicate the rotational constants in spectroscopic energy units of cm^{-1}, denoted by $\tilde{B}$. The rotational constants for the hydroxyl anion and radical are listed in table 2.1.

2.2.2 Centrifugal distortion

The rigid rotator model assumes a fixed bond length between the atoms, but rotation introduces a force along the internuclear axis. The centripetal force stretches the bond between the atoms from the equilibrium distance r_e to r and thereby increases the moment of inertia. The system is well described by a reduced mass μ rotating about the center of mass. This leads to a modification of the energy level structure. In the model such a bond is described by a spring with a constant k. The rigidity

Table 2.1: Rotational constants in the vibrational ground state and the corresponding Electron Affinity (EA) of the hydroxyl radical and anion in cm^{-1}

	OH			OH^-	
	EA	B_0	D_0	B_0	D_0
Schulz *et al* [78]	14 741.03(17)			18.7409(45)	0.00205(45)
Rosenbaum *et al* [71]				18.73503(36)	0.0019791(56)
Smith *et al* [83]	14 741.02(3)			18.732(3)	0.00205(45)[a]
Goldfarb *et al* [30]	14 740.9824(91)			18.7354(16)	0.001982(79)
Maillard *et al* [50]		18.550401(110)	0.0019791(56)		

[a] Smith *et al* [83] used the value of D_0 measured by Schulz *et al* [78]

of a bond increases with the spring constant k. Accordingly to Hooke's law the restoring spring force F_r compensates the centripetal force F_c:

$$\begin{aligned} F_r &= F_c \\ k(r - r_e) &= \frac{\mu v^2}{r} = \mu\omega^2 r = \frac{L^2}{\mu r^3}. \end{aligned} \tag{2.35}$$

The angular velocity ω is replaced by the angular momentum $L = \omega r^2$. Thus, the change of the internuclear distance is

$$\Delta r = r - r_e = \frac{L^2}{k\mu r^3}. \tag{2.36}$$

Since the stretching is small compared to the bond length itself ($\frac{\Delta r}{r_e} << 1$), higher order terms in

$$r^3 = r_e^3 \left(1 + \frac{\Delta r}{r_e}\right)^3 = r_e^3 \left(1 + 3\frac{\Delta r}{r_e} + \mathcal{O}\left(\left(\frac{\Delta r}{r_e}\right)^2\right)\right) \tag{2.37}$$

can be neglected. The energy in the vibrating rotator is partially stored in the stretching of the linear molecule. Thus the rotational energy

$$\begin{aligned} E_{rot} &= \frac{L^2}{2\mu r^2} - \frac{1}{2}k(r - r_e)^2 \\ &\approx \frac{L^2}{2\mu r_e^2} - \frac{L^4}{2k\mu^2 r_e^6} \end{aligned} \tag{2.38}$$

is reduced by the potential energy $E_{pot} = 1/2\ k(r - r_e)^2$ of the spring elongation. The additional radially symmetric potential does not change the angular part of the wavefunctions ($\Psi = \Psi_v(r)Y_{JM}(\theta, \phi)$). Thus, equation 2.31 can still be applied and selection rules for the rigid rotator are still valid for the vibrating rotator. Replacing the angular momentum L by the quantum mechanical operator $\hat{J}$ in the rotational energy (see equation 2.38) leads to the Hamiltonian of the vibrating rotator. To calculate its eigenvalues the relation of the spherical harmonics (see equation 2.31) is applied and a rotational energy structure of

$$E_J = \frac{\hbar^2 J(J+1)}{2\mu r_e^2} - \frac{\hbar^4 J^2 (J+1)^2}{2k\mu^2 r_e^6} \tag{2.39}$$

is revealed. Introducing a second rotational constant

$$D = \frac{\hbar^4}{2k\mu^2 r_e^4} \tag{2.40}$$

compensates for the stretching effect of the molecule in the rotational energy level scheme. The centrifugal rotational constant D describes a perturbation about the equilibrium bond length r_e and is usually several orders of magnitude smaller than the rotational constant B (see table 2.1). According to equation 2.39 the energy levels are given by

$$E_J = BJ(J+1) - DJ^2(J+1)^2. \tag{2.41}$$

The centrifugal distortion constant D can be rewritten. Thereby the spring constant of the molecule is replaced by its corresponding equilibrium vibration frequency

$$\omega_e = \sqrt{\frac{k}{\mu}} \text{ (see page 167 in [33])} \tag{2.42}$$

of a spring oscillator with mass μ. Hence, the vibration frequency of the molecule can be determined by measuring the centrifugal distortion

$$D_e = \frac{4B_e^3}{\hbar^2\omega_e^2} \tag{2.43}$$

in the rotational level splitting. Here B_e and D_e denote the rotational constants B and D in equilibrium. The mean nuclear distance in a molecule increases with its vibrational excitation due to the anharmonicity in molecular potentials. But the vibration about the equilibrium distance influences the rotational constants only slightly, since the rotational oscillation is much slower than the vibrational oscillation [5]. Thus frequency averaged rotational constants are defined. The rotational constant of the rigid rotator transforms to

$$B_v = \frac{\hbar^2}{2\mu}\left\langle \frac{1}{r^2} \right\rangle_v. \tag{2.44}$$

Each vibrational state has its own set of rotational constants. Since this thesis deals with cold molecules, the rotational constants B_0 and D_0 are given for the vibrational ground state (see table 2.1).

2.3 Rotational transition intensities

The transition dipole moments are critical for modeling radiative transition rates. In section 2.3.1 the line intensities for rotational transitions in a rigid rotator are discussed. Rotational and vibrational stretching effects are neglected in the first step. In section 2.3.2 the dipole moment is averaged over its rovibrational wavefunctions in order to include such effects.

2.3.1 Line intensities in the rigid rotator

Photons couple to an atom or molecule by their electric moments. In many systems the photon-matter interaction is dominated by dipole transitions. Higher order effects are normally strongly suppressed in weak fields. Thus, photon interactions with matter are often modeled by considering only dipole interactions.

An oscillating dipole is present in rotating diatomic or linear molecule with a permanent dipole moment along the internuclear axis. In molecules with a permanent dipole moment the center of charge and the center of mass are shifted with respect to each other. The dipole moment in a rotating molecule changes its direction in the laboratory frame of reference. Thus, the photon observes an oscillating dipole moment about the center of mass of the diatomic molecule.

The strength of the photon coupling (line intensities) is closely related to the transition dipole moment

$$\begin{aligned} d_{J,M\to J',M'} &= \left|\langle J', M'|\hat{d}|J, M\rangle\right| \text{ (see page 182 in [5])} \\ &= \left|\int \Psi^*_{J',M'}\hat{d}\Psi_{J,M}dV\right| \end{aligned} \tag{2.45}$$

describing the overlap of the two rotational states $\Psi_{J,M}$ and $\Psi_{J',M'}$ under a dipole transition. Here, J and M are the rotational and magnetic quantum numbers. As stated in section 2.2.2 the angular wave functions are not affected by the additional radial potential in the vibrating rotator approximation. The selections rules

$$J = \pm 1 \quad \Delta M = 0,\ \pm 1 \tag{2.46}$$

and the J dependence of the rotational line intensities are identical for the rigid and the vibrating rotator. In his book [5] Bernath derived the transition dipole moment for diatomic and linear molecules in the rigid rotator approximation between two neighboring rotational states

$$\begin{aligned} d^2_{J\to J+1} &= \sum_M \sum_{M'} |\langle J+1, M'|\hat{d}|J, M\rangle|^2 \\ &= d_0^2(J+1) \text{ (see page 183 in [5])}. \end{aligned} \tag{2.47}$$

Here, d_0 represents the permanent dipole moment along the internuclear axis.

The dipole moment of the rigid rotator (see equation 2.45) is used to calculate the spontaneous decay of a rotational state J. Let us assume a molecular ensemble in-vacuo, where the state J is populated by N_J molecules. The number of molecules per single state (J, M) is given by $N_J/(2J+1)$ due to the degeneracy in the magnetic quantum number. In a radiation-free environment the decay rates are described by

the Einstein coefficients for spontaneous emission. Thus, each single state (J, M) decays with a rate

$$\frac{dN_{J,M}}{dt} = -\sum_{M'} A_{J,M\to J-1,M'} \frac{N_J}{2J+1}, \tag{2.48}$$

where M' can take values of $\Delta M = 0, \pm 1$ (see selection rules 2.46). Summing over all magnetic quantum numbers in state J a rotational transition rate of

$$\frac{dN_J}{dt} = -\sum_{M}\sum_{M'} A_{J,M\to J-1,M'} \frac{N_J}{2J+1} \tag{2.49}$$

is derived. Replacing the Einstein coefficient by equation 2.15 and the dipole moment d_{10} by equation 2.45 leads to the spontaneous decay rate of the rotation state J:

$$\begin{aligned}\frac{dN_J}{dt} &= -\frac{16\pi\nu^3}{3\epsilon_0 hc^3}\frac{N_J}{2J+1}\sum_{M}\sum_{M'}|\langle J, M'|\hat{d}|J-1, M\rangle|^2 \\ &= -\frac{16\pi\nu^3}{3\epsilon_0 hc^3}\frac{N_J}{2J+1} d^2_{J-1\to J} \\ &= -\frac{16\pi\nu^3}{3\epsilon_0 hc^3}\frac{d_0^2 J}{2J+1} N_J. \end{aligned} \tag{2.50}$$

Comparing the rate equation 2.50 with the definition of the Einstein coefficient 2.5 leads to a spontaneous decay rate in the rotational state J of

$$A_{J\to J-1} = \frac{16\pi\nu^3}{3\epsilon_0 hc^3}\frac{d_0^2 J}{2J+1}. \tag{2.51}$$

Thus, rotational transitions have a line intensity of $J/(2(J+1))$.

Corrections to the spontaneous decay rates due to vibrational bond stretching will be added.

2.3.2 Vibrational averaging of dipole moment functions

Molecules vibrate even in their rovibrational ground state. Thus, the bond length is changing during a vibrational oscillation. Since the dipole moment $d(r)$ of the molecule varies with the internuclear distance r, an effective dipole moment can be derived by averaging over the rovibrational probability density distribution $\Psi^2_{v,J}(r)$. This is the vibrationally averaged dipole moment.

While the line intensities in section 2.3.1 result from the angular part of the wavefunction $Y_{J,M}(\theta, \phi)$ (see page 183 in [5]), the transition dipole moment arises from averaging over the radial part of the wavefunction $\Psi_{v,J}(r)$, where v denotes the vibrational excitation. Thus, both calculations can be treated separately.

To calculate the transition dipole moment the dipole moment function $d(r)$ and the radial wavefunctions $\Psi_{v,J}(r)$ in the molecular binding potential are required. The molecular binding potential in the rotational ground state $J = 0$ is approximated by a Morse potential

$$V_{J=0}(r) = D_e(1 - e^{-\beta(r-r_e)})^2 \quad \text{(see [5] page 212)}, \tag{2.52}$$

where D_e denotes the dissociation energy. β controls the width of the potential.

$$\beta = \sqrt{\frac{\omega_e^2 \mu}{2D_e}} \tag{2.53}$$

can be written in terms of the reduced mass μ, the equilibrium frequency ω_e and the equilibrium bond length r_e. For the OH^- molecule the reduced mass μ is approximated by the masses of the oxygen $m_O = 16.0$ u [52] and the hydrogen atom $m_H = 1.01$ u [52] (see equation 2.30). The dissociation energy $D_e = 4.8$ eV, the equilibrium frequency $\omega_e = 3731$ cm^{-1} and the equilibrium binding length $r_e = 1.83\ r_b$, denoted in Bohr radii can be found in the article by Werner *et al* [90]. The resulting Morse potential for OH^- is shown in figure 2.4(a). The Morse potential has its minimum at the equilibrium distance r_e and increases strongly for lower bond distances (see figure 2.4(a)). Close to the minimum the Morse potential can be approximated by a harmonic potential, but for a high vibrational energy the Morse potential flattens to higher nuclear distances r. Thus, the energy splitting between the vibrational states reduces with the vibrational excitation.

To include rotational effects in the Morse potential $V_{J=0}(r)$ the rotational potential of a rigid rotator (see equation 2.32) is added. The binding potential is described by

$$V_J(r) = D_e(1 - e^{-\beta(r-r_e)})^2 + \frac{\hbar^2 J(J+1)}{2\mu r^2}. \tag{2.54}$$

Thus, each rotational state J has its own vibrational wavefunction.

The vibrational wavefunctions $\Psi_{v,J}(r)$ and their corresponding energy eigenvalues are calculated here using the "wavefunction" package written by Robert Johansson [44]. For the rotational ground state $J = 0$ the wavefunctions are added to their corresponding energy eigenvalues (see figure 2.4(a)).

In the next step the dipole moment function $d(r)$ has to be determined along the internuclear axis. Dipole moment calculations from first principles are quite challenging. In case of the OH^- molecule the calculations of Werner *et al* are available (see table V in [90]). But those dipole moment functions, denoted by $d_O(r)$, are based on a coordinate system with the oxygen atom O being in the origin. To

determine the transition dipole moment for rotational transitions a transformation of the dipole moment function to the center of mass S is required.

To be consistent with the publication of Ellison [25] the OH^- molecule lies along the z-axis with its center of mass in the origin. If the oxygen atom is projected on the negative part of the z-axis,

$$z_O = -\frac{m_H}{m_O + m_H} r \qquad \text{and} \qquad z_H = \frac{m_O}{m_O + m_H} r \tag{2.55}$$

reflect the positions of the oxygen O and hydrogen atom H, respectively (see equation 2.28). Here m_O and m_H are the masses of the oxygen and hydrogen atom and r denotes the bond length between them. According to the publication of Ellison [25] the dipole moment is described by

$$d_S = e\left(\sum_\alpha q_\alpha z_\alpha - \sum_i z_i\right), \tag{2.56}$$

where z_α and z_i are the positions of the nuclei and electrons projected on the internuclear axis and q_α is the number of positive charges on nucleus α. To transform the dipole moment

$$\begin{aligned} d_S(r) &= e\left(\sum_\alpha q_\alpha (z_\alpha^O + z_O) - \sum_i (z_i^O + z_O)\right) \\ &= e\left(\sum_\alpha q_\alpha z_\alpha^O + \sum_i z_i^O\right) + e z_O \left(\sum_\alpha q_\alpha - N\right) \\ &= d_O(r) - e z_O \end{aligned} \tag{2.57}$$

the positions of the charges $z_\alpha = z_\alpha^O + z_O$ and $z_i = z_i^O + z_O$ are expressed in the coordinate system of the oxygen atom. Here N denotes the number of electrons in the OH^- molecules and $e(\sum_\alpha q_\alpha - N) = -e$ is the net charge of the OH^- molecule. Replacing z_O in equation 2.57 by the expression 2.55 the dipole moment in the center of mass is revealed:

$$d_S(r) = d_O(r) + e\frac{m_H}{m_O + m_H} r. \tag{2.58}$$

Additionally the dipole moment function $d_S(r)$ is cubically interpolated to average it over the wavefunctions. The result is shown in figure 2.4(b).

Now the dipole moment function $d(r)$ has to be averaged over the probability density function $\Psi_{v,J}^2(r)$. Numerically solving the radial part of the transition dipole integral yields

$$d_{v,J} = \int \Psi_{v,J}^* d(r) \Psi_{v,J} dr. \tag{2.59}$$

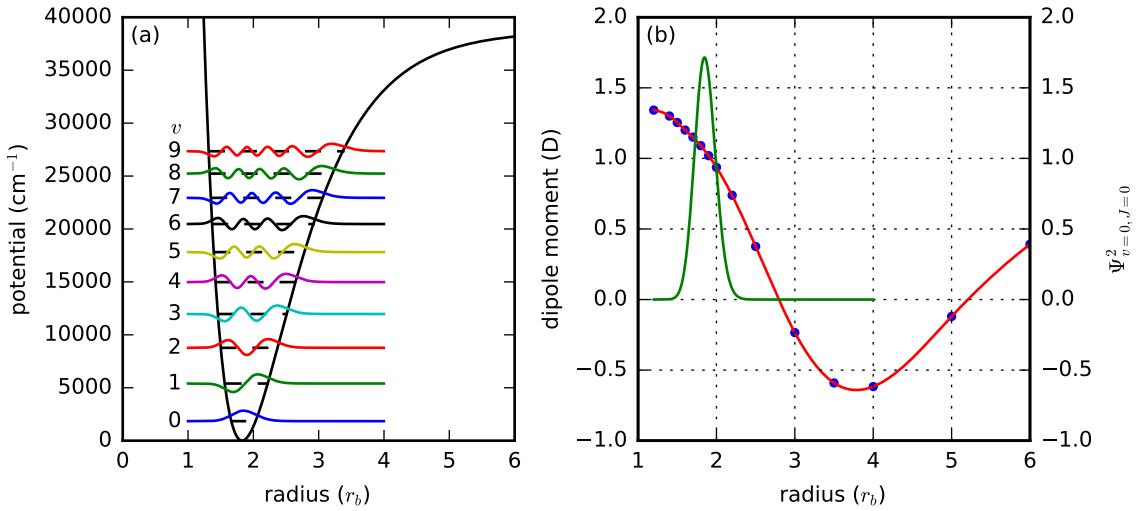

Figure 2.4: Figure (a) shows the Morse potential of the OH^- molecule and its corresponding wavefunctions $\Psi_{v,J=0}$. In figure (b) the square of the vibrational ground state $\Psi^2_{v,J}$ and the dipole moment function from Werner *et al* projected on the center of mass are plotted versus the internuclear distance. The internuclear distance in both plots is given in Bohr radii.

For the rovibrational ground state an average vibrational dipole moment of $\mu_{v=0,J=0} = 1.041$ D is derived. This value is about 0.031 D lower than the theoretical, equilibrium dipole moment value of $\mu(r_e) = 1.072$ D from Werner *et al* [90]. This small shift results from the anharmonicity of the Morse potential and from the non linearity of the dipole moment function over the width of the probability density function $\Psi^2_{v,J}$ (see figure 2.4(b)).

In the last step the modeled wavefunctions for different rotational excitations were used to determine rotational effects on the transition dipole moment. Those effects on the Einstein coefficients are described by the Herman-Wallis factor [5]

$$F(v,J) = \left(\frac{\langle \Psi_{v,J} | d(r) | \Psi_{v,J} \rangle}{\langle \Psi_{v,J=0} | d(r) | \Psi_{v,J=0} \rangle} \right)^2 \text{ (see page 267 in [5])}. \tag{2.60}$$

Since the Herman-Wallis factor decreases with increasing rotational state (see figure 2.5), it leads to a strengthening of the absorption compared to the emission in the same transition. In rotational spectroscopy the effect is seen as a weakening of the P branch (see page 276 in [5]). In this thesis the Herman-Wallis effect is neglected, because the effect for OH^- is below $<0.4\%$ in case of the lowest four states.

Including vibrational excitations in equation 2.51 leads to

$$A^{\nu}_{J \to J-1} = \frac{16\pi\nu^3}{3\epsilon_0 h c^3} \frac{d_{v,J} J}{2J+1}. \tag{2.61}$$

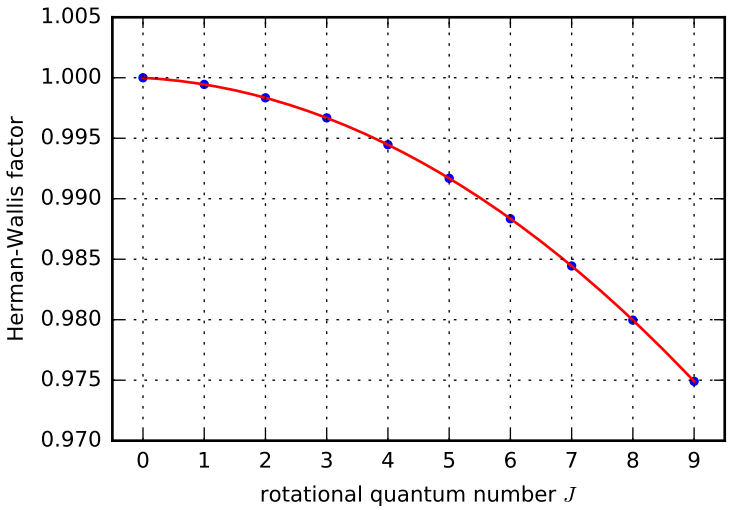

Figure 2.5: The Herman-Wallis factor (see equation 2.60) describes the rotational effect on the transition dipole moment in the Einstein coefficient. Here, the Herman-Wallis factor is modeled for the vibrational ground state $v = 0$ in OH^- by determining the wavefunction in a combined potential (see equation 2.54).The Herman-Wallis factor reduces transition rates for higher rotational excitations J.

Now the radiative rotational cooling for different radiation fields can be modeled.

2.4 Radiative cooling of rotations

In this section all radiative transition rates are combined in a broad-band radiation field yielding a linear differential equation 2.67 to model the rotational cooling dynamics (see section 2.4.1). The radiative steady state (see equation 2.71) and the radiative rotational cooling are discussed in the zero (see equation 2.73) and low temperature regime (see equation 2.74). The cooling behavior for different temperatures (see figure 2.6) and for different types of cavities (see figure 2.7 and section 2.4.2) are analyzed.

2.4.1 Rotational cooling in thermal cavities

The radiative rotational cooling of a linear molecule is modeled by describing the emission and absorption processes by the Einstein coefficient for spontaneous emission $A_{J\to J-1}$ (see equations 2.5 and 2.61) and by the photon occupation number $n_{\tilde{\nu}_{J-1\to J}}$ (see equations 2.12 and 2.13). The state of the rotational excitation J in a molecule changes to $J-1$ by photon emission and to $J+1$ by photon absorption.

Rotational states couple only to the neighboring states ($\Delta J = \pm 1$, see selection rules 2.46).

Let us assume a molecular ensemble with N_J ions in the rotational state J. Photon emission reduces the number of molecules N_J with a rate

$$\begin{aligned}\left.\frac{dN_J}{dt}\right|_{\text{emis}} &= \left.\frac{dN_J}{dt}\right|_{\text{spont}} + \left.\frac{dN_J}{dt}\right|_{\text{stim}} \\ &= -A_{J\to J-1}(1 + n_{\tilde{\nu}_{J-1\to J}})N_J \\ &= -k_{J\to J-1}N_J \text{ (see also equation 2.5, 2.4 and 2.13),}\end{aligned} \tag{2.62}$$

simultaneously increasing the number of ions N_{J-1} in the state $J-1$. Photon absorption lowers the number of molecules N_J with a rate

$$\begin{aligned}\left.\frac{dN_J}{dt}\right|_{\text{abs}} &= -\frac{g_{J+1}}{g_J}A_{J+1\to J}n_{\tilde{\nu}_{J\to J+1}}N_J \\ &= -k_{J\to J+1}N_J \text{ (see also equation 2.3 and 2.13),}\end{aligned} \tag{2.63}$$

simultaneously raising the number of molecules N_{J+1} in the state $J+1$. By combining loss and gain processes for the rotational level J the radiative rate is

$$\begin{aligned}\left.\frac{dN_J}{dt}\right|_{\text{rot}} &= \left.\frac{dN_J}{dt}\right|_{\text{abs}} + \left.\frac{dN_J}{dt}\right|_{\text{emis}} - \left.\frac{dN_{J-1}}{dt}\right|_{\text{abs}} - \left.\frac{dN_{J+1}}{dt}\right|_{\text{emis}} \\ &= -(k_{J\to J+1} + k_{J\to J-1})N_J + k_{J-1\to J}N_{J-1} + k_{J+1\to J}N_{J+1}.\end{aligned} \tag{2.64}$$

In addition to the photon-induced processes rest gas collisions reduce the total number of stored ions $N_{tot} = \sum_i N_i$. These processes are normally state-independent and linear to the number of ions leading to a mono-exponential decay

$$\left.\frac{dN_J}{dt}\right|_{\text{CSR}} = k_{\text{CSR}}N_J, \tag{2.65}$$

where k_{CSR} denotes the state-independent decay rate. Under these assumptions the cooling of the population $P_J = N_J/N_{tot}$ is independent of the storage conditions:

$$\begin{aligned}\left.\frac{dP_J}{dt}\right|_{\text{CSR}} &= \left.\frac{1}{N_{tot}}\frac{dN_J}{dt}\right|_{\text{CSR}} - \left.\frac{N_J}{N_{tot}^2}\frac{dN_{tot}}{dt}\right|_{\text{CSR}} \\ &= k_{\text{CSR}}\frac{N_J}{N_{tot}} - \frac{N_J}{N_{tot}}\sum_i k_{\text{CSR}}\frac{N_i}{N_{tot}} \\ &= (k_{\text{CSR}} - \sum_i k_{\text{CSR}}P_i)P_J \\ &= (1 - \sum_i P_i)k_{\text{CSR}}P_J = 0.\end{aligned} \tag{2.66}$$

Here the well-known relation $\sum_i P_i = 1$ is used. Thus, experimental methods allowing the calibration of the signal to the total number of ions reveal the radiative cooling rate

$$\frac{dP_J}{dt} = -(k_{J\to J+1} + k_{J\to J-1})P_J + k_{J-1\to J}P_{J-1} + k_{J+1\to J}P_{J+1}. \tag{2.67}$$

To understand the effects of the different decay rate parameters such as the Einstein coefficient for spontaneous emission and the photon occupation number, the steady state ($\frac{dP_J}{dt} \stackrel{!}{=} 0$) is analyzed. In the rotational ground state the radiative cooling rate (see equation 2.67) simplifies to

$$\frac{dP_0}{dt} = -k_{0\to 1}P_0 + k_{1\to 0}P_1. \tag{2.68}$$

Thus, the steady state in a two-state system is defined by

$$\frac{P_1}{P_0} = \frac{k_{0\to 1}}{k_{1\to 0}}. \tag{2.69}$$

If we use this expression (see equation 2.69) and the steady state condition ($\frac{dP_1}{dt} \stackrel{!}{=} 0$), a population ratio of

$$\frac{P_2}{P_1} = \frac{k_{1\to 2}}{k_{2\to 1}} \tag{2.70}$$

follows. By induction one can demonstrate that the following relation between the rotational states fullfills the steady state condition $\frac{dP_J}{dt} \stackrel{!}{=} 0$:

$$\begin{aligned}\frac{P_{J+1}}{P_J} &= \frac{k_{J\to J+1}}{k_{J+1\to J}} \\ &= \frac{g_{J+1}}{g_J}\frac{n_{\tilde{\nu}_{J\to J+1}}}{(1+n_{\tilde{\nu}_{J\to J+1}})}.\end{aligned} \tag{2.71}$$

Thus, the steady state population depends only on the radiative field and the degeneracy of states $g_J = 2J + 1$. In a thermal cavity the relation (see equation 2.71) follows the Boltzmann distribution (see equation 2.8).

To gain deeper insight into the cooling rates of the molecule a zero field ($n_{\tilde{\nu}} = 0$) approximation is analyzed. Under this assumption the radiative cooling rate simplifies to

$$\begin{aligned}\left.\frac{dP_J}{dt}\right|_{T=0} &= -k_{J\to J-1}P_J + k_{J+1\to J}P_{J+1} \\ &= -A_{J\to J-1}P_J + A_{J+1\to J}P_{J+1}.\end{aligned} \tag{2.72}$$

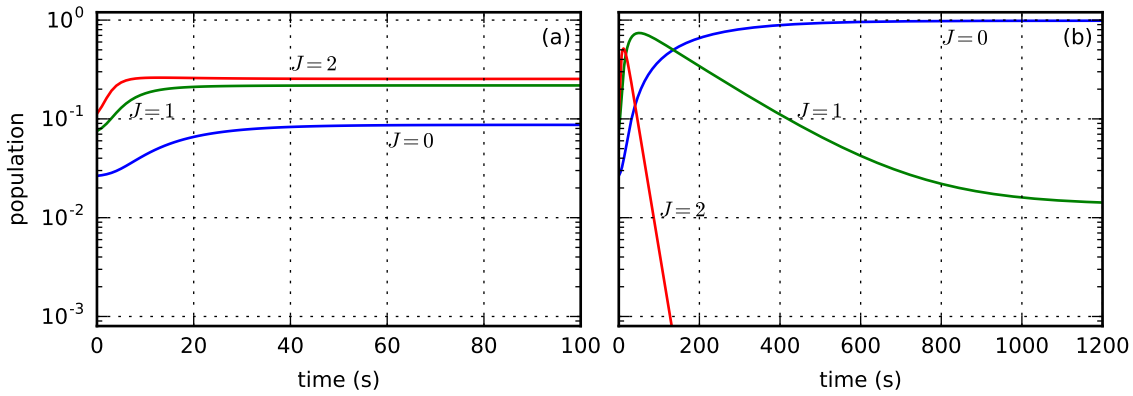

Figure 2.6: The radiative cooling of populations for the three lowest rotational states is presented. Here a 1000 K rotationally hot OH^- distribution is cooling in a thermal cavity at 300 K (a) and 10 K (b). The corresponding Einstein coefficients for spontaneous emission are modeled with a dipole moment of $\mu_{v=0,J=0} = 1.041$ D.

Taking into account that the lowest rotational state $J = 0$ can not cool further, the eigenvalues of such a system are

$$\lambda_J = \begin{cases} -A_{J\to J-1} & \text{for } J \geq 0 \\ 0 & \text{for } J = 0 \end{cases} . \tag{2.73}$$

Hence, the observed decay rates (see equation 2.73) under the zero field assumption directly reveal the radiative lifetime and accordingly the Einstein coefficient of spontaneous emission which describes the photon coupling in a broad-band photon field. Including the photon field and therefore the photon occupation numbers at the resonance frequencies in the calculation, the observed decay rates incorporate effects of stimulated emission and absorption. In the low temperature regime only the lowest transition frequencies are relevant, since the photon field contributes only to the long wavelength spectrum (see fig. 2.2). Thus only the photon occupation number at the smallest transition wavenumber $\tilde{\nu}_{0\to1}$ is considered. In this approximation the eigenvalues of our system change to

$$\lambda_J = \begin{cases} -A_{J\to J-1} & \text{for } J \geq 1 \\ -A_{J\to J-1}(1 + n_{\nu_{J-1\to J}}) & \text{for } J = 1 \\ 0 & \text{for } J = 0 \end{cases} . \tag{2.74}$$

Hence, a small acceleration of the cooling rate in the $J = 1$ state is observed. However, the cooling rate λ_1 can directly serve as an upper limit for the Einstein coefficient for spontaneous emission.

In order to include photon occupation numbers for higher rotational transitions fully numerical simulations of the linear differential equation 2.67 by using the exponential matrix solver implemented in the SciPy package in Python are performed. The rotational cooling of a 1000 K rotationally hot OH^- ensemble in a 300 K (see figure 2.6(a)) or 10 K (see figure 2.6(b)) radiation field are modeled up to 1200 s. Here, the calculated dipole moment for OH^- of $\mu_{v=0,J=0} = 1.041$ D in the rovibrational ground state is used for all rotational states (see section 2.3.2). As shown in figure 2.6 the OH^- molecule cools down to the temperature of the radiative cavity in less than 40 s in the 300 K environment (see figure 2.6(a)), but needs about 1000 s to reach the steady state at 10 K (see figure 2.6(b)). In the 300 K cavity the lowest rotational states seem to cool at a similar rate, but in a 10 K environment the rotational state $J = 2$ decays much faster than the state $J = 1$. Thus the difference between the rates predicted by the Einstein coefficients for spontaneous emission is compensated in the 300 K cavity by the stimulated emission and absorption effects controlled by the radiative field. Thus, only in the low temperature regime a stepwise cooling of the rotational states is observed. The following two effects are relevant for such a stepwise time structure:

- The Population in rotational state J can cool only to $J - 1$.
- Higher rotational states cool faster than the lower ones.

These two statements are generally valid for radiative rotational transitions in cold environments. The first effect is directly fulfilled by considering selection rules of dipole transitions. The second effect arises due to the rotational energy structure. Since the Einstein coefficient for spontaneous emission scales with the third power of the transition energy and the rotational energy splitting of the states increases approximately linear with the rotational quantum number, the higher rotational states cool faster. In total this leads to a stepwise cooling behavior which has also been observed for molecules like CH^+ [62].

In a nutshell natural lifetimes of the lowest rotational states and photon occupation numbers are revealed by observing the time-dependence of the populations. Thus, the rotational cooling of molecules like OH^- is a perfect tool to demonstrate the power of long storage times and to measure the temperature in radiative fields in cryogenic storage rings.

2.4.2 Rotational cooling in non-thermal cavities

As seen in section 2.1.1 small leaks of warm radiation can change the photon field completely. In this section the effects of non-thermal cavities on the rotational cooling are discussed. First simulations of the rotational cooling in a thermal 10 K environment (see figure 2.7(a)) are presented. In a second step the radiation field

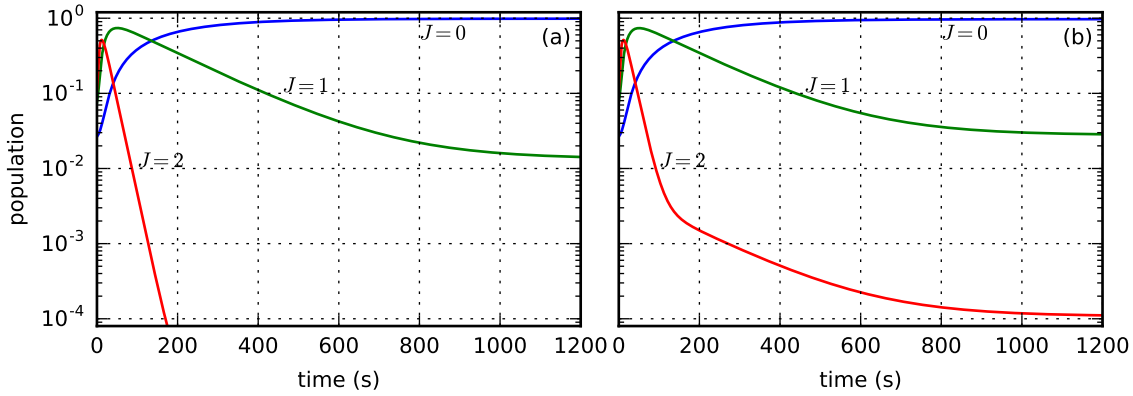

Figure 2.7: The radiative cooling of populations for the three lowest rotational states is presented. Here a 1000 K rotationally hot OH^- distribution is cooling in a thermal cavity (10 K) and non-thermal cavity (99.9% 10 K, 0.1% 300 K) (b). The corresponding Einstein coefficients for spontaneous emission are modeled with dipole moment of $\mu_{v=0,J=0} = 1.041$ D.

is altered by allowing a small amount of 0.1% of 300 K radiation to enter the 10 K cavity (see figure 2.7(b)).

Although the combined radiation field differs vastly from a thermal one (see figure 2.2), the rotational cooling shown in figure 2.7 varies only slightly for short storage times $t < 150$ s. But for long storage times $t > 150$ s changes in the rotational cooling behavior can be observed. As shown in figure 2.7 the resulting steady state for $J = 1$ and $J = 2$ is strongly shifted in the mixed radiation field. Thus, mixed radiation fields will lead to different measured effective rotational temperatures. Furthermore the decay of $J = 2$ shows an interesting behavior (see figure 2.7(b)). It bends at about ~ 150 s to the decay rate of the state $J = 1$. Since the population P_2 and P_1 of $J = 2$ and $J = 1$ are partially in a steady state, both populations decay at the same rate. Those effects can also be seen in thermal radiation fields, but are not obvious, since in a non-thermal radiation field the higher rotational states are much more strongly coupled.

To summarize, the rotational cooling of linear molecules have been modeled in a broad-band radiation field in-vacuo with only four parameters: the rotational constants B_0 and D_0, the photon occupation number and the transition dipole moment for rotational transitions. While the rotational constants and accordingly the rotational energy structure of many diatomic and linear molecules have been measured, the photon occupation number and the transition dipole moment are not assumed in this work to be known a-priori. Thus, the transition dipole moment of the studied molecule and the photon occupation number in the experimental setup can be revealed by monitoring the radiative cooling of the rotational population $P_J(t)$ over

time.

3 Photodetachment of closed shell anions

Otto *et al* [65] have shown that the rotational population in OH^- can be determined by photodetachment. If the dynamics of population ratios are observed independent of the storage time, photon occupation numbers and dipole moments for rotational transitions can be derived (see section 2). Thus, this chapter deals with the electronic state structure (see section 3.1) and its impact on the rotational energy levels to model the photodetachment spectrum of closed shell anions (see section 3.2).

3.1 Electronic state structure

Additional to the nuclear rotation modeled by the rigid rotator (see section 2.2.1) molecules can have a non-vanishing electronic angular momentum and spin. These angular momenta can couple to the nuclear rotation and change the rotational energy structure in the molecule. Thus, it is essential to know the electronic state (see section 3.1.1) and its coupling (see section 3.1.2) to the nuclear rotation. Furthermore electronic angular momenta can lead to a splitting of states depending on their wavefunction symmetry (parity). Since dipole transitions are only allowed for states with opposite parity, the Λ doubling is discussed in a separate section 3.1.3.

3.1.1 Classification of electronic states

Electronic states of molecules are classified in a similar way as in atoms, but taking the additional symmetry (internuclear axis) into account. Hence, the degeneracy of the angular momentum which precesses around the internuclear axis is lifted. Thus, the main symbol $\Lambda = |M_L| = \{0,\ 1,\ \cdots\}$ of the classification gives in Greek uppercase letters $\{\Sigma,\ \Pi,\ \Delta,\ \Phi,\ \cdots\}$ the absolute value of the electronic angular orbital momentum around the internuclear axis. If $\Lambda \neq 0$, the electronic angular orbital momentum couples with the spin $\Sigma = \{-S,\ S-1, \cdots,\ S\}$, which also precesses around the internuclear axis, to the total electronic angular momentum $\Omega = |\Lambda + \Sigma|$. This results in $(2\Sigma + 1)$ splittings of the electronic state. Thus, the electronic state classification in a molecule is given by [37]

$$^{2\Sigma+1}\Lambda_{\Omega}. \tag{3.1}$$

For molecules such as OH^- and SH^- the electronic ground state is characterized by a $^1\Sigma$ state, because all orbitals are completely filled up (closed shell) leading to zero spin $\Sigma = 0$ and zero angular momentum $\Lambda = 0$. Since the spin does not couple to the angular momentum, if $\Lambda = 0$, the total electronic angular momentum Ω is not defined and thus not given. If one electron in such a system is detached for example by photodetachment, an unpaired electron is produced, which results in a spin of $\Sigma = 1/2$ and an electronic angular orbital momentum $\Lambda = 0, 1$ in the molecule. If the produced neutral has an electronic angular momentum of $\Lambda = 1$, both momenta couple either to $\Omega = 1/2$ or $\Omega = 3/2$. Thus, the electronic ground state of the OH and SH molecule is a doublet ($2\Sigma + 1 = 2$) with the electronic configuration $^2\Pi$.

Additional to the quantum numbers the molecular electronic states are classified by their parity symmetry, since the dipole operator allows only transitions between symmetric (+) and antisymmetric (−) states

$$(+ \longleftrightarrow -, + \nrightarrow +, - \nrightarrow -). \tag{3.2}$$

Thus, the symmetry of the electronic states determines the dipole allowed transitions. For Σ states the ground state can either be symmetric or antisymmetric. Thus, the OH^- electronic ground state is denoted as $^1\Sigma^+$ (symmetric). Π states intrinsically have both symmetries.

3.1.2 Hund's coupling cases for the anion and radical

Molecules intrinsically have three different types of angular momentum: electron spin Σ, electronic orbital momentum Λ and the angular momentum of nuclear rotation N. These couple to a total angular momentum vector $\vec{J}$. In the case of OH^- and SH^- ($^1\Sigma^+$ state) the electron spin and electronic orbital momentum is zero. Hence, the total angular momentum is identical to the angular momentum of nuclear rotation and the molecule can be treated as a rigid rotator. But ground states of the corresponding neutrals OH and SH have all three different kinds of momenta. Hund was the first to describe the coupling order of those three angular momenta for different cases. This section 3.1.2 is based on the concise summary of Herzberg [37] and concentrates on the first two of Hund's cases. These two cases are important to understand the rotational structure and later on the theoretical description of the photodetachment of closed shell molecules into $^2\Pi$ states.

Hund's case (a): In this case the spin Σ strongly couples to the angular momentum Λ along the nuclear axis and only weakly to the nuclear rotation. The spin coupling to the internuclear axis leads to a multiplet splitting of $2\Sigma + 1$ of the electronic ground state and is often called LS coupling in analogy to atomic physics. The resulting electronic angular momentum Ω along the nuclear axis weakly couples to the nuclear rotation N. For this reason the precession axis of a molecule in

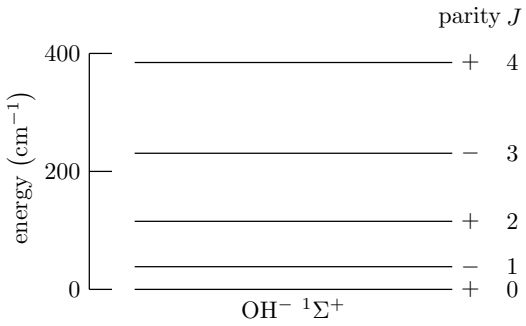

Figure 3.1: The schematic structure of the energy levels in OH^- indicating their parity ($\pm$) for the lowest rotational states in the vibrational ground state is presented.

Hund's case (a) is tilted to the one of the rigid rotator. Hence, the projection on the internuclear axis is subtracted from the rotational energy. If molecular stretching is neglected, the rotational energy in Hund's case (a) is given by [37]

$$E^a_{rot} = B_\nu(J(J+1) - \Omega). \tag{3.3}$$

Here the rotational constant B_ν does not significantly differ between the multiplet states if the splitting is small (see page 220 in [37]).

Hund's case (b): Molecules with a zero electronic angular orbital momentum do not have an intrinsic magnetic field along the internuclear axis. Hence, the spin is not coupled to the symmetry axis of the molecule. This might be even the case for $\Lambda \neq 0$ if the spin is weakly coupled to the internuclear axis. Thus, Hund's case (a) can not apply here. As a result the angular momentum of the nuclear rotation N is coupled with the electronic momentum Λ to the total angular momentum apart from spin

$$K = \Lambda + N = \{\Lambda,\ \Lambda + 1,\ \cdots\}\,. \tag{3.4}$$

Then the momentum K is combined with the spin to the total angular momentum

$$J = \{|K - S|\,,\ |K - S| + 1,\ \cdots\,,\ K + S\}\,, \tag{3.5}$$

leading as in Hund's case (a) to $(2S + 1)$ multiplet states. Since the closed shell anions have neither an angular orbital momentum ($\Lambda = 0$) nor a spin ($S = 0$), the nuclear rotation is identical to the total angular momentum. Hence, closed shell molecules are singlets in Hund's case (b) with no momentum along the internuclear axis and no Λ doubling (see section 3.1.3 and figure 3.1).

As a result the momentum coupling scheme has often to be switched during the photodetachment transition like between the electronic ground states of OH^- and OH. Hence, Hund's cases are important to understand the rotational intensities in photodetachment transitions (see section 3.2.2).

Uncoupling phenomena: Many molecules such as OH can not be strictly assigned to the case (a), since the coupling between the orbital angular momenta is weakened with higher rotational excitation (uncoupling phenomena). With increasing coupling strength A_ν of the electronic orbital angular momentum to the spin the uncoupling phenomenon is shifted to higher rotational energies. Thus, the strength of the uncoupling in the molecules depends also on the ratio

$$Y = \frac{A_v}{B_v} \tag{3.6}$$

between the rotational constant B_ν and the spin-orbit coupling energy A_ν. Hill and Van Vleck [38] calculated for doublet states such as in OH the rotational energy including a non-infinite spin-orbit coupling neglecting the coupling between the spin S and the angular momentum K (see equation 3.4), which is the combined momentum of the electronic state Λ and of the nuclear rotation N. Thus, the rotational energy can be expressed in the state $^2\Pi_{3/2}$ ($J = K + 1/2$) by

$$F_1(J) = B_v \left[\left(J + \frac{1}{2} \right)^2 - \Lambda^2 - \frac{X}{2} \right] - D_v J^4, \tag{3.7}$$

and in the state $^2\Pi_{1/2}$ ($J = K - 1/2$) by

$$F_2(J) = B_v \left[\left(J + \frac{1}{2} \right)^2 - \Lambda^2 + \frac{X}{2} \right] - D_v \left(J + 1 \right)^4. \tag{3.8}$$

Here we use the correction factor

$$X^2 = Y \left(Y - 4 \right) \Lambda^2 + 4 \left(J + \frac{1}{2} \right)^2. \tag{3.9}$$

The centrifugal distortion correction in equation 3.7 and 3.8 does not include any rotational coupling effects. Considering the strengths of the rotational constants B_v and D_v such an approximation is especially sufficient for the lowest rotational states (see table 2.1). The resulting rotational energy structure in the vibrational ground state for OH is shown in figure 3.2.

The last effect on the rotational energy structure which is considered in this thesis is the Λ doubling (see section 3.1.3). The states split up in energy according to their wavefunction symmetry, which is an important criterion of the selection rules for photodetachment transitions.

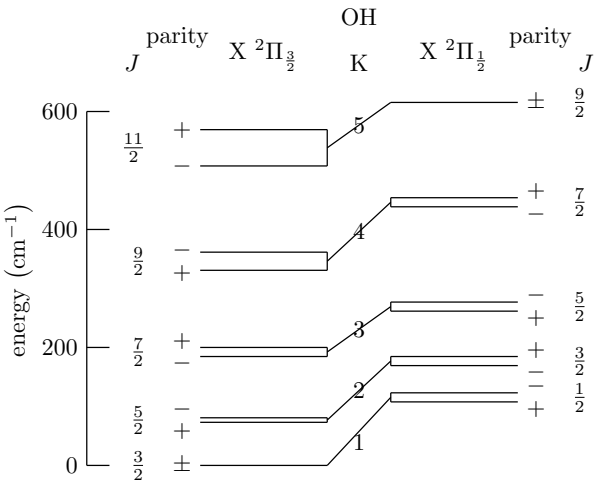

Figure 3.2: Schematic structure of the energy levels in OH indicating their parity ($\pm$) for the lowest rotational states in the vibrational ground state is shown. The Λ doubling effect (see section 3.1.3) between the different parity states is stretched to visualize the splitting.

3.1.3 Λ Doubling

The electronic angular momentum Λ has two possible orientations along the internuclear axis ($\pm\Lambda$). Since the two orientations are not eigenstates of the molecule, we have to describe the wavefunctions Ψ^+ and Ψ^- by a linear combination

$$\Psi^{\pm} = \psi(+\Lambda) \pm \psi(-\Lambda) \tag{3.10}$$

of both orientations. Under reflection which is a parity symmetry operation ($+\Lambda \rightarrow -\Lambda,\ -\Lambda \rightarrow +\Lambda$) the wavefunction Ψ^+ is symmetric ($+$) while Ψ^- is antisymmetric ($-$). Thus, every molecule with a non-zero electronic momentum has both symmetries for every combination of molecular quantum numbers. Hence, dipole transitions to such states are never dipole forbidden by symmetry. The uncoupling of the electronic momentum from the nuclear axis induces a splitting in the degeneracy of the Ψ^+ and Ψ^- states, since the two states observe a different Coriolis interaction. This splitting is called "Λ type doubling". The perturbation effect was first solved for Σ states by Van Vleck [85]. Referring to the isoelectronic HF^+ molecule [29] the parity splitting by Λ doubling in $^2\Pi$ states is given in the *e*-*f* notation [15] by

$$\begin{aligned}\Delta\nu_{ef} &= F_e - F_f \\ &= \pm\left(J+\frac{1}{2}\right)\left[\left(\pm 1 + \frac{2-Y}{X}\right)\left(\frac{1}{2}p+q\right) + 2\frac{\left(J+\frac{3}{2}\right)\left(J-\frac{1}{2}\right)}{X}q\right].\end{aligned} \tag{3.11}$$

Here states with parity $(-1)^{J-1/2}$ are denoted as e and those with $-(-1)^{J-1/2}$ are designated as f (see figure 3.2). Thus, the + part of equation refers to the Λ doubling in F_2 (see equation 3.7) and − to the one in F_1 (see equation 3.8). The Λ doubling coefficients p and q have been first calculated by Mulliken and Christy for a variety of molecules including OH [59]. For this thesis we rely on the experimental parameters from Maillard *et al* [50] to be consistent with the paper [54]. Especially for OH there is rather a large number of papers on calculated and measured p and q coefficients for different states [35, 39, 58].

3.2 Relative photodetachment cross sections

Photodetachment is a versatile tool to reveal properties of anions and their corresponding neutrals. For example fine-structure in photodetachment spectra are used to determine rotational constants of anionic molecules [78]. In order to reveal rotational constants and populations we have to understand the rotational structure, line intensities and photon energy dependence of photodetachment transitions (see section 3.2.1, 3.2.2 and 3.2.3). In the last part all concepts are combined to model the cross section ratios (see section 3.2.4).

3.2.1 Rotational structure of photodetachment thresholds

The rotational structure in photodetachment spectra is closely related to the rotational structure of the anion and its corresponding neutral. For the OH^- molecule the rotational levels can be described by the vibrating rotator (see figure 3.1 and equation 2.41). Due to its electronic angular momentum Λ and spin the OH radical has a more complex structure (see figure 3.2 and equation 3.7, 3.8 and 3.11). Those structures are energetically connected via the Electron Affinity (EA) which is the released energy, if an electron is attached to the neutral. For the OH molecule the EA ($\tilde{\nu}_{EA}$ = 14741.0 cm^{-1} [30, 78]) is equivalent to the minimum photon energy needed to photodetach the OH^- in its rovibrational ground state. As we see in figure 3.3 this transition is marked by the blue arrow with the label $R3$. But not all photodetachment transitions are allowed.

In this section the processes are described for the OH^- molecule, but they are transferable to other anions such as OD^-, SH^- and SD^-. In order to derive the conditions the photodetachment is split into two sub-processes. In the first subprocess

$$OH^-(^1\Sigma^+, J'') + h\nu \rightarrow (OH + e^-)(^1\Pi, J_c) \tag{3.12}$$

the OH^- molecule in the $^1\Sigma$ state is excited to a virtual complex $^1\Pi$ state with opposite parity [41, 70, 79]. Here J'' and J_c are the total angular momenta in the

molecular states. The transition 3.12 is a simple electronic dipole transition. Hence, the total angular momentum can only be changed by $J_c - J^{''} = 0, \pm 1$ (see page 169 [37]).

In a second process

$$(\mathrm{OH} + e^-)(^1\Pi, J_c) \rightarrow \mathrm{OH}(^2\Pi, J^{'} = J_c \pm \frac{1}{2}) + e^- \tag{3.13}$$

the electron leaves the virtual complex state in an s-wave. Thus, the parity is conserved. The electron hole in the shell results in a spin of $1/2$ of the OH molecule. This spin couples to the internuclear axis of the molecule and leads to a $^2\Pi$ doublet state. The spin can either be aligned along ($J^{'} = J_c + 1/2$) or against ($J^{'} = J_c - 1/2$) the direction of the electronic angular momentum Λ. During the spin coupling to the internuclear axis the Hund's case is switched from (b) to (a), which has to be considered for calculations of line intensities (see section 3.2.2).

The photodetachment transitions are labeled by the total angular momentum $K = N + \Lambda$ apart from spin. Similar to electronic transitions photodetachment transitions are denoted by O, P, Q, R and S for a change in K by -2, -1, 0, 1 and 2 (see figure 3.3). O photodetachment transitions are only possible to the $^2\Pi_{3/2}$ state and S transitions to the $^2\Pi_{1/2}$ [78]. To distinguish between the electronic OH states the branch symbol $\{O,\ P,\ Q,\ R,\ S\}$ is followed by 1 or 3 for the states $^2\Pi_{1/2}$ or $^2\Pi_{3/2}$ respectively. To know the addressed state the transition label includes the anionic rotational excitation $J^{''}$ in brackets. Thus, the transition is denoted by

$$T(J^{''}) = \{O,\ P,\ Q,\ R,\ S\}\,\{1,\ 3\}\,(J^{''}). \tag{3.14}$$

For example the transition $R3(0)$ connects the rovibrational ground states of OH^- and OH (see figure 3.3). The rovibrational ground state of OH^- has only three possible transitions, while all states with $J^{''} \geq 3$ can be photodetached into 8 different levels (see figure 3.3).

In OH the spin uncouples from the electronic angular momentum for high angular momentum $J^{'}$ and Hund's case (a) switches to Hund's case (b). In this case the total angular momentum can either be changed by 0 or ± 1. Hence, the O and S branches exist only for photodetachment transitions to low rotational states. Thus, the maximum number of transitions per rotational state is reduced to 6 for highly excited rotational states. In other words, photodetachment branches O and S are only visible in an LS coupled system [30].

Furthermore the rotational states in OH^- have a defined parity. As a result only transitions to states with an opposite parity are allowed. Due to the Λ doubling the rotational states in the $^2\Pi$ states split up according to the symmetry of the wavefunction. Thus, the transitions $S1(0)$ and $P1(3)$ do not address the same state (see figure 3.3).

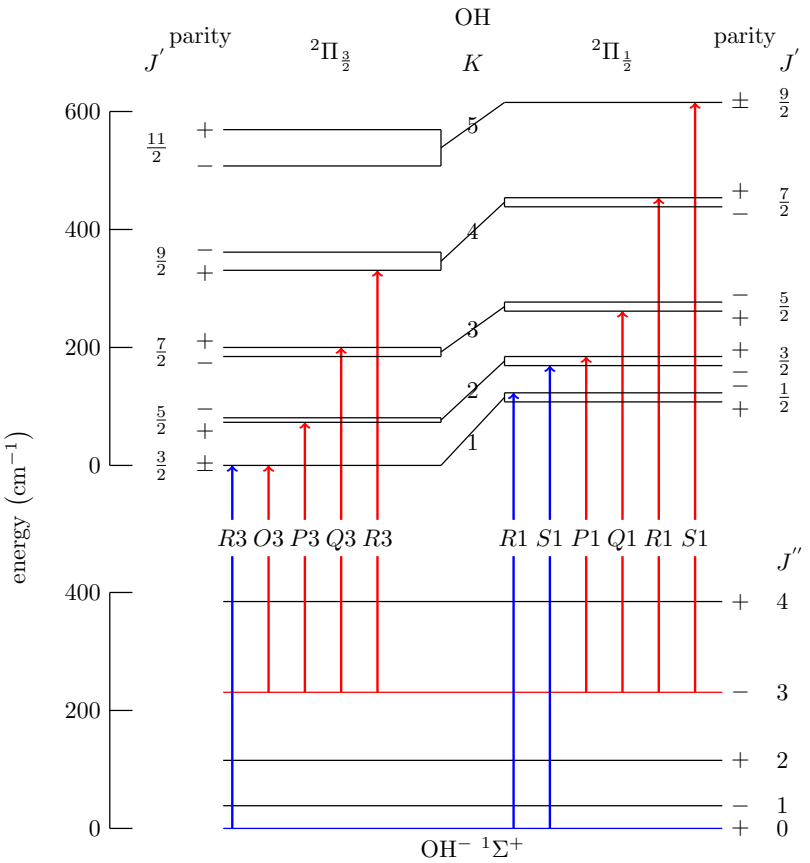

Figure 3.3: The schematic structure of photodetachment transitions from the rotational state $J = 0$ (blue) and $J = 3$ (red) in OH^- to OH in their vibrational ground states is presented. The transitions are denoted by 3.14.

3.2.2 Rotational intensities of fine-structure thresholds

Schulz *et al* [78] observed in the photodetachment spectrum of OH^- different thresholds addressing the same rotational state. The different intensities arise from the rotational structure of the anion and the neutral molecule. In this section the relative intensities are modeled for the $^1\Sigma$ to $^2\Pi$ photodetachment transition according to Schulz *et al* [79]. These intensities are essential to determine the rotational-state-dependent and population-independent relative cross sections.

In the first process the anion is excited by a dipole transition to a complex $^1\Pi$ state (see process 3.12). In bracket description the photon absorption is expressed by the electronic transition matrix element

$$\left\langle {}^1\Pi,\ J_c \middle| \hat{\mu} \middle| {}^1\Sigma,\ J'' \right\rangle, \tag{3.15}$$

which is propotional to the square root of the Hönl-London factor (see page 208 in [37])

$$S_{J''} = \frac{1}{4}\begin{cases} J'' - 1 & P \text{ branch} \\ 2J'' + 1 & Q \text{ branch} \\ J'' + 2 & R \text{ branch} \end{cases}. \tag{3.16}$$

Similar to section 3.2.1 the change of the rotational excitation by -1, 0 and 1 is denoted by the branches P, Q and R (see equation 3.14). The rotational excitation can also alter the vibrational wavefunctions (see section 2.3.2) and change the transition dipole moment 3.15. Considering the small variation in the Herman-Wallis factor (see figure 2.5 and equation 2.60) for the lowest rotational states, the variation on the wavefunction overlap with the rotational excitation is negligibly small.

In the second process the "free" electron is decoupled from the complex state $^1\Pi$. The electron is assumed to leave the complex state in an s-wave, such that the angular momentum is changed by the electron spin $\pm 1/2$. As a result, the total angular momentum Ω of the molecule can either take values of 1/2 or 3/2. The emitted electron does not alter the parity of the molecular state, since s-wave functions have a positive symmetry. Due to the magnetic field along the internuclear axis the spin of the molecule is coupled to the electronic angular momentum Λ. Hence, we change the coupling scheme from Hund's case (b) to Hund's case (a). This process is identical to the momentum reprojection from the ls to the jj coupled state in atomic physics. For the overlap between the complex states $^2\Pi_\Omega$ and $^1\Pi$

$$\left\langle {}^2\Pi_\Omega,\ J' \middle|^1\Pi,\ J_c \right\rangle. \tag{3.17}$$

(see process 3.13) Walker *et al* derived the coupling coefficient [87]

$$\left\langle {}^2\Pi_\Omega,\ J' \middle|^1\Pi,\ J_c \right\rangle = \sqrt{\frac{1}{2(2J_c+1)}}\begin{cases} \sqrt{J_c} & J' = J_c + \frac{1}{2},\ \Omega = \frac{1}{2} \\ -\sqrt{J_c+2} & J' = J_c + \frac{1}{2},\ \Omega = \frac{3}{2} \\ \sqrt{J_c+1} & J' = J_c - \frac{1}{2},\ \Omega = \frac{1}{2} \\ \sqrt{J_c-1} & J' = J_c - \frac{1}{2},\ \Omega = \frac{3}{2} \end{cases}. \tag{3.18}$$

According to Goldfarb *et al* [30] the signs in equation 3.18 are switched for the cases $J' = J_c + \frac{1}{2},\ \Omega = \frac{1}{2}$ and $J' = J_c + \frac{3}{2},\ \Omega = \frac{1}{2}$. The coefficients in equation 3.18 include already the Clebsch-Gordan coefficients. The eigenstates of the jj coupled system are not necessarily energy eigenstates of the real neutral molecule, defined in the section 3.1.2 by $F1$ and $F2$. The real eigenstates of the OH molecule are a linear combination of the jj coupling eigenfunctions. The $F1$ state is mainly affected by the $^2\Pi_{3/2}$ state, while the $F2$ state follows mainly the $^2\Pi_{1/2}$ for a low rotational excitation. Thus, in the last step the Hund's case (a) eigenfunctions are projected

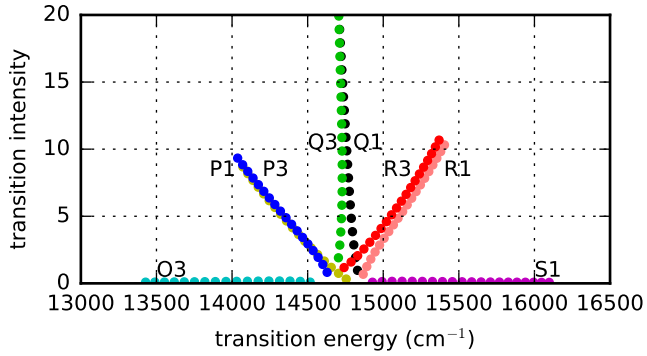

Figure 3.4: Transition intensities for the lowest 20 rotational states are plotted against their corresponding transition energies.

on the true wavefunctions Ψ_α of the energy eigenstates F_1 ($\alpha = 1$) or F_2 ($\alpha = 2$)

$$\langle \Psi_\alpha,\ J' \big|^2\Pi_\Omega,\ J' \rangle. \tag{3.19}$$

To calculate the mixing coefficients c_1 and c_2 for the real eigenfunctions

$$\big|\Psi_\alpha,\ J'\big\rangle = c_1^\alpha\ \big|^2\Pi_{1/2},\ J'\big\rangle + c_2^\alpha\ \big|^2\Pi_{3/2},\ J'\big\rangle, \tag{3.20}$$

we use the solution of the Hamiltonian [87]

$$\hat{H} = B(\vec{J}' - \vec{L}' - \vec{S}')^2 + A\vec{L}'\vec{S}' \tag{3.21}$$

for spin-orbit coupling. Here B is the rotational constant and A describes the coupling strength between the spin $\vec{S}'$ and the angular momentum $\vec{L}'$ of the molecule. For such a system Schulz *et al* [79] have derived the coefficients c_1^α and c_2^α for the OH eigenfunctions, but with a wrong phase factor. If the coefficients of Schulz *et al* [79] are applied the transition intensity in the figure 3.4 of the S1 branch increases and P1 and R3 contributions become negligible [30]. With the correct phase factors the coefficients for the OH eigenfunctions are given by

$$c_1^{F_1} = \kappa = c_2^{F_2} \qquad \text{and} \qquad c_2^{F_1} = -\sqrt{1-\kappa^2} = -c_1^{F_2} \tag{3.22}$$

$$\text{with } \kappa = \sqrt{\frac{X-2+Y}{2X}}. \tag{3.23}$$

It is not surprising that the mixing between the states depends on the spin decoupling factor X (see equation 3.9) introduced for the energy eigenstates of OH. To get the total intensity for the rotational transitions one sums over all intermediate

states and takes the square of the transition integral. Hence, one obtains for the rotational intensities the expression

$$I(J^{'}, J^{''}, \alpha) \propto \Bigg| \sum_{J_c = J' \pm 1/2} \sum_{\Omega = 1/2,\ 3/2} \left\langle \Psi_{\alpha}^{\mathrm{OH}},\ J' \right|^2 \Pi_{\Omega},\ J' \Big\rangle \cdot \left\langle {}^2\Pi_{\Omega},\ J' \right|^1 \Pi,\ J_c \Big\rangle \cdot \left\langle {}^1\Pi,\ J_c \right| \hat{\mu} \Big|^1 \Sigma,\ J^{''} \Big\rangle \Bigg|^2 . \tag{3.24}$$

Including all sub-processes the transition intensity for the OH^- photodetachment according to Goldfarb *et al* [30] is given for $O3$ and $P1$ ($J^{'} = J^{''} - 3/2$) by

$$I_{J'=J''-3/2} \propto \frac{J^{''} - 1}{2(2J^{''} - 1)} \left(c_1^{\alpha} \sqrt{J^{''}} + c_2^{\alpha} \sqrt{J^{''} - 2} \right)^2 , \tag{3.25}$$

for $P3$ and $Q1$ ($J^{'} = J^{''} - 1/2$) by

$$I_{J'=J''-1/2} \propto \frac{J^{''} - 1}{2(2J^{''} - 1)} \left(c_1^{\alpha} \sqrt{J^{''} - 1} - c_2^{\alpha} \sqrt{J^{''} + 1} \right)^2 + \frac{1}{2} \left(c_1^{\alpha} \sqrt{J^{''} + 1} + c_2^{\alpha} \sqrt{J^{''} - 1} \right)^2 , \tag{3.26}$$

for $Q3$ and $R1$ ($J^{'} = J^{''} + 1/2$) by

$$I_{J'=J''+1/2} \propto \frac{1}{2} \left(c_1^{\alpha} \sqrt{J^{''}} - c_2^{\alpha} \sqrt{J^{''} + 2} \right)^2 + \frac{J^{''} + 2}{2(2J^{''} + 3)} \left(c_1^{\alpha} \sqrt{J^{''} + 2} + c_2^{\alpha} \sqrt{J^{''}} \right)^2 , \tag{3.27}$$

and for $R3$ and $S1$ ($J^{'} = J^{''} + 3/2$) by

$$I_{J'=J''+3/2} \propto \frac{J^{''} + 2}{2(2J^{''} + 3)} \left(c_1^{\alpha} \sqrt{J^{''} + 1} - c_2^{\alpha} \sqrt{J^{''} + 3} \right)^2 . \tag{3.28}$$

To verify the obtained theoretical calculation the rotational intensities are plotted versus the transition energy (see figure 3.4). The intensity roughly increases linearly with the rotational quantum number due to the higher degeneracy. The splitting between rotational states also increases with the rotational excitation. Hence, the photon energy needed for inducing a transition decreases for P transitions and increases for R transitions with higher rotational excitation (see figure 3.4).

As stated before the rotation about the center of mass induces a decoupling of the spin from the internuclear axis. Thus, the energy splitting of doublet states reduces with increasing rotation. Hence, the difference between the $P1/Q1/R1$ and the $P3/Q3/R3$ transition intensities decreases with higher rotational quantum

number (see figure 3.4). Furthermore the transitions $S1$ and $O3$ are only visible, if the coupling scheme is switched during the photodetachment (see section 3.2.1). For higher rotational excitation of OH the spin coupling to the electronic angular momentum is weakened. Thus the rotational intensities for $S1$ and $O3$ for high rotational excitation are reduced.

3.2.3 Spectral dependence of fine-structure thresholds

The spectral dependence of photodetachment cross sections has been studied theoretically [26, 79] and experimentally [42, 78] near the photodetachment threshold, since the threshold behavior reveals information about the electron and neutral interaction. Wigner predicts that close above the threshold the cross section should rise proportional to k^{2l+1}, where k is the momentum and l the angular orbital momentum of the released electron [92]. Here he assumed only the long range interaction of the centrifugal potential of a spherical system. For s-wave transitions the threshold has a spectral dependence of

$$\sigma \propto \begin{cases} (E(\tilde{\nu}) - E_T)^{1/2} & \text{for } E(\tilde{\nu}) > E_T \\ 0 & \text{else} \end{cases}, \tag{3.29}$$

where E_T is the minimal needed photon energy to detach the electron by the transition T and $E(\tilde{\nu})$ is the photon energy at the wavenumber $\tilde{\nu}$.

But diatomic molecules do not have a spherical symmetry due to the internuclear axis. Furthermore dipole moments of such molecules interact with the electron and mix the partial waves of the electron by the angular orbital momentum l. For such angular wavefunction mixing the molecule needs to have a negative and positive parity [26]. Thus, such interaction occurs in the $^2\Pi$, but not in the $^1\Sigma$ state. The photodetachment transitions from OH^- to the $^2\Pi_{3/2}, J' = 3/2$ state of OH are calculated to rise by $(E(\tilde{\nu}) - E_T)^{0.28}$. The spectral dependence of the photodetachment transition changes also with the rotational excitation of the neutral [26]. Due to the Λ doubling there is a short spectral band for some transitions, where the other parity is energy forbidden. In this spectral range Smith *et al* [83] observed a threshold behavior of $(E(\tilde{\nu}) - E_T)^{0.42\pm0.04}$ comparable to the Wigner exponent of 0.5.

Measurements on OH^- photodetachment showed that the spectral dependence near-threshold can be modeled by a Wigner-type dependence

$$\sigma(\tilde{\nu}) \propto \begin{cases} (E(\tilde{\nu}) - E_T)^a & \text{for } E(\tilde{\nu}) > E_T \\ 0 & \text{else} \end{cases}, \tag{3.30}$$

using an exponent a in the range of $a = 0.2$ to 0.25 [65, 83]. For this thesis the exponent a is set for all transitions to the value of 0.2, which is sufficient to roughly predict the relative photodetachment cross sections near the EA.

To take also effects high above the photodetachment threshold into account we include a factor $(E(\tilde{\nu})/E_T)^{b-a}$ leading to a decrease of the photodetachment cross section for large kinetic energy release. Only a few data points are taken for the range high above the photodetachment threshold of OH^- indicating a maximum at about 16000 cm^{-1} [10, 40]. To match the spectral shape the factor b is set to -2.8 for the OH^- molecule .

Now the spectral dependence of the fine-structure thresholds is combined with the corresponding intensity $I_{J''}$ (see section 3.2.2). Since the rotational population is split between the single states (J, M) the rotational intensity $\hat{I}_{J''} = I_{J''}/(2J''+1)$ is weighted by the rotational degeneracy of the anionic state. Thus, the rotational-state-dependent relative cross sections are given by

$$\sigma_{T(J'')}(\tilde{\nu}) = \begin{cases} \hat{I}_{J''}(E(\tilde{\nu}) - E_T)^a (\frac{E(\tilde{\nu})}{E_T})^{b-a} & \text{for } E(\tilde{\nu}) > E_T \\ 0 & \text{else} \end{cases} . \tag{3.31}$$

The resulting photodetachment spectral intensities (see equation 3.31) for the OH^- molecule are plotted against the photon energies close to the electron affinity for

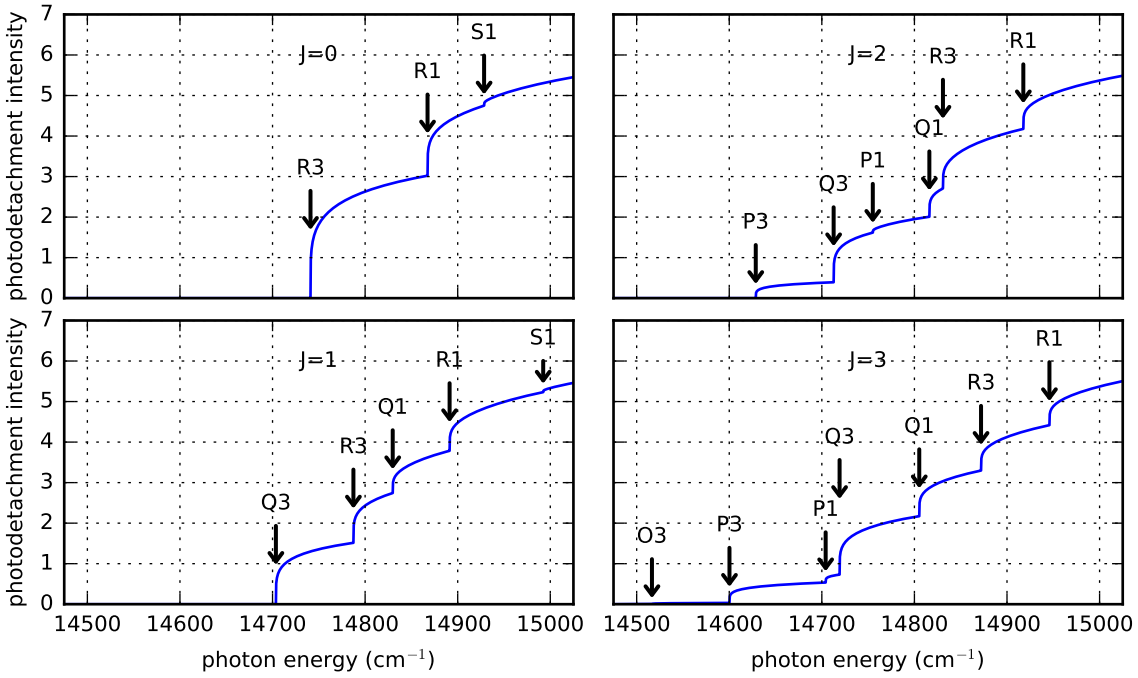

Figure 3.5: Spectral intensities (see equation 3.31) for photodetachment transitions are shown for the lowest four rotational states in the OH^- molecule. The thresholds are assigned by their corresponding transition (see notation 3.14).

the lowest four rotational states in OH^- (see figure 3.5). As we see in figure 3.5 the relative cross section rises in a stepwise behavior. The photon energy at which the first photodetachment threshold occurs reduces with the rotational excitation of the molecule (see figure 3.5). As a result, the addressed rotational states in the anion can be chosen by tuning the photon frequency for the photodetachment. Thus, rotational states in OH^- can be state-selectively probed.

3.2.4 Total cross sections

In order to model the photodetachment cross section we assign to each rotational state all allowed transitions (see section 3.2.1). For the ground state these are the $R3$, $R1$ and $S1$ transitions (see figure 3.3). In the next step we calculate the relative intensity for rotational fine-structure thresholds (see section 3.2.2). Those intensities are multiplied with a spectral dependence for photodetachment transitions to determine the rotational-state-dependent relative cross sections (see equation 3.31). Especially if a rotationally cold OH^- ensemble is photodetached near threshold, this assumption seems to be valid [65].

To model the total photodetachment cross section

$$\sigma^{tot}_{J''}(\tilde{\nu}) \propto \sum_{J''} \sigma_{T(J'')}(\tilde{\nu}) P_{J''}(t) \tag{3.32}$$

the state-dependent cross sections $\sigma_{T(J'')}$ are folded with the population distribution $P_{J''}(t)$. While the rotational-state-dependent cross sections depend only on the molecular properties, the total cross section varies with the population distribution

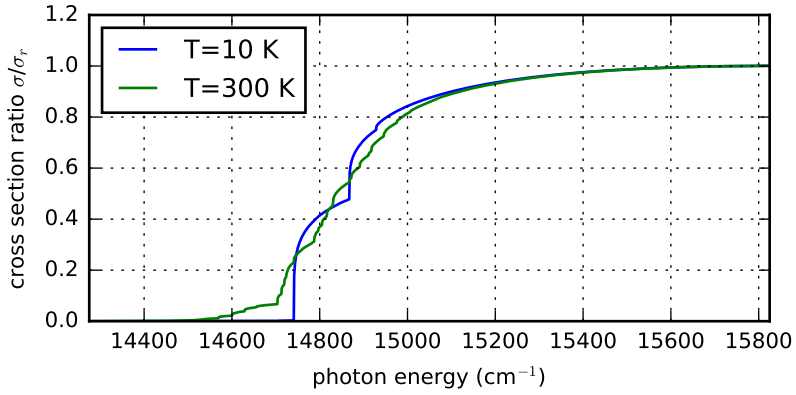

Figure 3.6: The modeled photodetachment spectrum of OH^- (see equation 3.32) is presented for a 10 K and 300 K rotational hot population distribution. Here the relative total cross section σ is normalized to the cross section σ_r at the helium neon laser line at 633 nm.

in the molecular ensemble. Thus, a higher rotational temperature broadens up the photodetachment threshold and reduces the energy needed for releasing the electron (see figure 3.6). If all OH^- molecules are in the ground state the number of observed fine-structure thresholds reduces to 3 corresponding to the $R3(0)$, $R1(0)$ and $S1(0)$ transition. Hence, cooling anions simplifies their photodetachment threshold structure and hence, the deduction of molecular properties like the EA (see figure 3.6).

To compare the modeled total cross sections for different exponents of a and b (see equation 3.31) they are normalized to a reference cross section high above the photodetachment threshold. At those photon energies the total cross section should theoretically be state independent (see figure 3.6). Thus, the photon energy determines the sensitivity of the total cross section to the population distribution. Experimentally the population-independence has been confirmed by total cross section measurements for OH^- at the helium neon laser wavelength 633 nm ($\tilde{\nu}_{HeNe} = 15754$ cm^{-1}) to a precision of 10% [10, 40]. Additionally experimental absolute cross section values at this wavelength are available for O^- [11, 40, 49], often used as a calibration molecule for cross section measurements [40]. Hence, it is reasonable to normalize th modeled relative cross section for OH^- to the cross section at the helium neon line by building cross section ratios σ/σ_r. Thus, the next chapter deals with the methods to measure cross section ratios for OH^- at several wavenumbers in dependence of the storage time in the CSR.

4 Photodetachment probing experiments: methods and results

As we have seen in chapter 3 the radiative cooling of OH^- molecules can be probed by photodetachment. The experimental technique to determine photodetachment cross section ratios are described in this chapter 4.

The first section 4.1 deals with the experimental setup of the CSR focusing on laser-ion beam interactions. Thus, the next section 4.2 connects the photon-induced neutralization reaction rates of OH^- to the photodetachment cross sections. Here the experimental technique is described to determine photon-energy-dependent cross section ratios over time by measuring photodetachment reaction rates of two lasers simultaneously. Then the reaction rates are analyzed by their time-of-flight spectrum and amplitude spectrum (see section 4.3). In the end of this chapter the cross section ratios are constructed from the reaction rates and fitted by a combined cooling and probing model (see section 4.4).

4.1 The Cryogenic Storage Ring

To measure the radiative rotational cooling the OH^- ions are stored in a collision-free environment with a low radiative background. Those properties are given in recently developed cryogenic electrostatic storage devices like the electrostatic Cryogenic Storage Ring (CSR) [32] at the Max-Planck-Institut für Kernphysik (MPIK) in Heidelberg. An overview about the experimental setup is given (see section 4.1.1) followed by a more detailed description of the laser setup used in the year 2015 (see section 4.1.2).

4.1.1 Experimental setup

In the CSR the ions are forced on a closed orbit of 35 m by a combination of several electrostatic deflectors (see figure 4.1). As we see in figure 4.1 the ion beam is bent in every corner by two 39° and 6° deflectors. The earth magnetic field and the maximum voltage at the electrodes roughly restricts the kinetic energy of ion beams between 20 and 300 keV per charge unit.

The experimental chambers of the CSR are cooled to several Kelvin by a liquid helium refrigerator system [32]. To decouple the experimental chambers from the

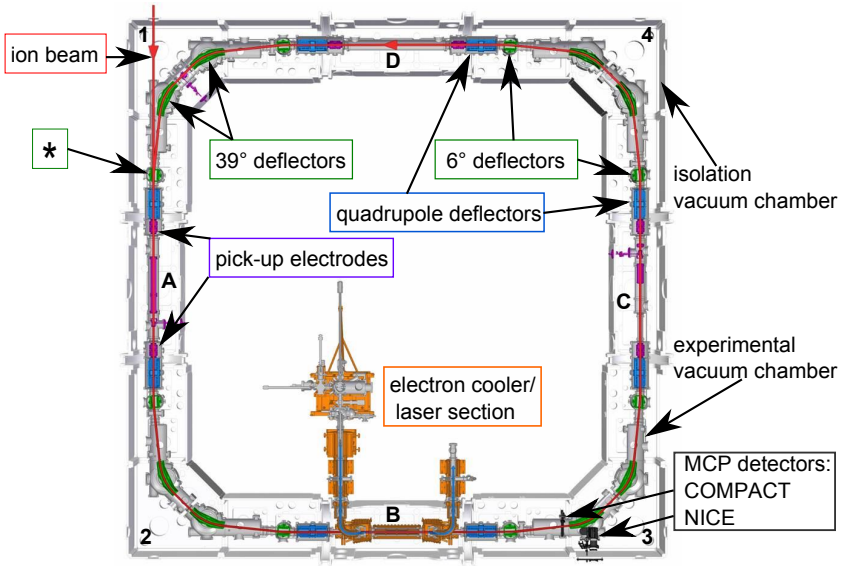

Figure 4.1: A schematic overview of the Cryogenic Storage Ring (CSR) at the Max-Planck-Institut für Kernphysik (MPIK) in Heidelberg is given. The corners and linear experimental section are numbered in the ion beam direction (anti-clock wise). In the year 2015 the section **B** included a laser setup which was altered in 2017 to implement also the electron cooler. The ion beam (red line) enters the CSR at corner **1** and encounters the first 6° deflector marked with a star (*).

laboratory environment they are enclosed in an isolation vacuum and surrounded by two stages of radiation shields to prevent heating by thermal radiation from room temperature surfaces. In cold operation a residual particle density in the experimental vacuum of lower than $5.8 \cdot 10^{-15}$ mbar [32] in room temperature equilibrium is reached. Thus, ion beams can be stored up to several hours. Hence, processes on the timescale of several 100 s can be observed like rotational cooling of OH^-. The cryogenic temperature at the experimental chambers drastically reduces the thermal radiation field in the CSR. As a result, infrared-active molecules can cool down to their lowest quantum states by interacting with the radiative environment in the CSR. Thus, the CSR is the perfect tool to observe processes of cold cations and anions under interstellar conditions.

To inject ions into the ring the CSR is connected to an ion source platform. On the platform the particle beam is produced for example in a Penning source or a Middleton Ion Sputter Source (MISS) [55] chosen for OH^-. If necessary, it is foreseen to accumulate and bunch the ions to increase the number of stored particles in the ring. The ions are accelerated with 20 to 300 kV and guided to the CSR by electrostatic and magnetic optical elements. In the transportation beamline an

electrostatic deflector (chopper) is switched to bunch the ion beam. This ion bunch is injected the CSR and stored by switching the first 6° deflector which the ions encounter (see figure 4.1). Up to several 10^8 ions can be stored in the CSR.

To study ions in the storage ring they interact in the experimental sections with neutrals (see linear section **A** in figure 4.1), electrons (see linear section **B** in figure 4.1) or photons (see linear section **B** in figure 4.1). The reactions in the CSR produces neutrals and charged particles with a charge-to-mass ratio different from the stored ions. The products leave the closed orbit of the CSR and are counted by MCP detectors in the corners (see corner **3** in figure 4.1).

The Neutral Imaging in Cold Environment (NICE) detector [32] is specialized in counting neutrals position sensitively and with high time precision. This is especially useful to time correlate events. The COld Movable PArticle CounTer (COMPACT) [47] can be moved quasi-perpendicularly to the ion beam, allowing to detect also charged product particles. Due to the single particle sensitivity even weak ion beams can be monitored by inducing interactions. Particularly photon-induced reactions are simple to implement by crossing the ion beam with a laser beam in the experimental chamber.

4.1.2 Laser setup of this experiment

To induce photon interactions the stored ion beam is overlapped with a laser beam. The laser enters and exits the CSR vacuum system by two sets of sapphire viewports (see figure 4.2). The viewports at the isolation vacuum chamber need to have an effectively larger view diameter, so that the shrinking of the experimental chamber during the cooldown of the ring can be compensated for by shifting the laser beam outside. The viewports at the experimental chambers withstand the large temperature range of 4 K to 250° C and have a sufficiently good heat conductivity to get a cold surface in the experimental chambers. Additionally the sapphire glass in optical quality transmits a large wavelength range of 250 nm to 6 μm. The spectral energy distribution of 300 K radiation has its maximum at around 15 μm (see figure 2.2). Thus, most of the 300 K radiation is blocked by the sapphire glass viewport.

To transport the laser in the isolation vacuum to the experimental chambers the radiation shields have small holes combined with tubes. Particles which try to enter the region between the radiation shields and the experimental chambers through the laser holes should freeze to the tubes before the particles reach the sapphire glass windows. Hence, the tubes reduce the amount of particle freezing to the viewports during the cryogenic operation.

In many experimental setups like in the CTF [48] the laser beam crosses the ion beam perpendicularly. Such a setup would result to relative small beam overlaps especially in the CSR due to its large circumference. To increase the interaction

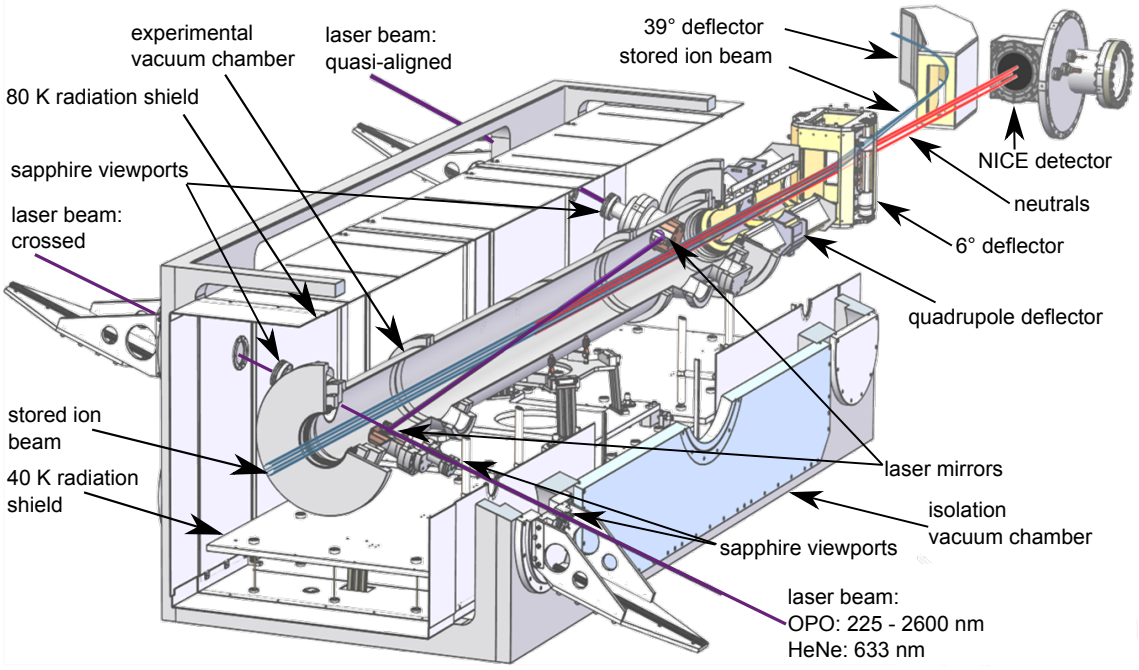

Figure 4.2: The interaction section in the CSR (see linear section **B** in figure 4.1) in the year 2015 is presented including the NICE in corner **3**. At this time the linear section **B** included only a laser setup. The anions in the section are neutralized a laser (purple line) in two different alignments: quasi-aligned and crossed. The neutrals travel through the 6° deflector and hit the NICE detector in corner **3**. The experimental chambers are surrounded by 40 K and 80 K radiation shields and by an isolation vacuum chamber.

probability of a photon the laser beam inside the experimental chambers is reflected by a mirror to graze the ion beam at angle of 3.4°. With a second mirror the laser is coupled out. As a result the overlap length along the ion beam is increased from $\sim$ 1 cm to $\sim$ 50 cm (see equation 4.7) which raises the absorption probability of a photon by a factor of $\sim$ 50. The mirror holders inside the experimental chambers are surrounded by a copper shield to prevent charging of the dielectric glass substrate and to protect the reflecting surface of the mirror. The mirror holders inside the experimental chambers keep the angle of the mirrors during the whole heating and cooling process sufficiently stable.

Since the dielectric mirrors inside the experimental chambers limit the wavelength range between 300 nm and 2000 nm, the copper shield around the entrance mirror holder has a hole to pass the mirror with the laser and hit the ion beam also perpendicularly. Thus, the laser setup possesses two types of laser-ion beam alignments: one quasi co-propagating (see laser beam: quasi-aligned in figure 4.2) and one per-

pendicular (see laser beam: crossed in figure 4.2).

This is the setup used in the beamtime for the measurements of this work, in the year 2015. It was later modified to allow experiments with the electron cooler.

4.2 Measuring cross section ratios

This section 4.2 deals with the technique to measure photodetachment cross section ratios at various photon energies over time. Therefore a concept is established to construct cross section ratios from two measured reaction rates (see section 4.2.1). The events at the detector are time-correlated with the laser pulse to separate reaction rates from two lasers quasi-simultaneously (see section 4.2.2). In the last section 4.2.3 a measurement time scheme is presented which facilitates time-correlation of photon-induced events and cycling of laser wavelengths.

4.2.1 Measured quantities

In the CSR relative cross sections $\sigma^{tot}_{J''}(\tilde{\nu})$ are measured by counting the number of reactions in the overlap region. The probability of absorbing a photon in the target volume with the particle density ρ_T and the overlap length l is given by

$$P_{\mathrm{OH^-}} = \sigma^{tot}_{J''}(\tilde{\nu})\rho_T l. \tag{4.1}$$

To approximate the probability of absorbing a photon the target density $\rho_T \approx N_{ion}/V_{\mathrm{CSR}} \approx 114\ \mathrm{cm}^{-3}$ in the CSR is estimated by the stored number of ions $N_{ion} \approx 10^7$ and the volume of the ion beam $V_{\mathrm{CSR}} = l_{\mathrm{CSR}}\pi r^2_{\mathrm{CSR}}$. Here, $l_{\mathrm{CSR}} \approx 35$ m is defined by the circumference of the ring and $r_{\mathrm{CSR}} \approx 5$ cm by the mean width of the ion beam in the overlap region. From geometrical considerations the overlap length is estimated by $l \approx 40$ cm. With the given absolute cross section $\sigma^{tot}_{J''}(\tilde{\nu}) \approx 10^{-17}\ \mathrm{cm}^2$ for the $\mathrm{OH^-}$ molecule (see reference [10]) the probability of absorbing a photon $P_{\mathrm{OH^-}} \approx 5 \cdot 10^{-14}$ is much smaller than one ($P_{\mathrm{OH^-}} << 1$).

In this thin target the photon flux $\Phi = dN_p/dt$ from the laser is not significantly screened in the overlapping volume and the number of interactions $N_{react} = PN_p$ is proportional to the number of photons N_p. Hence, the relative total cross section $\sigma^{tot}_{J''}(\tilde{\nu})$ can be linked to the laser-induced rate $R_p = dN_{react}/dt$ by

$$R_p(\tilde{\nu}, t) = \sigma^{tot}_{J''}(\tilde{\nu})\rho_T(t) l \Phi(\tilde{\nu}). \tag{4.2}$$

The overlap length l depends only on the geometrical overlap between laser and ion beam and the photon flux $\Phi(\tilde{\nu}) = I(\tilde{\nu})/(hc\tilde{\nu})$ is proportional to the laser intensity I. Hence, both properties are time-independent. But the ion beam density ρ_T inside the target volume decays over time due to ion loss processes and beam divergence.

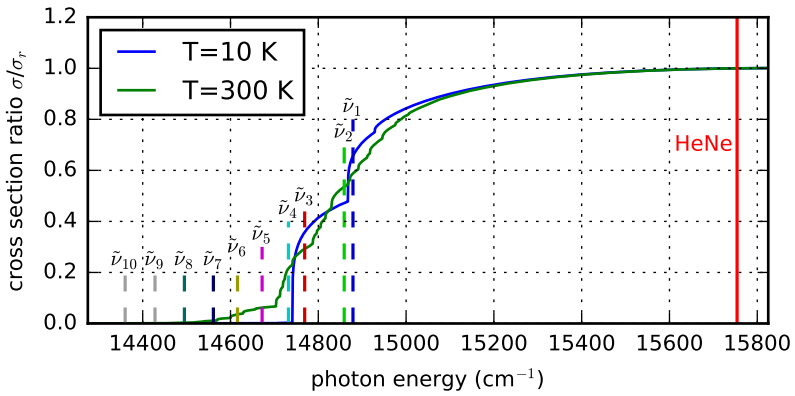

Figure 4.3: The modeled photodetachment spectrum of OH^- is presented for 10 K and 300 K thermal rotational distribution. While the helium neon laser (red solid line) far above the Electron Affinity is nearly independent of the internal excitation, the OPO laser (dashed lines) probes the rotational population changes near the threshold.

Thus, the particle density ρ_T is directly observed by a second photon-induced rate $R_r(\tilde{\nu}_r, t)$ at a photon frequency $\tilde{\nu}_r$ high above the photodetachment threshold. At those photon energies rotational-state-dependent relative cross sections $\sigma^{tot}_{J''}(\tilde{\nu}_r) = \sigma_r$ for all J'' are considered to be equal for all rotational excitations J'' leading to a population- (see figure 4.3) and time-independent total cross section

$$\sigma^{tot}_{J''}(\tilde{\nu}_r) = \sum_J \sigma_{T(J'')}(\tilde{\nu}_r) P_J(t) = \sigma_r \sum_J P_J(t) = \sigma_r. \tag{4.3}$$

If the rates $R_r(\tilde{\nu}_r, t)$ and $R_p(\tilde{\nu}, t)$ are measured at the same time in the same overlap volume, the rate ratio

$$\frac{R_p(\tilde{\nu}, t)}{R_r(\tilde{\nu}_r, t)} \frac{\Phi(\tilde{\nu}_r)}{\Phi(\tilde{\nu})} = \frac{\sigma^{tot}_{J''}(\tilde{\nu})}{\sigma_r} \propto \sigma^{tot}_{J''}(\tilde{\nu}) \tag{4.4}$$

weighted by the photon flux Φ is proportional to the total cross section ratio.

The obvious choice for the reference photon frequency $\tilde{\nu}_r$ is the helium neon laser line at 633 nm. The photon frequency $\tilde{\nu}_r = 15754$ cm^{-1} in the OH^- rest frame (see equation 4.5) is about ~ 1000 cm^{-1} above the Electron Affinity (EA) (see table 2.1). Close to this position several absolute cross section measurements have been conducted, indicating no dependence on the rotational population distribution [40].

In a second step the wavenumbers for probing the rotational distribution are chosen. Close to the EA the relative contribution of each state to the total cross section varies with the photon energy $\tilde{\nu}$ (see figure 3.5). The strength of each fine-structure

threshold in the photodetachment spectrum is proportional to the population of the corresponding rotational state. Hence, the rotational cooling of this state can be observed by monitoring the photodetachment rates just above and below the transition energy. Thus, with a small set of wavenumbers the cooling of the rotational population distribution can be measured. In this thesis the photodetachment spectrum is monitored at ten different wavenumbers $\tilde{\nu}_k \in \{14879, 14859, 14769, 14732, 14672, 14616, 14561, 14495, 14428, 14360\}$ cm^{-1} denoted by $k \in \{1,\ 2,\ \cdots,\ 10\}$ in descending order. The photon energies $\tilde{\nu}_k$ and the reference photon frequency $\tilde{\nu}_r$ (HeNe line) are presented in figure 4.3 which is an extension of figure 3.6. As we see in figure 4.3 the cross section at the laser probing lines $\tilde{\nu}_k$ close to the EA varies with the population distribution, but the cross section at the helium neon laser line $\tilde{\nu}_r$ stays constant.

The wavelength-tunable, ns-pulsed OPO laser system (EKSPLA NT342B) with a spectral width of $\Delta\tilde{\nu} \approx 5$ cm^{-1} is used to probe the photodetachment spectrum close to the EA. Close to a photodetachment transition the cross section rises rapidly with the photon energies (see figure 3.5). Thus, the rate $R_p(\tilde{\nu}, t)$ varies strongly with the photon frequency, even over the spectral width of the laser. To be insensitive to small photon frequency shifts, e.g. induced by the velocity distribution of the stored ions, the probing wavenumbers $\tilde{\nu}_k$ are set between the fine-structure thresholds. At those positions the cross sections are assumed to be flat over the spectral width of the laser (see figure 3.5) and effects of the line shape in the photodetachment signal can be neglected.

4.2.2 Detecting laser-induced neutralizing reactions

A technique to simultaneously induce and detect photon reactions at several wavenumbers is established. Therefore the ion beam is overlapped in the second straight experimental section with a laser beam consisting of a pulsed OPO laser and continuous helium neon laser in a quasi co-propagating manner (see beam: quasi-aligned in 4.2). The ions at velocity $v_{ion} = \beta c$ observe an electromagnetic wave at a frequency

$$\tilde{\nu}_{\mathrm{OH}} = \frac{\tilde{\nu}_L}{1 + \frac{\beta}{\cos(\alpha)}}, \tag{4.5}$$

which is Doppler shifted to the photon energy of the laser $\tilde{\nu}_L$ in the laboratory frame. Here, the coefficient $\cos(\alpha)$ takes into account the angle $\alpha \approx 3.5°$ between the laser and ion beam. The photons inside the CSR neutralize a small fraction of the anionic ensemble by photodetachment. Particles neutralized in the field-free experimental section **B** fly ballistically, leave the closed orbit of the CSR and are detected in the corner **3** by either one of the two MCP detectors (see figure 4.1). Here, the flight times of the neutrals to the detector 3 m downstream reflect the reaction positions in the field-free section.

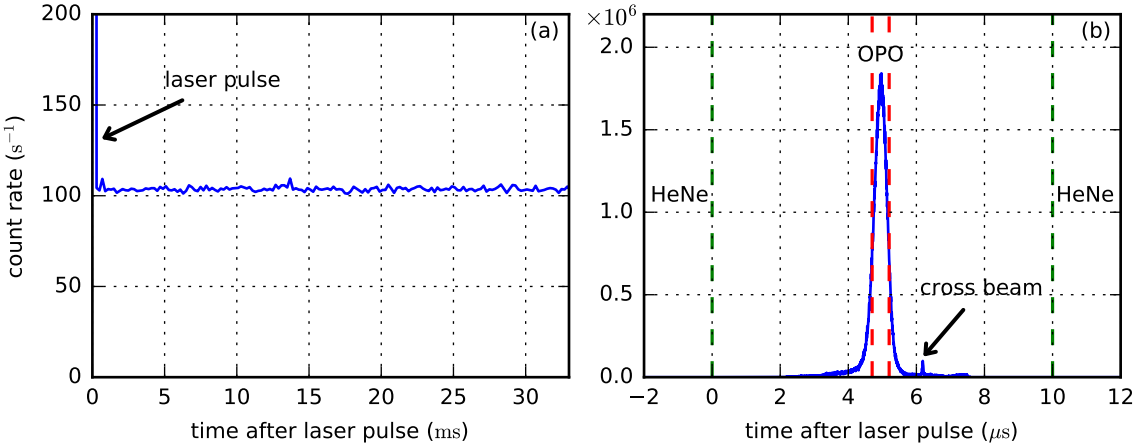

Figure 4.4: Both figures present the flight time of the neutrals induced by the pulsed OPO and continuously running helium neon laser in the overlap region to the detector. The helium neon laser randomly produces neutrals, leading to a flat distribution in figure (a). The neutrals induced by the pulsed OPO laser reach the NICE detector in a defined time range (see peak at 5 μs in figure (b)). The red vertical lines show the acceptance time range for pulsed correlated counts and the green lines the neglected time window for randomly induced neutrals.

To assign the neutrals to their induced laser the detection times are correlated to the ns-short OPO laser pulses. In the interaction time of the laser $t_{laser} = 3$–5 ns the OH^- ions with a kinetic energy $E_{kin} = 60$ keV and mass m_{ion} cover a distance of

$$l_{ion} = v_{ion} t_{laser} = \sqrt{\frac{2E_{kin}}{m_{ion}}} t_{laser} \lesssim 0.41 \text{ cm}. \tag{4.6}$$

Thus, the flight distance l_{ion} during the laser pulse is small compared to the overlap length $l \approx 40$ cm. Hence, the arrival times of the neutrals at the detector reflect their production position in the overlap region. For OH^- at a kinetic energy E_{kin} of 60 keV the ions reach the detector roughly after $t_{tof} \approx 5$ μs within a time spread of $\Delta t_{tof} \approx 0.6$ μs (see figure 4.4). Thus, the length of the overlap between the ion and the laser beam is given by

$$\Delta l_{tof} = \sqrt{\frac{2E_{kin}}{m_{ion}}} \Delta t_{tof} \approx 50 \text{ cm}. \tag{4.7}$$

A detailed analysis of the time-of-flight spectrum is given in section 4.3.1.

The time-correlation between the laser pulse and the detection of the photon-induced neutrals can be used to assign the counts at the detector to their corresponding laser. Around the main peak at 5 μs in the time-of-flight spectrum (see

figure 4.4) a time window between 4.7 μs and 5.2 μs is set (red lines in figure 4.4). Counts in this time range are assigned to the OPO laser. In the same way counts outside the green window between 0 μs and 10 μs (green lines in figure 4.4) are considered to be induced by the helium neon laser. Thus, the photon-induced rates of two laser can be separated quasi-simultaneously. The small acceptance window for the pulsed induced neutrals reduces the number of counts assigned to the OPO laser, but suppresses also the background rate from random processes by roughly six orders of magnitude. The time correlation of counts allows us to probe photon-induced processes over several orders of magnitude, although the dynamic range of the MCPs is reduced in the cold environment of the CSR [47].

For multiple hits in a short time window the detection system is limited by its dead time t_{dead}. The number of hits per laser pulse is called the multiplicity n. In the pulsed laser mode the NICE detector is chosen due to its short dead time of $t_{dead} \approx 6$ ns [32]. To avoid missing hits at the detector the number of neutralized ions n in one laser pulse is always kept small enough. Experimentally this is assured by limiting the number of photons per laser shot, so that the detection system always stays in the linear regime. If the system works in a non-linear regime, the shape of the time-of-flight spectrum flattens for higher multiplicity events. For OH^- ions at a kinetic energy of 60 keV the NICE detector system is linear even for events with ~ 10 hits per laser shot (see section 4.3.2).

If the multiple hit mode is compared to the single hit mode, the same statistical precision is reached in shorter measurement times. If the overlap length between ion and laser beam is increased, the time-of-flight spectrum broadens, allowing even more photon-induced reactions per laser shot. For lasers in continuous mode or quasi-continuous operation with a repetition rate of more than 1 kHz the COMPACT is the more reasonable choice due to its higher dynamic range and lower dark count rate compared to the NICE detector. For the OH^- experiment the NICE detector is chosen due to the low OPO laser repetition rate of $f_L = 20$ Hz.

4.2.3 Measurement time scheme

To monitor the internal energy distribution of the OH^- anion by photodetaching, the measurement time scheme needs to fulfill certain requirements. While the Continuous Wave (CW) helium neon laser with a fixed wavelength at 633 nm constantly produces neutrals, the OPO laser photodetaches the OH^- anions in the overlap region only during the laser pulse. Thus, OPO-laser-induced neutrals are expected to reach the MCP detector in a time range of around 0.6 μs. To observe a reasonable number of neutrals $n > 1$ during the laser pulse the signal of the detector is digitized with nanosecond resolution, but timescales of up to hours are monitored. Thus, the signal at the NICE detector is acquired in steps of $t_{st} = 33.55$ ms (see figure 4.5) and directly analyzed for pulse times and heights. This technique does

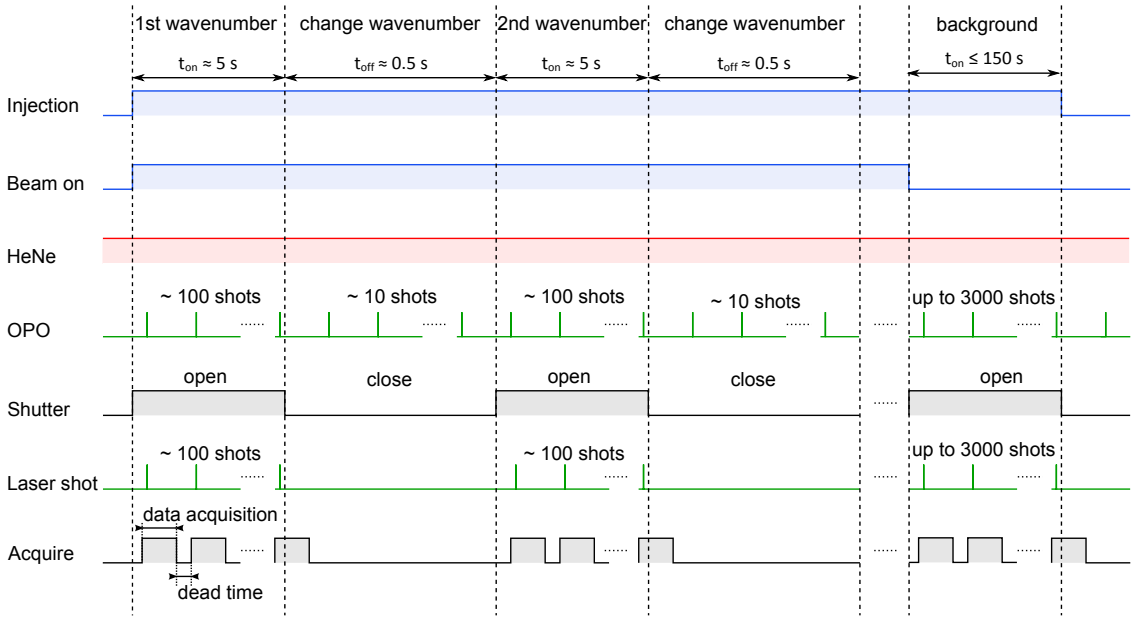

Figure 4.5: The timing of the control signals of the measurement scheme for one injection is presented.

not allow to continuously measure the MCP signal during the whole injection, but nanosecond time resolution is achieved in the steps.

Those steps are synchronized with the OPO laser trigger of $f_L = 20$ Hz (see figure 4.5), so that data acquisition initiated by the laser shot trigger (see Laser shot in figure 4.5) starts 10 μs before the laser pulse is shot into the CSR. Thus, counts induced by the OPO laser are always detected and phase shifts between laser pulse and step are prevented. The arrival times of the neutrals are given in respect to the start time of the step. Hence, the time distribution of the pulses in the steps corresponds to the time-of-flight spectrum of the neutrals to the detector only shifted by 10 μs. This fixed time structure between laser and step facilitates to assign the neutrals to their induced laser. Due to the dead times between the steps (see Acquire in figure 4.5) the measurement duty cycle $\mathrm{DC}_{acq} = t_{st} f_L$ in one injection is reduced to 0.67, neglecting dead times at the beginning and the end of each injection.

On purpose the injection of the ion beam is not synchronized to the pulsed OPO laser. Thus, the phase between the first laser shot and injection varies with each injection. Hence, the gaps in the measurement time which arise from the stepwise recording of the detector signal can be filled up by combining several injections. Thus, decays can be scanned faster than the laser repetition rate f_L. Additionally the binning of the data has not been set to a multiple of the laser frequency f_L.

While the background in the OPO laser signal is reduced by roughly 6 orders

of magnitude, the signal assigned to the CW helium neon laser inherits significant amounts of noise. Although pulse height discrimination significantly lowers the signal to noise ratio (see section 4.3.2), the background has to be subtracted from the helium neon laser signal. Hence, the ion beam is kicked out up to 150 s before the end of each injection and the count rate is measured with the same detector system. The measurement time for the background rate is 150 s for 1200 s, 50 s for 300 s and 5 s for 31 s storage time.

So far the time scheme allows to measure photon-induced rates from two lasers quasi-simultaneously over long storage times. To address several rotational states of the OH^- anion with the OPO laser, the wavelength is tuned during the experimental run. Each run consists of several injections. Normally the new wavenumber is set between the injections to interleave the wavelength change with the ion beam preparation to increase the duty cycle. At the CSR the storage times are large against the breaks between the injections. Additionally averaging gets more reliable, if wavenumbers are iterated shorter in time. Thus, the measurement time scheme allows to change the wavelength during the injection (see figure 4.5). However this reduces the measurement duty cycle, because no data can be acquired during the wavelength change for 0.6 s. Thereby one avoids measuring counts from laser pulses with unknown photon energy. The OPO laser beam is blocked during the wavelength change by a shutter and the laser shot trigger is stopped, so that no step is acquired in between two wavelengths (see figure 4.5). To reach at least a total measurement duty cycle $\mathrm{DC}_{tot} = \mathrm{DC}_{\tilde{\nu}} \cdot \mathrm{DC}_{acq} > 0.5$ the wavenumber cycle period is set to minimum 3.6 s. Thus, a reasonable measurement duty cycle is achieved, although photon frequency cycling is allowed during the injection.

4.3 Analyzing photodetachment rates

This section deals with the methods to analyze the measured photodetachment rates. Here, the time-of-flight spectrum 4.3.1 and the amplitude spectrum 4.3.2 are discussed. Furthermore the continuously acquired rates are checked for non-random noise (see section 4.3.3).

4.3.1 Time-of-flight spectrum

For the OH^- experiment the laser beam consists of a pulsed OPO and a continuous helium neon laser. Both lasers photodetach the OH^- molecule in the overlap region and produce a neutral rate at the NICE detector. The flight time to the detector depends on the position of the photodetachment reaction in the overlap region (see section 4.2.2). To measure the time-of-flight spectrum the reaction time is linked to the detection time by synchronizing the data acquisition with the laser pulse.

As mentioned in section 4.2.3 the data is acquired in steps which are initiated by a laser shot trigger 10 μs before the laser pulse. The detection time of the neutrals is measured by the pulse at the MCP detector. The time of the pulse is given with respect to the beginning of the step. By summing up all steps in one experimental run and shifting the start time of the steps by 10 μs the time-of-flight spectrum is revealed (see figure 4.4). To analyze the flight spectrum it is split at 20 μs into two parts.

As we see in figure 4.4(a) the time-of-flight spectrum after 20 μs is constant. Thus, the neutrals are randomly produced to the laser pulse, which results mainly from the continuously running helium neon laser. The figure 4.3.1(b) is dominated by a peak at around $\sim$ 5 μs after the laser shot. This peak results from the neutrals produced in the overlap region by the pulsed OPO laser. This peak has long tails which expand from nearly $\sim$ 2 μs to $\sim$ 8 μs. If these counts are induced by the OPO laser, the corresponding positions are far from the estimated overlap region. But their positions are still located in the linear section **B**. Stray light produced at the sapphire windows may lead to neutralization far from the overlap region. If an anion is neutralized outside the linear section, the neutral trajectory does not hit the NICE detector. Thus, the electrostatic configuration limits the time range of the laser pulse correlated counts between $\sim$ 2 μs and $\sim$ 8 μs. Hence, all counts outside of this time range are produced by random processes. Thus, it is reasonable to set the neglected time region for the helium neon laser between 0 μs and 10 μs after a laser pulse (see figure 4.4(b)).

The figure 4.4(b) reveals also a small peak at 6 μs. If the time between both peaks is translated into position in the field free region, the neutrals are produced $\sim$ 1 m ahead of the overlap region. The laser setup at the CSR has two options. In the first configuration the laser passes the mirror and hits the ion beam perpendicularly. In the second configuration the laser is reflected by the mirror to overlap with the ion beam in grazing configuration (see figure 4.2). Thus, light which passes the mirror hits the ion beam $\sim$ 1 m before the considered overlap region. Those effects can happen if the laser is not perfectly aligned or light is diffracted at an iris shutter close to the CSR entrance.

All photodetachment reactions outside the overlap region produce neutrals at a different angle between the laser and the ion beam. Thus, the photon frequency in the ion rest frame changes due to the Doppler effect (see equation 4.5). As a result a small acceptance range around the main peak between 4.7 μs and 5.2 μs is set to keep the photon angle distribution sufficiently small (see figure 4.4(b)). This change of the incident angle happens also, if the ions are photodetached with the helium neon laser. But the total cross section around the helium neon laser line high above the threshold varies slowly within the Doppler frequency shift (see figure 4.3). Additionally the total cross section in this photon energy range stays independent of the population distribution. Hence, the rate ratio weighted by the photon flux

(see equation 4.4) remains proportional to the total cross section.

In a nutshell the time-of-flight spectrum is a crucial tool to separate count rates, to suppress the background and to assure a constant observed photon frequency in the ion rest frame at one laser line.

4.3.2 Pulse amplitude discrimination

By time-correlation the pulsed induced counts are separated from the randomly distributed events. While the background in the pulsed photodetachment signal is reduced by the short observation time of 0.5 μs (see figure 4.4), the signals from the continuously running helium neon laser inherit various types of background. To reduce the background rate induced by dark counts at the NICE detector the pulses are discriminated by their amplitude.

The voltages at the NICE detector are set, so that the intensity of the pulse at the MCP varies with the type of impact. Heavy particles like molecules produce multiple free electrons on impact, while photons can release only one electron. The amplitude distribution of the dark counts differs significantly from the molecular one (see figure 4.6). While the dark count rate decreases rapidly with the pulse amplitude, the molecular impact leads to a bump in the amplitude spectrum. This bump is best observed in the amplitude spectrum of the pulsed induced laser counts due to its better signal-to-noise ratio (see figure 4.6(b)). The background rate in the photodetachment signal is significantly reduced by setting an acceptance interval

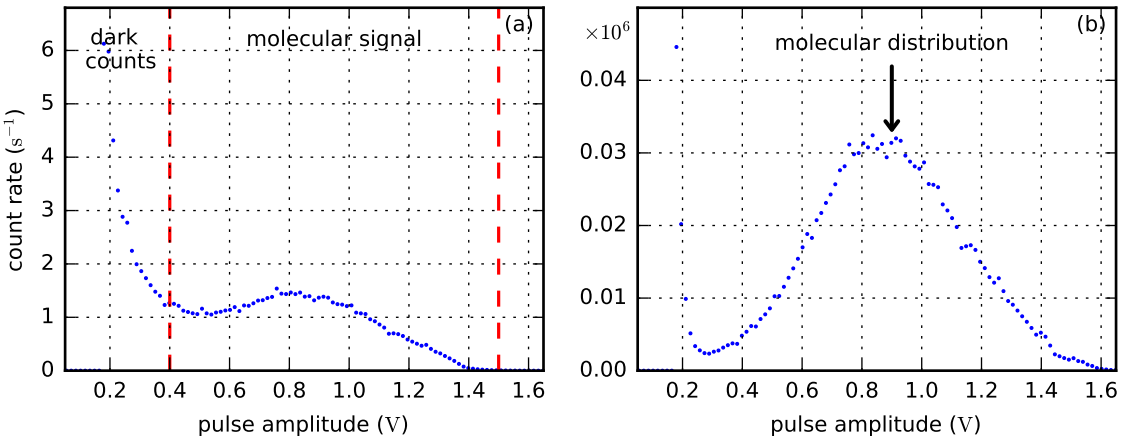

Figure 4.6: The pulse amplitude distribution at the NICE detector is presented for the two laser-induced signals. The counts assigned to the helium neon laser (outside the green dashed line in figure 4.4(b)) are shown in figure (a). The amplitude distribution for MCP pulses between the red dashed lines in figure 4.4(b) is revealed in figure (b).

for the pulse amplitude. The noise reduction in the signal at the helium neon laser line has a higher priority. Thus, the acceptance interval between 0.4 V and 1.6 V is based on the amplitude distribution for the continuously detected signal.

The amplitude distribution is a well established method to check for saturation effects at the detector. Thus, the amplitude distribution and the time-of-flight spectrum are split up according to the multiplicity n of the pulsed laser event (see figure 4.7). If saturation takes place the peak in the time-of-flight spectrum flattens and the pulse amplitude distribution shifts to lower intensities. While the time-of-flight spectrum shows no significant changes in the time discriminated window (see figure 4.7(a)), the maximum of the bump in the amplitude spectrum shifts to lower amplitudes (see figure 4.7(b)). The amplitude distribution consists of a dark count and a molecular impact distribution. If the signal-to-noise ratio increases, the combined maximum of both functions shifts to lower amplitudes. Although an amplitude shift in the maximum is observed, the detector seems to work in the linear regime.

To be safe the maximum number of count per laser shot is set to 20. Steps with more time correlated counts exceed the 3σ deviation, if the mean multiplicity per laser shot is $n = 10$. Additionally those steps with more than 20 counts per laser shot have a higher probability to be affected by non-random distributed noise (see section 4.3.3).

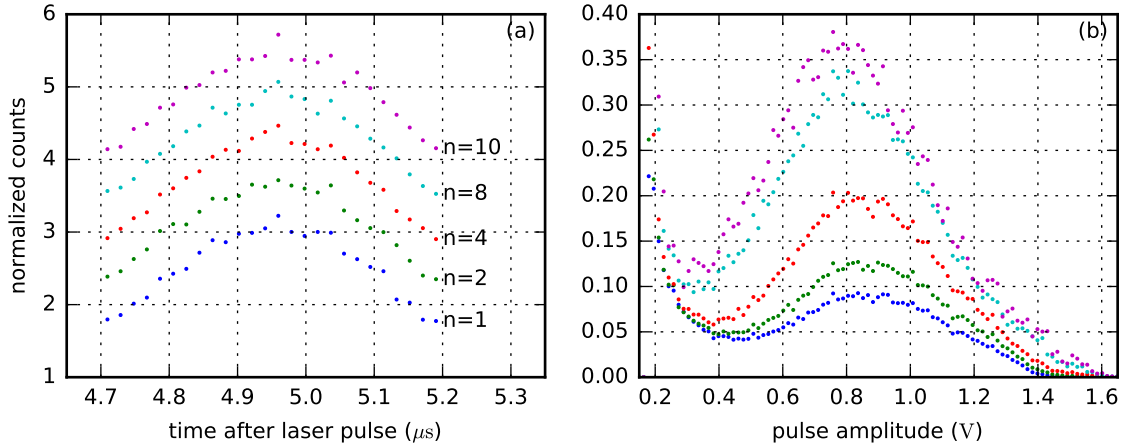

Figure 4.7: The time-of-flight spectrum (a) in the pulsed induced acceptance window (see red dashed lines in figure 4.4(b)) and the pulse amplitude distribution (b) (see figure 4.6(b)) at the NICE detector is presented for laser pulses with different multiplicities n.

4.3.3 Non-random noise

Randomly distributed noise can be subtracted by measuring the background signal afterwards, but non-random noise can lead to systematic shifts in the data. Thus, the counts induced by the helium neon laser are statistically investigated for non-random effects. The event rate for two following counts is plotted against the time Δt between those. For a random distribution this Δt distribution is flat, if the observed time interval is much shorter than the step length (see figure 4.8(a)). Non-random behavior is seen at times smaller than 3 μs (see figure 4.8(b)). This noise might result from electromagnetic waves coupling into the detector system leading to time correlated multiple counts. To avoid systematic errors in the data counts with a time distance of less than 3 μs are ignored in the count rate assigned to the helium neon laser. The OPO-laser-induced counts are already time correlated by the laser pulse. Thus, this cut can not be applied here.

In the section 4.3 the time-of-flight spectrum the amplitude and the Δt distribution were analyzed. The time-of-flight spectrum is crucial to separate counts and to assure the right incident angle between the laser and the ion beam. The amplitude cut increases significantly the signal-to-noise ratio in the helium neon laser signal. The Δt cut suppresses time steps with unexpectedly high count rates in the continuous signal. The effect of the Δt cut is rather small.

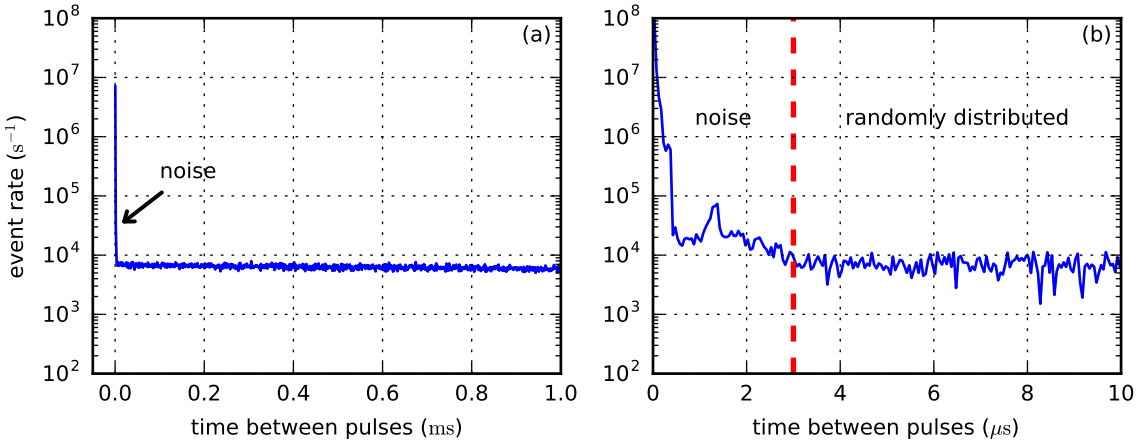

Figure 4.8: The event rate of two following pulses at the MCP in one step is plotted against their time distance Δt. To avoid time correlation with the laser pulse the time window between the green vertical lines in figure 4.4(b) is disregarded. If the processes are randomly distributed and the times are much shorter than the step length, the Δt distribution is flat. Hence, the red vertical dashed line separates time-correlated noise from random processes.

4.4 Analysis technique

In this section the photodetachment rate $R(\tilde{\nu}_k, t)$ at the probing wavenumbers $\tilde{\nu}_k$ is normalized by the rate $R(\tilde{\nu}_r, t)$ at the reference photon frequency (see section 4.4.1) and fitted with a combined probing and cooling model (see section 4.4.2). This model includes already experimental effects, which are discussed in section 5.2.

4.4.1 Constructing the photodetachment signal

To reconstruct the population of the rotational states the photodetachment rates $R(\tilde{\nu}_k, t)$ are measured at different photon frequencies $\tilde{\nu}_k$. Hence, the laser wavelength is cycled during the storage time. Different wavelength schemes per injection are applied to derive a complete set of photon energies at all storage times. The number of the schemes coincides with the number of the used photon energies.

First all injections with the same wavelength scheme are summed up by using a bin size of 0.3 s for 31 s, 3 s for 300 s and 15 s for 1200 s storage time. Due to our experimental background from O^- (see section 5.2) the number of counts N in all bins is high enough to calculate the statistical error by $\Delta N = \sqrt{N}$ and to apply Gaussian error propagation. Furthermore the summed counts are divided by the number of steps per bin.

Additionally the dark count rate at the detector is measured in the beam-off time and subtracted from the helium neon laser signal. No dark count rate subtraction is needed for the pulsed induced signal.

In the next step the rate assigned to the OPO laser $R(\tilde{\nu}_k, t)$ is normalized by the signal at the helium neon laser line $R(\tilde{\nu}_r, t)$. As equation 4.4 predicts the rate ratio $R(\tilde{\nu}_k, t)/R(\tilde{\nu}_r, t)$ is independent of the number of ions in the ring. Thus, variations on the number of injected ions cancel out in the rate ratios. Now the rate ratios $R(\tilde{\nu}_k, t)/R(\tilde{\nu}_r, t)$ are combined to get a full time coverage at all wavelengths. Here, the rate ratios are averaged by weighting them with their corresponding number of steps per time bin. Thereby the measurement time per bin is considered.

Thus, one receives measured rate ratios, also called the photodetachment signals S_k with $k \in= \{1,\ 2,\ \cdots,\ 10\}$, at the wavenumbers $\tilde{\nu}_k \in \{14879,\ 14859,\ 14769,\ 14732,\ 14672,\ 14616,\ 14561,\ 14495,\ 14428,\ 14360\}$ cm^{-1} for CSR run 108, 109, 121, 123, 125 and 127 (see figure 4.9). Since the signals $S_{9,10}$ are neither used in the fit nor in the argumentation, we ignore them in the further context.

4.4.2 Fit parameters and fitting method

The data in figure 4.9 are used to determine the cooling of the rotational population distribution. In this section 4.4.2 the photodetachment signals $S_k(t) =$

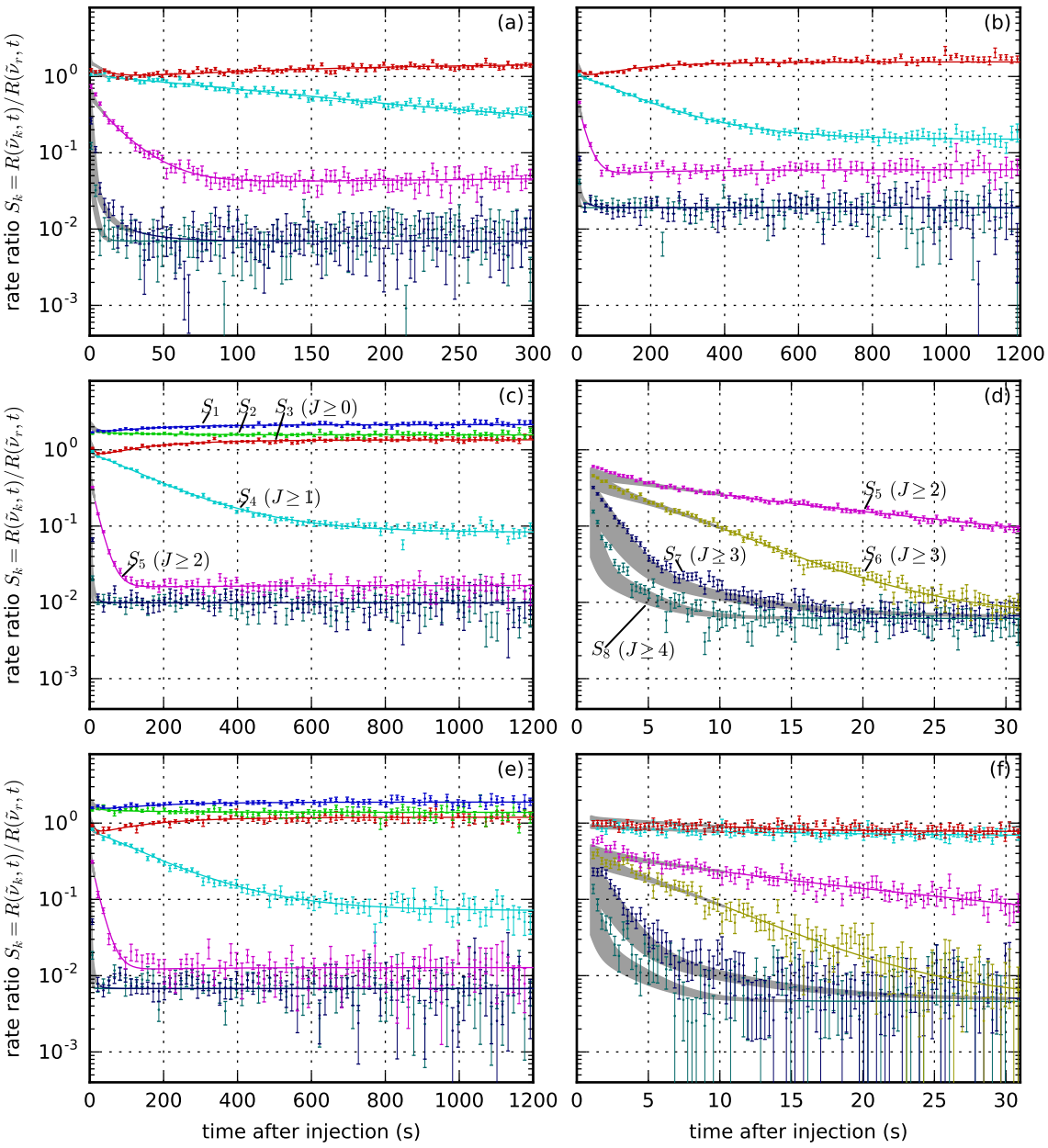

Figure 4.9: Photodetachment rates of the OPO laser $R(\tilde{\nu}_k, t)$ normalized to the helium neon laser $R(\tilde{\nu}_r, t)$ are plotted against the storage time in the CSR for the run 108(a), 109(b), 121(c), 123(d), 125(e) and 127(f). Each color corresponds to one photon energy $\tilde{\nu}_k$. The rate ratio $S_k = R(\tilde{\nu}_k, t)/R(\tilde{\nu}_r, t)$ is the key quantity measured in this thesis (see equation 4.4). The data points are fitted by a combined cooling and photodetachment model (see lines). The grey shaded areas give the model variation for a 1000 K to 6000 K rotational hot start population and are not considered in the fit.

$R(\tilde{\nu}_k, t)/R(\tilde{\nu}_r, t)$ are fitted by a combined cooling and probing model. The signals $S_k(t)$ are a linear combination of rotational populations $P_J(t)$ (see equation 3.32), where the rotational-state-dependent cross sections $\sigma_{k,J} = \sigma_J(\tilde{\nu}_k)$ (see equation 3.31) are its linear coefficients. In vector representation the fit function is represented by

$$\vec{S}(t) = b\hat{\sigma}\vec{P}(t). \tag{4.8}$$

Here, each row of the cross section matrix $\hat{\sigma}$ corresponds to one photon energy $\tilde{\nu}_k$ and each column to one rotational state J. While the cross section matrix $\hat{\sigma}$ is a molecular property, the scaling factor b can vary between the runs due to changes in the laser and detector setup. Hence, the parameter b is fitted for every run separately.

The rotational population is modeled by a linear set of differential equations (see equation 2.67) calculated by the exponential matrix equation

$$\vec{P}(t) = e^{\hat{A}t}\vec{P}_0 \tag{4.9}$$

using the Padé approximation implemented in the Python SciPy package. Here, the matrix $\hat{A}$ includes as fit parameters the Einstein coefficients $A_{J+1\to J}$ and the photon occupation numbers $n_{\tilde{\nu}_{J\to J+1}}$ for the resonant transitions.

From other experiments with the MISS the start population P_0 is estimated to be several 1000 K hot [53]. Thus, the data is fitted for a set of start populations varying between $T_0 = 1000$ K and $T_0 = 6000$ K. To include all significant population at all times the cooling is calculated up to the rotational quantum state $J = 50$. Thus, a population $P_J < 10^{-4}$ for $J > 50$ is received in the upper temperature limit of 6000 K. The start population affects only the cooling behavior at short storage times, since the rotational levels decay in a cascading manner (see section 2.4). Hence, threshold times are set at which the population in certain states can be disregarded for the signal calculation.

The fast decay of the signal S_8 reveals that all states $J \geq 4$ have decayed after 10 s (see figure 4.9). Thus, the signals after 10 s can already be modeled with four state-dependent cross sections per photon energy. Furthermore the cross sections for forbidden transitions are set to zero. Hence, the complete rotational cooling after 10 s storage time can be fitted with a small set of parameters in the cross section matrix $\hat{\sigma}$ (see table 4.1). All non-significant state-dependent cross sections are set to their modeled values.

The quality of determining the state-dependent cross section depends on the characteristic rotational cooling of the OH^-. Due to the stepwise cooling time ranges can be defined at which cross sections are sensitive to. The cross sections of the rotational state $J = 3$ can only be determined, if sufficient statistics is available in the time range between 10 s and 30 s. Under this consideration the signals $S_{1,2}$ are

Table 4.1: The pulse energies of the OPO laser and the fitted positions in the cross section matrix are given. The state-dependent cross section at signal S_3 detaching the state $J = 0$ is set to its modeled value (red text).

OPO laser			cross section ratio $\sigma_J(\tilde{\nu}_k)/\sigma_r$			
k	$\tilde{\nu}_k$ (cm^{-1})	pulse energy (mJ)	$J = 0$	$J = 1$	$J = 2$	$J = 3$
1	14879	11.6	fitted	fitted	fitted	not fitted
2	14859	11.6	fitted	fitted	fitted	not fitted
3	14769	11.2	fixed	fitted	fitted	fitted
4	14732	10.8	0	fitted	fitted	fitted
5	14672	10.3	0	0	fitted	fitted
6	14616	10.7	0	0	0	fitted
7	14561	10.4	0	0	0	not fitted
8	14495	10.3	0	0	0	0

fitted after 30 s and signals $S_{3,4,5,6}$ after 10 s. A full set of the fitted state-dependent cross section is given in table 4.1.

To take into account the different photon flux at the probing wavenumbers $\tilde{\nu}_k$ each row in the cross section matrix $\hat{\sigma}$ is scaled by the corresponding photon flux (see table 4.1). The photon flux is inferred from the OPO laser intensity. To gain the relative cross section the fitted values for the matrix elements are scaled back. By this method the error of 3% on the laser intensity is included in the relative cross section calculation, but not in the fitting process. Thus, additional errors on the radiative lifetimes are avoided.

In the next step the relevant Einstein coefficients are defined. After 10 s storage time three different decay rates are observed in the photodetachment signals (see figure 4.9). Those three decays correspond to the lifetime of the three lowest rotational excitated states ($J = \{1,\ 2,\ 3\}$) in the OH^- molecule. Thus, the Einstein coefficients for those states can be fitted separately. The rotational cooling of all higher states is modeled by using the fitted transition dipole moment in the rotational level $J = 3$.

Futhermore a reasonable set of fitted photon occupation numbers is chosen. Including the effect of laser reflection (see section 5.2) only the lowest two states reveal significant population in the steady state. Thus, only one photon occupation number can be fitted. If the photon field is in thermal equilibrium, the photon occupation number follows the Bose-Einstein statistics. Hence, the photon occupation ratio n_2/n_1 where the photon energy E_2 is greater than E_1 ($E_2 > E_1$) monotonically increases with the temperature. Hence, a thermal distribution determined by the occupation number at the lowest frequency gives a minimum value for the radiative

field at all other transitions. Thus, the radiation field is fitted by a temperature T_{eff} instead of the photon occupation number $n_{\tilde{\nu}_{0\to1}}$.

Including also the experimental effects of reflection and O^- contamination the fit function has the form

$$\vec{S}(t) = b\hat{\sigma}\vec{P}(t) + R\hat{\sigma}_R\vec{P}(t) + c_{O^-}, \tag{4.10}$$

where R is the reflection coefficient, $\hat{\sigma}_R$ the theoretical cross section matrix at the positively Doppler shifted frequency and c_{O^-} the photodetachment rate induced by O^- (see section 5.2). The resulting fits and the photodetachment signals of all runs are given in figure 4.9. Independent of the start temperature a reduced mean chi squared of $\chi^2_{red} = 1.30$ is reached.

Before the results of this fit can be analyzed in the next chapter the effect of the start population has to be discussed. Although the first 10 s are excluded in the fitting process, the temperature of the start population varies some fit parameters significantly. Thus, the start temperature is considered as a systematic uncertainty. As we see in figure 4.9 the upper limit ($T_0 = 6000\ K$) of the grey shaded areas fits best at short storage times. Hence, the fit with $T_0 = 6000\ K$ is considered to be the optimal fit. Thus, the values analyzed in the next chapter are taken from this fit. To take into account the start temperature dependence in the parameters the fits at $T_0 = 4000\ K$ and $T_0 = 6000\ K$ are compared. The systematic shift in the fitted values is our measurement for the uncertainty in the start temperature, which is added to the statistical uncertainties.

5 Photodetachment probing experiments: analysis

In section 5.1 the photodetachment rate at the reference wavenumber $\tilde{\nu}_r$ is analyzed for ion beam lifetimes, laser depletion and population effects. Furthermore the photodetachment signals in figure 4.9 are investigated for experimental effects (see section 5.2). The fit results for the cooling model are presented in section 5.3, revealing rotational lifetimes of up to $193(3)_{\mathrm{stat}}(3)_{\mathrm{sys}}$ s (see table 5.4). Due to the cooling dynamics also state-resolved cross sections are determined (see table 5.5). The concept of using the correlation between the radiative cooling rate and internal excitation is discussed and the cross section results are compared to the model in figure 3.5 (see section 5.4).

5.1 Photodetachment at the reference wavenumber

In contrast to room temperature storage devices the ion beam decay in the CSR can not be monitored by detecting neutrals from residual gas collisions. Thus, the ion beam dynamics for the OH^- molecule are measured by overlapping the negative ion beam with a co-propagating helium neon laser beam. In the ion rest frame the helium neon wavelength at $\lambda_r = 633$ nm is shifted to a photon frequency of $\tilde{\nu}_r = 15754$ cm^{-1}. This wavenumber $\tilde{\nu}_r$ is about ~ 1000 cm$^-$ above the photodetachment threshold. Thus, the cross section at this wavelength σ_r is predicted to be independent of the rotational excitation in the OH^- molecule (see section 3.2.4). Hence, the photodetachment rate at the reference wavenumber $\tilde{\nu}_r$ is a relative measurement for the number of ions N_T in the overlap region. If the ion density in the overlap region is proportional to the number of ions N_{ions} in the ring, the neutral rate induced by photodetachment

$$\left.\frac{dN_{ion}}{dt}\right|_{laser} = -k_r N_{ion} \tag{5.1}$$

observes the decay process of the ion beam. Here the decay rate k_r depends linear on the cross section σ_r, the laser intensity I_r and on the overlap between ion and laser beam. As a result, the beam lifetime can be measured by monitoring the photodetachment at the reference frequency $\tilde{\nu}_r$ (see section 5.1.1).

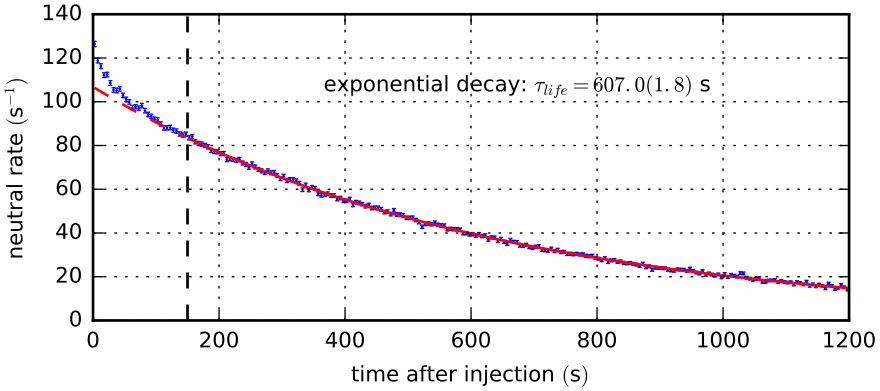

Figure 5.1: The neutral rate at the NICE detector induced by the helium neon laser is plotted against the time after injection. The exponential fit (red line) of the data points after 150 s reveals a beam lifetime of $\tau_{life} = 607.0(1.8)$ s.

The laser beam itself induces an additional decay process on the stored negative ion beam (see equation 5.1), which is investigated in section 5.1.2. All measurements in this thesis rely on the assumption that the photodetachment cross section at the reference wavenumber $\tilde{\nu}_r$ is independent of the rotational population distribution. This assumption is tested in section 5.1.3 by searching for rotational cooling effects in the ion beam decay.

5.1.1 Beam lifetime

To monitor the decay process of the ion beam with the helium neon laser the effective laser intensity in the interaction region is set to $I_{HeNe} = 0.7$ mW. Thereby a reasonable rate of around $R_r \approx 100$ s^{-1} at the NICE detector is reached. This neutral rate induced by photodetachment exponentially decays after 150 s (see figure 5.1). Thus, the loss processes in the CSR can be described by a linear rate model

$$R_{loss} = -\frac{dN_{ion}}{dt} = k_{life} N_{ion}. \tag{5.2}$$

Here R_{loss} is the ion loss rate and k_{life} represents the exponential decay rate, which is the inverse of the beam lifetime $\tau_{life} = 1/k_{life}$. For run 121 a beam lifetime of $\tau_{life} = 607.0(1.8)$ s is fitted for long storage times ($t > 150$ s) (see figure 5.1). Such beam lifetimes are sufficient to observe the radiative rotational cooling of OH^- molecules to equilibrium.

For short storage times the neutral rate induced by the helium neon laser behaves non-exponentially (see figure 5.1). This effect may be caused by non-linear ion losses in the ring ($R_{loss} \not\propto N_{ion}$) or by transversal ion density changes in the overlap

region ($N_{ion} \not\propto N_T$). In the first case ($R_{loss} \not\propto N_{ion}$) the neutral rate still provides a relative measurement for the number of stored ions N_{ions}. But in the second case ($N_{ion} \not\propto N_T$) the ratio N_T/N_{ion} changes during the storage time.

To calibrate the photodetachment rates induced by the OPO laser a measurement for the number of ions in the overlap region is needed. Thus, a normalization to the number of ions in the ring may be insufficient. But non-linear storage effects are intrinsically corrected by dividing the rates induced by the OPO laser by the photodetachment signal at the reference wavenumber. Hence, the rate ratio (see equation 4.4) is robust against most storage effects.

5.1.2 Laser depletion

The laser beam in the CSR neutralizes a small fraction of the OH^- anions in the overlap region. Thus, an additional decay process is induced, which shortens the lifetime of the ion beam in the storage device. The laser depletion is quantified by tuning the laser intensity.

In a separate measurement only the helium neon laser is operating. By a shutter the laser beam is switched on and off during the storage time with a duty cycle of DC = 0.5. If the laser depletes the ion beam, the lifetime in the laser on-phase is reduced. Thus, the laser-induced decay rate k_L can be disregarded, if the measurement points in a logarithmic plot lie on a straight line (see figure 15 in [32]). Hence, the uncertainty of the measured lifetime $\tau_{life} = 425(9)$ s in reference [32] gives an upper limit for the laser-induced decay rate

$$k_L < \frac{\Delta\tau_{life}}{\tau_{life}^2} \approx 5 \cdot 10^{-5} \text{ s}, \tag{5.3}$$

which corresponds to a laser-induced lifetime of $\tau_L \gtrsim 2 \cdot 10^4$ s ≈ 5.6 h

This laser-induced lifetime is applied to the OH^- experiment discussed in this thesis. In both measurements the helium neon laser is operating at the same intensity and in grazing configuration with the ion beam. Thus, the laser-induced decay rate k_L weighted by the duty cycle DC gives an upper limit for the depletion rate induced by the helium neon laser:

$$k_L^{\text{HeNe}} = \frac{k_L}{\text{DC}} \lesssim 10^{-4} \text{ s}. \tag{5.4}$$

In the next step the laser-induced decay rate of the OPO laser is modeled. Both lasers are applied in the same overlap region. Hence, the neutral rates $R_p(\tilde{\nu}, t)$ and $R_p(\tilde{\nu}_r, t)$ (see equation 4.2) differ only by the applied photon flux $\Phi(\tilde{\nu})$ and by the total cross section $\sigma_J^{tot}(\tilde{\nu})$. The photon flux ratio $\Phi(\tilde{\nu})/\Phi(\tilde{\nu}_r)$ between both lasers is

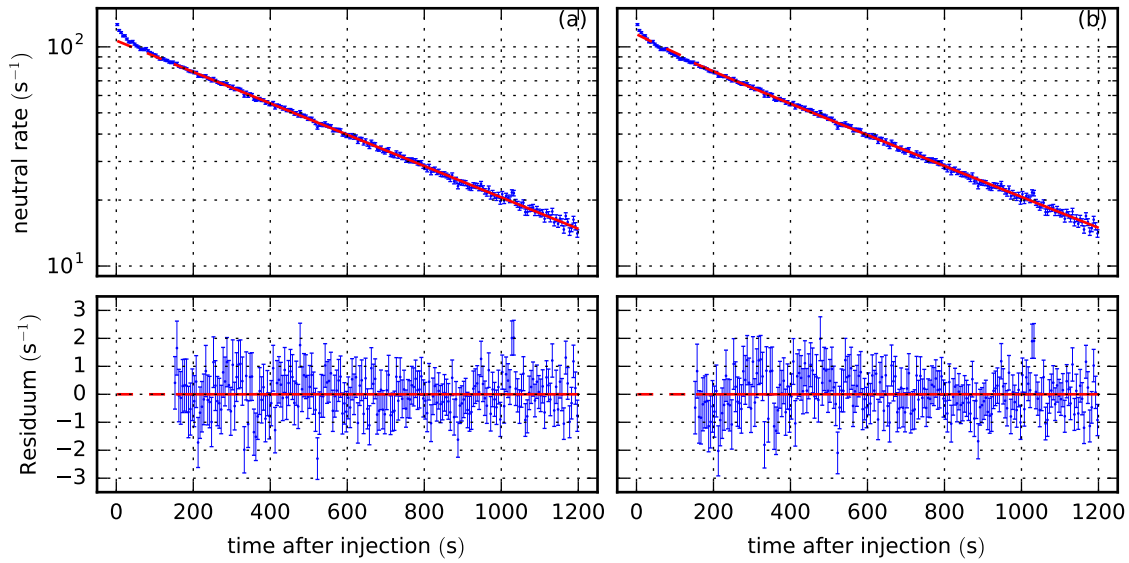

Figure 5.2: In the upper two diagrams the neutral rate induced by the helium neon laser is plotted against the time after injection into the CSR. The data is fitted by a mono-exponential (a) and bi-exponential decay (b) (see equation 5.8) after 150 s (solid red line), giving lifetimes of $\tau_{life}^{mono} = 607.0(1.8)$ s (a) and $\tau_{life}^{bi} = 617.0(1.8)$ s (b). The two plots below show the residua of the fits.

represented by the laser intensity normalization $b \approx 3$ (see equation 4.8). The relative cross sections used in this thesis are already normalized to the cross section σ_r at the helium neon laser line. The laser wavelength of the OPO laser are cycled during injection. Thus, the state-dependent cross sections $\sigma_J(\tilde{\nu}) = \sum_{T,J=J''} \sigma_{T(J'')}(\tilde{\nu})$ (see equation 3.31) are averaged over the applied wavenumbers weighted by their measurement time. Thus, the depletion in the rotational state J is expressed by

$$k_J^{\mathrm{OPO}} = \sigma_J^{mean} \frac{\Phi(\tilde{\nu})}{\Phi(\tilde{\nu}_r)} k_L^{\mathrm{HeNe}}, \tag{5.5}$$

where σ_J^{mean} represents the wavelength average cross section normalized to σ_r. These rates k_J^{OPO} are used to approximate the systematic shift induced by differential laser depletion (see equation 5.18).

5.1.3 Rotational cross section variations

The helium neon laser photodetaches the OH^- anion high above the EA. Thus, state-dependent cross sections are predicted to vary less than 10^{-3} (see section 3.2.4). Hence, the rotational population distribution should not affect the rate induced by

the helium neon laser. To verify this assumption one searches for an additional decay process at the reference wavenumber $\tilde{\nu}_r$.

The neutral rate induced by the helium neon laser is given by

$$R(\tilde{\nu}_r, t) = \sigma_J^{tot}(\tilde{\nu}_r)\frac{N_T(t)}{V_T} l\Phi(\tilde{\nu}_r) \text{ (see equation 4.2).} \tag{5.6}$$

The total cross section $\sigma_J^{tot}(\tilde{\nu}_r)$ is the sum over all state-dependent cross sections $\sigma_J(\tilde{\nu}_r) = \sum_{T,J=J''} \sigma_{T(J'')}(\tilde{\nu})$ weighted by their population distribution P_J. The overlap length l, the photon flux $\Phi(\tilde{\nu}_r)$ and the target volume V_T are assumed to be constant over the measurement time. Thus, the helium neon laser induces a rate

$$R(\tilde{\nu}_r, t) \propto N_T(t) \sum_J \sigma_J(\tilde{\nu}_r) P_J(t), \tag{5.7}$$

which is proportion to the total number of ions in the target volume N_T. Furthermore a linear dependence between the ions in the target volume N_T and the ions in the ring N_{ions} is predicted ($N_T \propto N_{ions}$) (see section 5.1.1).

If all cross sections $\sigma_J(\tilde{\nu}_r) = \sigma_r$ are equal, the sum $\sum_J \sigma_J(\tilde{\nu}_r) P_J(t) = \sigma_r$ is independent of the population. Thus, the photon-induced rate $R(\tilde{\nu}_r, t)$ at the reference wavenumber $\tilde{\nu}_r$ shows the time decay of $N_{ion}(t)$. Hence, the equality of the cross sections at the reference wavenumber $\tilde{\nu}_r$ is tested by searching for additional dynamics in the decay of the rate $R(\tilde{\nu}_r, t)$. The cooling of the two lowest rotational states are modeled by analytically solving the differential equation 2.67 for a two state model after $t_0 = 150$ s. After 150 s storage time all higher rotational states are considered to be negligible (see figure 2.6(b)). Then the photodetachment rate at the reference wavelength is described by

$$R_r(t) \propto e^{-k_{life}t}(1 + ae^{-(k_{1\to0}+k_{0\to1})(t-t_0)}) \tag{5.8}$$

$$a = \frac{(k_{1\to0}P_1(t_0) - k_{0\to1}P_0(t_0))(\sigma_1(\tilde{\nu}_r) - \sigma_0(\tilde{\nu}_r))}{\sigma_0(\tilde{\nu}_r)k_{1\to0} + \sigma_1(\tilde{\nu}_r)k_{0\to1}}, \tag{5.9}$$

where $P_J(t_0)$ is the population in state J at $t_0 = 150$ s and $k_{J\to J'}$ are the radiative transition rates (see section 2.4). From the global fit (see figure 4.9) of the photodetachment signals one derives the decay rates $k_{1\to0} = 5.32 \cdot 10^{-3}$ s^{-1} and $k_{0\to1} = 0.45 \cdot 10^{-3}$ s^{-1} and the start populations $P_0(t_0) = 0.46$ and $P_1(t_0) = 0.54$ at $t_0 = 150$ s. By altering the problem parameter a the quality factor χ^2 of the bi-exponential fit is changed (see figure 5.2). In the 1σ confidence region the problem parameter a can vary up to $2.9 \cdot 10^{-2}$. Thus, the relative difference

$$\left|\frac{\sigma_0(\tilde{\nu}_r) - \sigma_1(\tilde{\nu}_r)}{\sigma_0(\tilde{\nu}_r)}\right| = \left|1 - \frac{k_{1\to0}P_1(t_0) - k_{0\to1}P_0(t_0) + k_{1\to0}a}{k_{1\to0}P_1(t_0) - k_{0\to1}P_0(t_0) - k_{0\to1}a}\right| \tag{5.10}$$

between the relative cross sections of $J = 0$ and $J = 1$ has to be smaller than 6.4%. This result agrees with previous measurements [40] and the photodetachment model (see section 3.2.4).

Assuming a relative cross section difference of 6.4%, the measured beam lifetime would change to $\tau_{life}^{bi} = 617.0(1.8)$ s (see figure 5.2). Hence, the fitted radiative cooling rates of the OH^- molecule would systematically shift by the rate

$$k_{life}^{sys} = \Delta k = \left| \frac{1}{\tau_{life}^{bi}} - \frac{1}{\tau_{life}} \right| = 2.670(11)\ 10^{-5}\,\mathrm{s}^{-1} \tag{5.11}$$

This decay rate affects the measurement of the longest rotational radiative lifetime $\tau_{J=1}$. Hence, a maximal systematic shift of

$$\frac{k_{life}^{sys}}{k_{1\to 0}} < \frac{k_{sys}}{A_{1\to 0}} \approx 0.6\% \tag{5.12}$$

is predicted due to normalization by the reference rate.

In section 5.1.1 the lifetime of the OH^- ion beam in the CSR is revealed. Additionally an upper limit for the laser depletion rates is given, which is important for understanding systematic effects on rotational lifetimes (see equation 5.18). Furthermore state-dependent cross sections at the reference wavenumber $\tilde{\nu}_r$ for the lowest two rotational states are identical regarding precision (6.4%). Thus, the longest rotational lifetime can maximally shift by 0.6% due to normalization imperfections.

5.2 Experimental effects in the photodetachment signal

In the photodetachment signals (see figure 4.9) two experimental effects are observed. The background in the rate ratio is far above the intrinsic detector noise, which is explained by photodetachment of $^{17}O^-$ atoms (see section 5.2.1). Furthermore an unexpected high rate ratio in the steady state of S_5 is found, which can not result from a population in the rotational state $J = 2$. In section 5.2.2 this effect is explained by reflected laser light which crosses the ion beam in opposing direction.

5.2.1 $^{17}O^-$ beam contamination

The photodetachment signals S_i in figure 4.9 reveal a background rate ratio of $(0.46 \cdots 1.92) \cdot 10^{-2}$ which all signals S_i for $i > 4$ cool down to. Since every signal S_i combines different fractions of rotational states, the background is independent of the internal excitation of the OH^- molecule, but is far above the intrinsic detector

noise. Instead the background is explained by laser-induced photodetachment of O^-.

The $^{17}O^-$ anion has nearly the same charge-to-mass ratio as the OH^- ion. Thus, the oxygen isotope $^{17}O^-$ can not be separated from the OH^- by the 90° magnetic dipole benders in the transportation beam line to the CSR. Hence, an OH^- ion beam with a contamination of $^{17}O^-$ is injected into the CSR. The abundance of O^- in the stored ion beam depends on the production efficiency ϵ_p of O^- to OH^- and on the natural abundance $a_{^{17}O} = 0.038$ % of ^{17}O neglecting the transportation efficiency. To estimate the production efficiency $\epsilon_p \approx 10$ the intensity ratio of mass 16 u to 17 u is measured after the first dipole bender. Thus, an O^- contamination of around 0.38 % is predicted in the stored OH^- ion beam. The O^- contamination can alter between the runs, since ion source parameters and beam line settings might affect the ratio between O^- and OH^- in the stored ion beam.

The O^- atoms inside the ring are photodetached at a photon frequency which is high above the EA $\tilde{\nu} = 11785$ cm^{-1} [61]. Thus, theory [95] and experiment [9, 49] predict a rather constant cross section in the small probing range of the OPO laser. Thus, the neutralized rate induced by the OPO laser is independent of its used wavenumber. To estimate the abundance of O^- in the OH^- beam by the cross sections the background rate ratio is divided by the laser intensity normalization $b \approx 3$ (see equation 4.8). Hence, one gets a photodetachment reference rate ratio for the background of $(0.13 \cdots 0.45) \cdot 10^{-2}$. An O^- abundance of $(1.7 \cdots 5.9) \cdot 10^{-3}$ is calcuted by taking into account that the cross section of O^- around the reference photon energy 1.95 eV (15751 cm^{-1}) is by a factor 0.75 smaller than the one of the OH^- [40]. Thus, the predicted contamination of 0.38% lies perfectly in the calculated range.

To verify the O^- contamination the OPO laser is tuned stepwise to the EA of the oxygen atom in a separate run. Shortly above the wavenumber 11785 cm^{-1} [7] a strong decrease in the photodetachment signal is observed.

5.2.2 Reflected laser beam correction

The laser light enters and exits the experimental chambers in CSR through sapphire windows (see figure 4.2). If the laser hits the windows at the exit in a perfect 90° angle, the reflected light hits the ion beam against its propagating direction. Hence, the ions observe a reflected light frequency, which is Doppler shifted by about 40 cm^{-1} to higher instead of to lower photon energies (see equation 4.5). Thus, the wavenumber of the reflected laser beam is about 80 cm^{-1} higher in the ion rest frame than the normal laser light (see figure 5.3).

The total cross section high above the EA varies slowly with the photon energy. Thus, the neutral rate induced by the helium neon laser is not significantly affected.

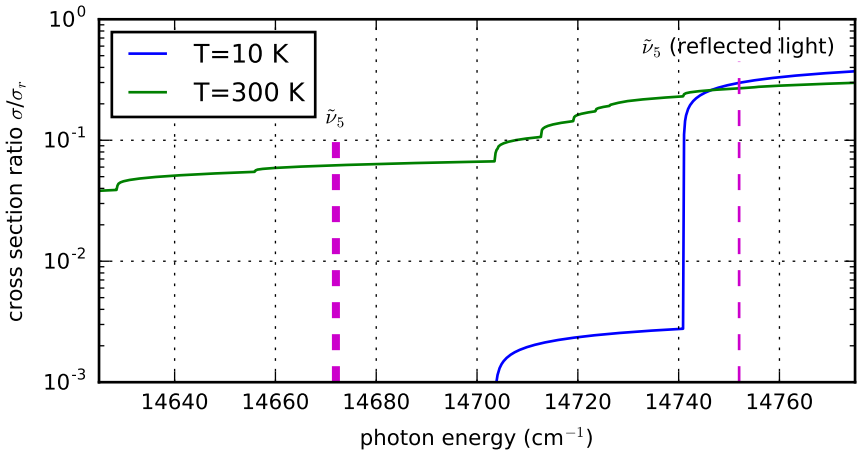

Figure 5.3: The photodetachment spectrum is shown for 10 K and 300 K thermal population distribution. For a cold rotational distribution the cross section for the reflected and normal laser light differs over several orders of magnitude. For a broader spectral overview see also figure 3.6.

But near the photodetachment threshold even photon frequency shifts of about 80 cm^{-1} can drastically change the total cross section (see figure 5.3). The photon energy $\tilde{\nu}_5$ used for the rate ratio S_5 can normally only detach the rotational states $J \geq 2$. But the reflected light can neutralize all rotational levels $J \geq 0$. Due to the large differences in the population of states the total cross section can vary over several orders of magnitude (see figure 5.3). If reflections in the range of some per mill up to several percent are considered, the background at the rate ratio S_5 can be explained by reflected light photodetachment.

To disregard a population in state $J = 2$ the consistency of the population hierarchy in the steady state is checked. If the background in signal S_5 results from a population in state $J = 2$, the photodetachment signals S_5, S_4 and S_3 in run 121 reveal a steady state population of

$$P_0 = 0.907,\ P_1 = 0.061 \text{ and } P_2 = 0.032. \tag{5.13}$$

Here the modeled cross sections are applied (see section 3.2). The corresponding photon occupation numbers $n_{\tilde{\nu}_{0\to1}} = 0.023$ and $n_{\tilde{\nu}_{1\to2}} = 0.461$ are revealed by applying equation 2.71. Hence, the photon occupation number would increase with the photon energy, if the steady state in the signal S_5 is explained by population in the rotational level $J = 2$. But the Bose-Einstein statistics is a monotonically decreasing function (see equation 2.12). Thus, no set of thermal radiators can induce such a behavior. The modeled cross sections are maybe incorrect. But Otto *et al* have shown that their description is quite well near the photodetachment threshold [65]. Hence, the background in S_5 does not arise from a population in the $J = 2$.

Thus, the background in S_5 is explained by an additional rate induced by reflected light. The relative cross section matrix $\hat{\sigma}$ is modeled for the positively Doppler shifted wavenumbers, folded with the population distribution and added to the fit function by a reflection factor R (see equation 4.10). Two fitted reflection factors, one $R_1 = 3.53(7)$ for run 108 and 109 and one $R_2 = 0.64(3)$ for all other runs, are sufficient to describe the steady state signal S_5 in all runs. Interestingly the fitted reflection factors R_i changed, when the laser setup was newly aligned. This is a clear indication that the background in S_5 strongly depends on the angle and position of the laser beam.

The position at which the reflected laser beam hits the ion beam varies with the angle between the laser and the window. Since the time-of-flight spectrum reflects the reaction position in the overlap region (see figure 4.4), the small acceptance time window for the pulsed induced counts limits the measured photodetachment reactions to a rather small range in the experimental section. Thus, the resulting rate induced by the reflected light is decreased with deviation from the perfect 90° reflection angle. Hence, the time correlation between counts and laser suppresses stray and reflected light effects in the OPO-induced neutral rates.

5.3 Radiative cooling of rotational states

This section deals with the main result of this thesis: the radiative lifetimes of rotational states (see table 5.4). To reveal them absorption and stimulated emission processes induced by the radiative field have to be considered. Thus, the radiative field is discussed in subsection 5.3.1. Here the fit results are compared to the temperature determined by the modeled cross section. Subsection 5.3.2 analyzes the radiative rotational cooling. The measured cooling rates of OH^- can be shifted by various effects. Thus, in section 5.3.3 the systematic uncertainties on radiative lifetimes are discussed. In section 5.3.4 the rotational lifetimes are analyzed by comparing their corresponding dipole moments to theoretical calculations.

5.3.1 Radiation field

The radiative steady state in the CSR depends only on the photon occupation number (see equation 2.71). Hence, the photodetachment signals are analyzed at storage times $t_{st} > 900$ s at which the rate ratios can be assumed to be constant (see figure 4.9). The photodetachment signals for S_i for $i > 4$ are ignored, since they reflect either the O^- background in the OH^- ion beam (see section 5.2.1) or the additional photodetachment by the reflected laser beam (see section 5.2.2). Thus, a significant amount of population is only found in the two lowest rotational levels.

Thus, the photon field in the CSR is measured by the population ratio P_1/P_0 at a photon frequency $\tilde{\nu}_{0\to1} = 37.48$ cm^{-1}. The modeled cross sections are applied

to estimate the populations $P_0 = 0.902$ and $P_1 = 0.098$ as well as the population ratio $P_1/P_0 = 0.109$. Hence, a photon occupation number of $n_{\tilde{\nu}_{0\to1}} = 0.038$ is revealed corresponding to an effective temperature of $T_{\mathrm{CSR}} = 16.1$ K. These estimated values deviate about 10 σ from the fitted results at a rotational start population temperature of $T_0 = 6000$ K:

$$P_0 = 0.922(2),\ P_1 = 0.078(2),\ P_1/P_0 = 0.085(2),\ n_{\tilde{\nu}_{0\to1}} = 0.0291(9)$$
$$\text{and } T_{\mathrm{eff}} = 15.1(1) \text{ K}. \tag{5.14}$$

Thus, the modeled cross sections already seem to be a good approximation, but radiative rotational cooling increases the precision. A start population variation from 6000 K to 4000 K changes the effective rotational temperature T_{eff} by 0.03 K. Thus, systematic effects due to the start population can be neglected.

In the steady state both methods reveal more than 90% population in the rotational ground state of OH^-. Hence, the CSR provides an environment which is suitable to conduct experiments under conditions comparable to interstellar clouds. The observed radiative temperature in the OH^- experiment agrees also with the results found in the CH^+ experiment [62].

The effective radiative temperature $T_{\mathrm{eff}} = 15.1(1)$ K determined in this thesis deviates from the temperature $T_{\mathrm{CSR}} = 6$ K at the experimental chambers of the CSR. The temperature difference is explained by 300 K radiation entering the CSR in the injection. Thus, an effective radiation field is considered consisting of a 6 K n_6 and a 300 K n_{300} radiation field. The effective field is given by

$$n_{\tilde{\nu}} = \epsilon_6 n_6 + \epsilon_{300} n_{300}, \tag{5.15}$$

where $\epsilon_6 = 1 - \epsilon_{300}$ and ϵ_{300} describe the thermal fractions of the radiation field. Equation 5.15 is an equivalent description of equation 2.2. A small fraction of $\epsilon_{300} = 5.7(2) \cdot 10^{-3}$ leads to an increase of 9.1(1) K in the measured internal temperature (see table 5.1). The thermal fractions reflect the ratio of the radiation surfaces in the CSR arrangement in the year 2015. For a CSR circumference of $l_{\mathrm{CSR}} = 35$ m

Table 5.1: Photon occupation numbers at the lowest rotational transition frequency $\tilde{\nu}_{0\to1} = 37.47$ cm^{-1} of OH^- for black body radiation fields at different temperatures

Temperature (K)	$n_{\tilde{\nu}_{0\to1}}$	Symbol
6.0	1.252×10^{-4}	n_6
15.1(1)	$2.91(9) \times 10^{-2}$	n
300.0	5.079	n_{300}

the opening for the 300 K radiation has a diameter of roughly 20 cm, which is in the order of the beam tube diameter in the injection.

Interestingly a similar measurement at DESIREE in Stockholm [75] shows no effect of 300 K radiation. The cold ion bender at the injection seems to prevent hot radiation from entering the storage ring. By closing the injection beam line, e.g. with a cold iris, the ions inside the CSR can cool down to even lower temperatures.

5.3.2 Radiative cooling

While the OH^- ions circulate inside the CSR they radiatively cool to the lowest rotational levels in a stepwise behavior. Thus, the rotational state J cools faster than the next lower one $J-1$ (see section 2.4). Hence, the photodetachment signals which address only the highly excited rotational levels ($J \geq 4$) decay faster (see figure 4.9). After 10 s significant population is only left over in the lowest four rotational states. Since the signals S_7 and S_6 cool down to the O^- background (see section 5.2.1), the radiative field intensity at the transition frequency $\tilde{\nu}_{2\to3} = 111.3\ \mathrm{cm}^{-1}$ from $J = 2$ to $J = 3$ can be disregarded. Thus, the exponential decay rate after 10 s in S_6 reveals directly the Einstein coefficient for spontaneous emission $A_{3\to2} = 0.1767(41)\ \mathrm{s}^{-1}$ (see figure 5.4). Hence, the transition dipole moment in the vibrational ground state is given by $d_{J=3} = 0.959(11)$ D (see equation 2.51).

If the rotational state J is significantly populated in the steady state, the observed

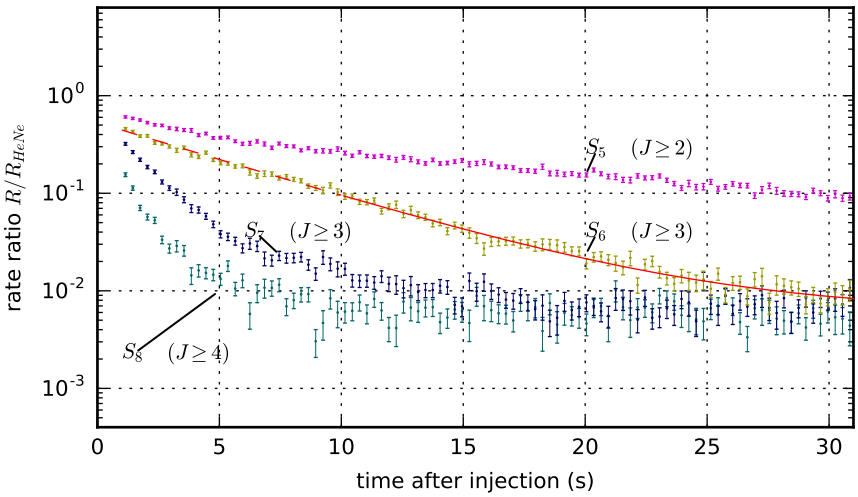

Figure 5.4: The signals of run 123 of figure 4.9 are displayed including an exponential fit at the rate ratio S_6 after 10 s (red line). A lifetime of $\tau_{J=3} = 5.66(3)$ s for the rotational state $J = 3$ is revealed. The background for the fit is determined separately.

exponential decay of the state J is approximately accelerated by the corresponding photon occupation number $n_{\tilde{\nu}_{J-1\to J}}$ (see equation 2.74). Hence, the measured exponential decay rates reveal an upper limit for the radiative lifetimes. The observed decay of the rotational state $J = 1$ into $J = 0$ is faster than the corresponding Einstein coefficient of spontaneous emission. Thus, the exponential decays are corrected by radiative field effects to determine the Einstein coefficients. Therefore all runs are fitted simultaneously by a numerical cooling model including the O^- background and the reflected light correction (see equation 4.10). But the rotational start population is unknown. Thus, the fitted data are limited to suitable time ranges (see section 4.4.2).

After 10 s three types of radiative decays are observed in the photodetachment signal (see figure 4.9) corresponding to the decay of the rotational states $J = 3$, $J = 2$ and $J = 1$. Thus, the Einstein coefficients for the three lowest excited states are fitted. Cooling of highly excited states ($J \geq 4$) are modeled by the dipole moment in the rotational level $J = 3$ by applying equation 2.15. Here the frequency broadening of the absorption lines (see section 2.1.4) and the change of the dipole moment with the rotational state (see section 2.3.2) are disregarded. But those assumptions do not significantly affect the results. The fitted lifetimes for the rotational state $J = 3$, $J = 2$ and $J = 1$ are given in table 5.2.

5.3.3 Systematic effects on radiative lifetimes

Especially long lifetimes measured by exponential decays are sensitive to systematic effects in many cases. Thus, this sections deals with systematic uncertainties on radiative decay rates.

Frequency precision of the measurement clock: A simple way to change the exponential decay rate is a frequency shift in the measurement clock. A frequency change in the measurement clock would result in stretching or compression of the time axis. Thus, the measured radiative decay rates are shifted accordingly. To

Table 5.2: Einstein coefficients $A_{J\to J-1}$, radiative lifetimes τ_J and the corresponding dipole moment d_0 of the three lowest rotational states in OH^- including their 1σ statistical uncertainties.

	$J = 1$	$J = 2$	$J = 3$	unit
$A_{J\to J-1}$	$0.00517(7)_{\text{stat}}$	$0.0478(15)_{\text{stat}}$	$0.189(6)_{\text{stat}}$	s^{-1}
$\tau_J = A^{-1}_{J\to J-1}$	$193(3)_{\text{stat}}$	$20.9(7)_{\text{stat}}$	$5.30(16)_{\text{stat}}$	s
d_0	$0.970(6)_{\text{stat}}$	$0.952(15)_{\text{stat}}$	$0.997(15)^a_{\text{stat}}$	D

[a] value for all rotational states $J \geq 3$

quantify the frequency stability the time delay between the measurement clock in the Field Programmable Gateway Array and the time server at the MPIK is measured by the Network Time Protocol (NTP). This measurement results in a time shift of $5 \cdot 10^{-6}$ s in 1 s. The NTP's precision is limited to several microseconds. Hence, the result gives an upper limit for the time shift generated by the measurement clock. The Einstein coefficients are proportional to the radiative decay rates. Thus, the relative time uncertainty of $5 \cdot 10^{-6}$ coincides with the systematic shift induced in the radiative lifetimes.

Hence, the systematic uncertainties generated by the measurement clock are negligible in comparison to the statistical uncertainties of 1.3% for $A_{1\to0}$ and 3% for $A_{J\to J-1}$ with $J \in \{2, 3\}$ (see table 5.2).

Starting temperature: The fit of the photodetachment signals begins at a storage time of 10 s to start at a well-defined population distribution. Thus, the fitted values should be independent of the start population. But still some effects of the start temperature T_0 remain.

The excluded points in the photodetachment signals are best described by the model using a start temperature of $T_0 = 6000$ K (upper limit of the grey shaded areas in figure 4.9). To quantify the systematic shift a start temperature variation of about 2000 K is assumed. Thus, the photodetachment signals are also fitted at a $T_0 = 4000$ K start population. The resulting shift in the fit values determines the systematic uncertainty. The start population variation yields a small relative systematic effect of below 0.1% for $A_{J\to J-1}$ with $J \in \{1, 2\}$ and of 0.15% for $A_{3\to2}$. Comparing the statistical uncertainties of 1.3% for $A_{1\to0}$ and 3% for $A_{J\to J-1}$ with $J \in \{2, 3\}$ (see table 5.2) the start temperature uncertainty can be neglected.

Electronic deflection fields:
To monitor the radiative cooling of the OH^- ensemble the ions are stored in an electrostatic cryogenic storage ring. Thus, the OH^- molecules observe an electric field in the ion deflectors. Due to the Stark effect the electric field mixes the rotational states and changes the population distribution. To bend the 60 keV OH^- beam in the CSR an electric field strength of $F = 120$ kV/m is applied. The interaction between the neighboring states $|J, M\rangle$ and $|J-1, M\rangle$ induced by the Stark effect depends on the dipole moment $d \approx 1$ D of the molecule and the energy splitting $|E_{J+1} - E_J| \approx 2B$ of the two states. The mixture amplitude between to neighboring rotational states is given by [20]

$$|\epsilon_J^M| = \frac{dF}{|E_{J+1} - E_J|} \frac{\sqrt{J^2 - M^2}}{\sqrt{(2J^2+1)(2J^2-1)}} \lesssim \frac{dF}{2|E_{J+1} - E_J|}. \tag{5.16}$$

With the interaction energy of $dF = 2.5 \cdot 10^{-6}$ eV a maximal admixture amplitude of $|\epsilon_J^M| \lesssim 3 \cdot 10^{-4}$ is calculated. Thus, additional decay channels are smaller by a

factor of $|\epsilon_J^M|^2 \lesssim 1 \cdot 10^{-7}$. As a result, the electrostatic storage of the ion beam does not significantly effect the radiative cooling and steady state population of the OH^- ensemble.

Differential laser depletion: The laser beam neutralized a small fraction of the stored ion beam in the CSR. Thereby the laser beam reduces the number of stored ions. If all rotational states are depleted at the same rate the population distribution of the OH^- ensemble is not affected by laser probing (see section 2.4.1). But the OPO laser induces a rotational state-dependent depletion rate

$$\left.\frac{dN_J}{dt}\right|_{\mathrm{OPO}} = k_J^{\mathrm{OPO}} N_J, \tag{5.17}$$

where k_J^{OPO} is described by equation 5.5. Thus, the laser-induced rate at the rotational population $P_J = N_J / \sum_i N_i$ is given by

$$\begin{aligned}\left.\frac{dP_J}{dt}\right|_{\mathrm{OPO}} &= \frac{1}{\sum_i N_i}\frac{dN_J}{dt} + \frac{N_J}{(\sum_i N_i)^2}\sum_i \frac{dN_i}{dt} \\ &= P_J\left(k_J^{\mathrm{OPO}} + \sum_i k_i^{\mathrm{OPO}}\right) \\ &= P_J \sum_i P_i \left(k_J^{\mathrm{OPO}} - k_i^{\mathrm{OPO}}\right) = P_J k_J^{sat}.\end{aligned} \tag{5.18}$$

The resulting decay rate k_J^{sat} depends on the rate difference $\Delta k_{i,J}^{\mathrm{OPO}} = k_J^{\mathrm{OPO}} - k_i^{\mathrm{OPO}}$ and the population of all other states.

The photodetachment signals are fitted after 10 s storage time. Thus, only the lowest four states are significantly populated. Since the sum over all populations is per definition 1, the maximal absolute rate difference $|\Delta k_{i,J}^{\mathrm{OPO}}|$ for $i \in \{0,\ 1,\ 2,\ 3\}$

Table 5.3: Systematic uncertainties of radiative lifetimes induced by differential laser depletion

	run number		
	109	121	125
$\Delta A_{1\to0}^{sys,rel}$	$4.6 \cdot 10^{-3}$	$9.8 \cdot 10^{-3}$	$8.8 \cdot 10^{-3}$
$\Delta A_{2\to1}^{sys,rel}$	$4.2 \cdot 10^{-4}$	$1.6 \cdot 10^{-3}$	$9.2 \cdot 10^{-4}$
$\Delta A_{3\to2}^{sys,rel}$	$1.4 \cdot 10^{-4}$	$2.8 \cdot 10^{-4}$	$2.4 \cdot 10^{-4}$

gives an upper limit for the absolute value of the differential depletion rate

$$\begin{aligned} \left|k_J^{sat}\right| &= \left|\sum_{i=0}^{3} P_i \left(k_J^{\mathrm{OPO}} - k_i^{\mathrm{OPO}}\right)\right| \\ &\leq \max_i \left|k_J^{\mathrm{OPO}} - k_i^{\mathrm{OPO}}\right| \text{ for } i \in \{0,\ 1,\ 2,\ 3\}. \end{aligned} \tag{5.19}$$

Normalizing the maximum absolute value of $|k_J^{sat}|$ to the corresponding Einstein coefficient $A_{J\to J-1}$ reveals an upper limit for the systematic uncertainty due to differential laser depletion. Depending on the run different sets of wavenumbers are applied (see figure 4.9). Thus, the differential depletion rates k_J^{sat} vary with each run. For the three longest runs 109, 121 and 125 the upper limits are given in table 5.3. Considering the statistical uncertainty of 1.3% for $A_{1\to 0}$ and 3% for $A_{J\to J-1}$ with $J \in \{2, 3\}$ (see table 5.2) differential laser depletion is only taken into account for the longest rotational lifetime with a systematic uncertainty of 1%.

5.3.4 Rotational lifetimes

The lifetimes of the rotational states have statistical uncertainties of 1.3% for $A_{1\to 0}$ and 3% for $A_{J\to J-1}$ with $J \in \{2, 3\}$ (see table 5.2). Thus, systematic effects of the measurement clock, the start temperature and the electrostatic deflection fields are neglected. The maximal systematic shift by differential laser depletion of 1.0% is considered for the lowest rotational excited state. The J-dependence of the cross section σ_r at the reference wavenumber $\tilde{\nu}_r$ is taken into account for all states. For the transition from $J = 1$ to $J = 0$ a maximum effect of 0.6% is revealed in section 5.1.3. The J-dependence of the cross sections for all higher states is considered to be less than 10% [40]. This leads to a systematic uncertainty of 1%. Altogether an uncertainty of 2.9% for $A_{1\to 0}$ and 4% for $A_{J\to J-1}$ with $J \in \{2, 3\}$ is revealed (see table 5.4).

To my best knowledge, those are the first direct measurements of natural lifetimes on the lowest rotationally excited states [54]. Shortly after, the research group in

Table 5.4: Einstein coefficients $A_{J\to J-1}$, radiative lifetimes τ_J and the corresponding dipole moments d_0 of the three lowest rotational states in OH^- including their 1σ statistical and systematic uncertainties.

	$J = 1$	$J = 2$	$J = 3$	unit
$A_{J\to J-1}$	$0.00517(7)_{\mathrm{stat}}(8)_{\mathrm{sys}}$	$0.0478(15)_{\mathrm{stat}}(4)_{\mathrm{sys}}$	$0.189(6)_{\mathrm{stat}}(2)_{\mathrm{sys}}$	s^{-1}
$\tau_J = A_{J\to J-1}^{-1}$	$193(3)_{\mathrm{stat}}(3)_{\mathrm{sys}}$	$20.9(7)_{\mathrm{stat}}(1)_{\mathrm{sys}}$	$5.30(16)_{\mathrm{stat}}(6)_{\mathrm{sys}}$	s
d_0	$0.970(6)_{\mathrm{stat}}(8)_{\mathrm{sys}}$	$0.952(15)_{\mathrm{stat}}(4)_{\mathrm{sys}}$	$0.997(15)^{a}_{\mathrm{stat}}(5)_{\mathrm{sys}}$	D

[a] value for all rotational states $J \geq 3$

Stockholm reported lifetimes for the lowest excited level in OH^- of 145(28) s [75], which agrees with our value in a 2σ uncertainty range. At the given accuracy, the molecular dipole moments extracted from the Einstein coefficients of spontaneous emission $A_{J\to J-1}$ assuming the elementary Hönl-London factors (see equation 2.61) are compatible among each other within experimental uncertainties. Hence, effects of rotational excitation described by the Herman-Wallis factor can not be resolved (see section 2.3.2). Thus, the weighted average of $d_0 = 0.971(10)$ D is compared to calculations of the OH^- dipole moment. At the equilibrium internuclear distance the theoretical dipole moment is given by 1.050 to 1.072 D in earlier [90] and 1.10 D in recent work [84]. To get an effective dipole moment in the ground state the dipole moment is vibrationally averaged over the dipole moment function of [90]. Thereby the dipole moment is reduced by at most 0.31 D to $d_0 = 1.041$ D (see section 2.3.2). Thus, the current theory overestimates the OH^- dipole moment by about $(7 \pm 1)\%$ and underestimates the OH^- rotational lifetimes by about $(14 \pm 2)\%$.

5.4 State-resolved photodetachment cross sections

In addition to radiative lifetimes the fitting of the photodetachment signals also reveal the state-resolved or state-dependent cross sections. The concept which leads to the resolving power of the data is described in section 5.4.1. Futhermore the resulting cross sections are analyzed for measurement uncertainties and compared to the modeled photodetachment cross sections in figure 3.5 (see section 5.4.2).

5.4.1 State decay correlation

The total photodetachment cross section (see equation 3.32) is a linear combination of the population distribution folded with state-dependent cross sections. Thus, the shape of the photodetachment spectrum depends also on the internal temperature of the molecular ensemble. Hence, the cross section for the individual rotational state can not be resolved without knowing the population distribution. Thus, the correlation between the rotational excitation and the radiative decay rate is used to reveal the population distribution.

The Einstein coefficient is proportional to the cubic of the energy splitting between the rotational levels which increases roughly linearly with the rotational excitation (see section 2.33). Thus, the radiative lifetime of a rotational state decreases with the internal energy of the OH^- molecule. Hence, each rotational level has its own radiative decay rate into the steady state. Since the transition dipole moment varies slowly with the rotational excitation (see figure 2.5), the lifetime of all rotational levels can be predicted by one measured Einstein coefficient (see equation 2.61).

Due to the strong correlation between the rotational excitation and the radiative decay rate the population distribution can be fitted by the cooling dynamics in the photodetachment signals S_k (see figure 4.9).

The cross section ratio between the rotational ground and the first excited state is directly observable at the rate ratios S_1, S_2 and S_3 (see figure 4.9). At those wavenumbers $\tilde{\nu}_{1,2,3}$ all rotational states can be photodetached. Thus, the addressed part of the population distribution stays constant independent of the rotational cooling. After around 150 s storage time the OH^- ensemble is assumed to be in a two state system. While the population cools down from $J = 1$ to $J = 0$, the photodetachment signals S_1 and S_3 increase. Thus, the photodetachment cross section in the rotational state $J = 1$ must be lower than in the ground state. In the same way one can argue that the cross sections for the lowest two states in the photodetachment signal S_2 have to be roughly equal.

In a nutshell the population distribution can be revealed by using the state decay correlation in photodetachment signals over time. Hence, rotational cooling can determine state-dependent, relative photodetachment cross sections.

5.4.2 Cross section ratios

In this thesis the state-dependent cross section can be revealed due to the correlation between the rotational excitation and the radiative decay rate (see section 5.4.1). These cross sections are molecular properties which are independent of the internal excitation of the molecular ensemble. Thus, all rate ratios in figure 4.9 are fitted simultaneously to reveal the state dependent cross section (see section 4.4.2). Since relative cross sections are measured, one non-zero state-dependent cross section has to be fixed to its modeled value. For the fit stability it is crucial to choose a cross section, which is nearly independent of the applied start population. Thus, the cross section of the photodetachment signal S_3 detaching the rotational state $J = 0$ is chosen (see fixed value in table 4.4.2).

To calibrate the rate ratio to the photon flux of the OPO laser (see equation 4.4) the laser energy at the applied wavelength is measured after the experiment (see table 4.1). If the rate ratios are normalized directly, the 3% uncertainty of the laser power measurement would also increase the uncertainty of the radiative lifetime measurement. To avoid that the modeled cross sections are normalized to the corresponding photon flux before the fit process. To reveal the state-dependent cross sections the fitted values in the cross section matrix $\hat{\sigma}$ are scaled back. Thus, the 3% systematic uncertainty of the laser power measurement is included in the state-dependent cross section values by Gaussian error propagation. To yield the systematic uncertainty the shift between the fitted values at 6000 K and 4000 K start temperature is calculated and separately given in table 5.5. In figure 5.5 the systematic and statistical uncertainties are added. The measurement values for the

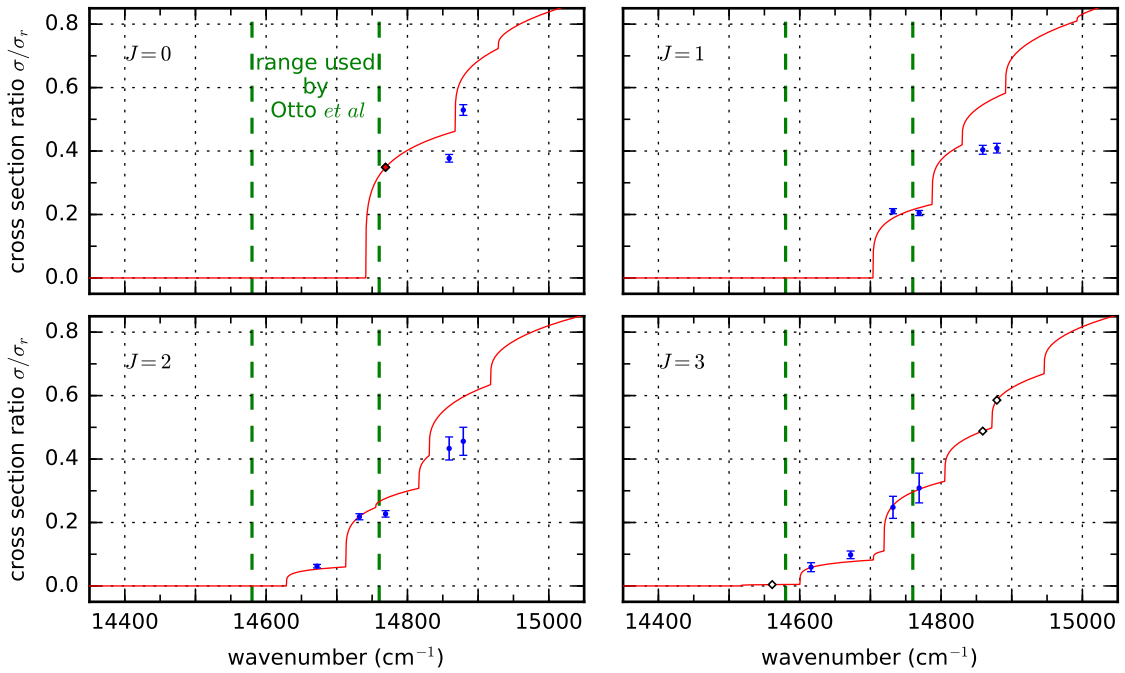

Figure 5.5: Fitted values of near-threshold photodetachment cross section ratios $\sigma(\tilde{\nu}_k)/\sigma_r$ (blue points) of OH^- at the probing wavenumbers $\tilde{\nu}_k$ are compared to the empirical model with the exponents $a = 0.2$ and $b = -2.8$ (full lines) (see table 5.5). The error bars include the 1σ statistical and the systematic uncertainty induced by an unknown start population distribution (see section 4.4.2). The open diamonds mark modeled values for the cross section ratios at the probing lines, where radiative cooling can not disentangle the population contribution. The reference value is assigned by a red filled diamond.

state-dependent cross section are compared to the model (see section 3.2.3) in table 5.5 and figure 5.5.

With more electron energy than 12.4 meV (100 cm^{-1}) the empirical theoretical model for the cross sections starts to fail (see figure 5.5). Also the change of the common exponent of the thresholds does not increase the overall agreement between the modeled and the experimental cross section. The experimental result calls for more detailed cross section calculations beyond the simple threshold model, e.g. including higher moments. Only close to the threshold including the wavelength range used by Otto *et al* [65] the model agrees with our experimental data. Thus, the measured values for the state-dependent cross sections can be applied as an independent basis for future thermometry measurements with OH^-. This will serve ion trap experiments to study cold inelastic collisions like [34, 65]. Furthermore

OH^- may be a candidate to proof anionic laser cooling in the future, where an experimental cross section basis is preferable.

Table 5.5: Measured relative photodetachment cross sections for the rotational states at the probing wavenumbers $\tilde{\nu}_k$ are presented including their 1σ statistical and relevant systematic uncertainty. The measured values for the state-dependent cross sections normalized to the cross section σ_r at the helium neon laser line are plotted in figure 5.5. If no systematic uncertainty is given, it can be neglected in comparison to the 1σ statistical uncertainty. Theoretical predictions are given for comparison.

OPO laser		cross section ratio $\sigma_J(\tilde{\nu}_k)/\sigma_r$							
		$J=0$		$J=1$		$J=2$		$J=3$	
k	$\tilde{\nu}_k$ (cm^{-1})	Exp.	Model	Exp.	Model	Exp.	Model	Exp.	Model
1	14879	$1.52(5)_{\text{stat}}$	1.82	$1.17(4)_{\text{stat}}$	1.64	$1.31(12)_{\text{stat}}$	1.71		1.68
2	14859	$1.08(4)_{\text{stat}}$	1.31	$1.16(4)_{\text{stat}}$	1.57	$1.24(10)_{\text{stat}}$	1.63		1.40
3	14769	1.00^a		$0.587(21)_{\text{stat}}(2)_{\text{sys}}$	0.635	$0.651(29)_{\text{stat}}(1)_{\text{sys}}$	0.791	$0.89(12)_{\text{stat}}(2)_{\text{sys}}$	0.874
4	14732		0	$0.603(20)_{\text{stat}}(3)_{\text{sys}}$	0.541	$0.626(25)_{\text{stat}}(2)_{\text{sys}}$	0.629	$0.71(9)_{\text{stat}}(1)_{\text{sys}}$	0.728
5	14672		0		0	$0.179(11)_{\text{stat}}(5)_{\text{sys}}$	0.152	$0.281(24)_{\text{stat}}(11)_{\text{sys}}$	0.220
6	14616		0		0		0	$0.170(27)_{\text{stat}}(13)_{\text{sys}}$	0.167
7	14561		0		0		0		0.0124
8	14495		0		0		0		0

[a] Reference value ($\sigma_{J=0}(\tilde{\nu}_3)/\sigma_r = 0.3488$)

6 Summary and conclusion

In contrast to atoms molecules can store energy in their internal degrees of freedom. In many cases vibrational and rotational excited states are significantly populated at room temperature. Thus, cross section measurements on room temperature molecules are averaged over the population distribution. In this thesis a method has been presented to disentangle the rotational population distribution of the OH^- molecule to reveal the state-dependent relative cross sections and radiative lifetimes of rotational states.

Radiative lifetimes of excited states are normally determined by measuring their exponential decay like in the S^- experiment at DESIREE [3]. Although the OH^- ions are stored in a cryogenic environment, the residual photon field shifts the spontaneous radiative decay by absorption and stimulated emission. Thus, it is essential to know the radiative field or the steady state population distribution (see equation 2.14) to determine the lifetime of a rotational state. Hence, population measurements are crucial to disentangle physical effects.

Otto *et al* [65] revealed the rotational population distribution of a helium buffer gas cooled OH^- ensemble in a 22-pole trap by measuring the photodetachment spectrum. But the state-dependent, relative cross sections have to be modeled to predict the internal excitation of the OH^- molecule. We followed a different approach. The radiative lifetime of a rotational state decreases with the internal excitation of a molecule. Hence, the cooling rate of the OH^- molecule is coupled with its internal energy. The rotational population distribution is revealed by monitoring the change in photodetachment signals close to the EA by the radiative decay of the populations. The concept of using decay rate variations to quantify the internal energy has also been used in cluster physics and on carbon chain molecules playing a fundamental role in astrochemistry. For example the internal energy in Co_4^- clusters is determined by monitoring the destruction decay of the photon-excited system [13]. Furthermore, a low lying electronic state in C_6^- has been detected by observing the dynamics in the photon-excited state [43]. Strong variations of the decay rate with the internal energy can be found in many quantum systems. Thus, this method of determining the population seems to be a promising approach to study radiative processes in infrared-active molecules.

Absorption and stimulated emission of photons have to be suppressed to observe the strong dependence between the rotational excitation and the radiative decay rate in the OH^- molecule (see figure 2.6). Thus, the OH^- molecule is stored in

an electrostatic cryogenic storage ring. Those devices provide a collision-free environment with a low radiative background in which infrared-active molecules can radiatively cool down to their lowest quantum states (see section 1.6). Furthermore the electrostatic design inhibits rotational state mixing by the Zeeman effect, which in some cases can alter the radiative lifetime of an excited state [93].

The rotational cooling of the OH^- ensemble in the CSR is probed by near-threshold photodetachment. Close to the EA the photodetachment spectrum depends on the rotational population distribution (see figure 3.6). Thus, the contributing fractions of the rotational states change by tuning the laser wavelength. This effect has been first employed by Otto *et al* [65]. To model the cross section Otto *et al* scan the fine structure thresholds to reveal the energy dependence of photodetachment transitions experimentally, since sophisticated calculations are needed to determine the threshold law in this case. But in this thesis the population distribution is revealed by the radiative cooling of the rotational states. Thus, only 8 wavenumbers close to the photodetachment transitions are sufficient to probe the whole cooling process at a storage time longer than 10 s (see figure 4.9). Hence, this thesis concentrates on the time dynamics of the photodetachment signals, which is measured up to 20 min.

To measure the rotational cooling the photodetachment rates have to be corrected for ion loss processes during the storage time. In contrast to room-temperature devices the ion beam decay can often not be monitored by residual gas collisions. Thus, a second laser at a wavelength high above the EA is introduced. The photodetachment rates measured near-threshold are normalized by the signal high above the EA. The resulting rate ratios are calibrated to the number of ions in the overlap region and are directly proportional to the relative cross section (see equation 4.4). Thus, this method is robust against ion density fluctuations. The rate ratios (see figure 4.9) can be described in a very good agreement (reduced mean squared residuals $\chi^2_{red} = 1.30$) with our combined probing and cooling model. Thereby radiative lifetimes, rotational-state-dependent cross sections and photon occupation numbers are revealed.

The photon occupation number for the lowest transition in OH^- corresponds to an effective temperature of $T_{\text{eff}} = 15.1(1)$ K, which is far from the temperature $T_{\text{CSR}} \approx 6$ K measured at the experimental chambers of the CSR. Thus, the radiative field in the CSR can not be described by a black body radiator. But other rotational cooling measurements in Stockholm at DESIREE predict a thermal radiation field with a temperature of $\sim 13.4(2)$ K [75]. In contrast to the present setup at the CSR, ions are injected in DESIREE over an already cold deflector. Thus, 300 K radiation can not directly enter the cryogenic environment. Small leaks of room-temperature radiation lead to drastic changes in the radiation field (see figure 2.2). Hence, the amount of $a_{300\text{ K}} = 0.57(2)\%$ at 300 K radiation heats up the OH^- molecule from 6 K to an effective temperature of 15 K (see section 5.3.1). Nev-

ertheless, even in the present arrangement the CSR reduces the radiation field in the experimental chambers significantly allowing to cool infrared-active molecules to their lowest rotational states.

Due to the long storage times in the cryogenic environment of the CSR radiative lifetimes of the lowest rotational states can be measured (see table 5.4). For the lowest excited state a lifetime of $193(3)_{\mathrm{stat}}(3)_{\mathrm{sys}}$ s is revealed [54]. Within the errors, this agrees with a later measurement in Stockholm at DESIREE [75]. Effects of rotational excitation on the resulting transition dipole moments have not been found in our data. Thus, a mean transition dipole moment in the vibrational ground state of 0.971(10) D is defined, which is about $(7 \pm 1)\%$ off the closest theoretical value, 1.041 D [90]. Even recent calculations do not fit with the experimental results in this thesis [84]. Hence, line strength calculations for rotational transitions with a higher precision than $\sim 10\%$ should take into account theoretical uncertainties. Transition strengths for rotational transitions are applied in interstellar spectroscopy analysis.

Especially the additional electron in anions bound by electron correlations challenges the theories. The extra electron in OH^- changes the bound length by less than $\Delta r_e < 0.02$ Å [14, 18], but drastically decreases the calculated dipole moments in the vibrational ground states from 1.65 D in OH to 1.04 D in OH^- [90]. Thus, the electron configuration in the shell has a large impact on the transition dipole moment in OH^-. As a result, radiative lifetimes of rotational states in OH^- are good quantities to test electron correlations in models. Furthermore the Einstein coefficients for pure rotational transition measure the permanent dipole moment of the molecule, while vibrational transitions depend on the change of the dipole moment along the internuclear axis. Thus both transition dipole moments can differ largely.

The measurement of Otto *et al* [65] has shown that the temperature of the OH^- anion in some cases deviates from the temperature of the coolant, although the OH^- molecule should be in equilibrium with the helium buffer gas. This effect can result from micromotion in the 22-pole trap or from erroneously predicted state-dependent cross sections. The measured state-dependent cross section (see table 5.5) can serve as a basis to exclude modeling errors from photodetachment thermometry with OH^- molecules. This method has been applied for measuring rotational-state-changing inelastic collisions [34].

Excluding the measurement of CH^+ [62], this thesis presents to my knowledge the first method to measure the photon energy density of the radiative field in a cryogenic storage device. Here the photon field is only determined at the lowest transition frequency $\tilde{\nu} = 37.48$ cm^{-1} of the OH^- molecule. But the method in this thesis can be applied to future photodetachment measurements to reveal photon occupation numbers at other wavenumbers. To disentangle the population distribution the anionic molecules should cool to the steady state during the storage time and

their level structure has to be very well known. Especially the first condition limits the molecular species to light hydrides such as OD^-, SH^- and SD^-. But this method can also be applied to molecules with an open shell like NH^-, although the complex level structure challenges the experiment. For example the photon energy density in the radiative field can be measured with OD^- by slightly changing the probing wavenumbers of the OPO laser. The OD^- molecule ($B_0 = 9.99$ cm^{-1} [78]) has a higher spectral density of rotational transitions than OH^- ($B_0 = 18.74$ cm^{-1}) (see also figure 2.3). Thus, the photodetachment measurement of OD^- will reveal the photon energy densities at multiple wavenumbers. In the future such photodetachment measurements can be used to search for radiation field variations in cryogenic storage devices by changes in the experimental setup.

Photodetachment can only be applied to anions, but also infrared-active cations such as CH^+ radiatively cool in the CSR. The population ratios of OH^- have been determined by the coupling between the rotational excitation and the radiative decay rate, which results from the transition energy dependence of the Einstein coefficients and the rotational level structure. Thus, this coupling can also be utilized for cations. Hence, any reaction, whose cross section spectrum varies with the rotational excitation of the molecule, can be used to reveal the population distribution and to measure state-resolved reaction cross sections. Cross section variations have been observed in an electron recombination measurement for vibrationally cooling HD^+ in the Test Storage Ring at the MPIK in Heidelberg [27]. Especially state-resolved cross sections of electron recombination measurements for the lowest molecular states can contribute to a better understanding of interstellar chemistry.

As a result, the OH^- experiment in this thesis paves the way to state-resolved and population-independent results in probing measurements of rotationally cooling molecules in a radiatively dominated environment.

List of Figures

List of Tables

Bibliography

[1] M. Agúndez, J. Cernicharo, M. Guélin, C. Kahane, E. Roueff, J. Kłos, F. J. Aoiz, F. Lique, N. Marcelino, J. R. Goicoechea, M. G. García, C. A. Gottlieb, M. C. McCarthy, and P. Thaddeus, "Astronomical identification of CN^-, the smallest observed molecular anion", *Astronomy & Astrophysics* **517** (2010), p. L2, DOI: 10.1051/0004-6361/201015186.

[2] K. Anton, S. L. Kaufman, W. Klempt, G. Moruzzi, R. Neugart, E. Otten, and B. Schinzler, "Collinear Laser Spectroscopy on Fast Atomic Beams", *Physical Review Letters* **40** (1978), p. 642, DOI: 10.1103/PhysRevLett.40.642.

[3] E. Bäckström, D. Hanstorp, O. M. Hole, M. Kaminska, R. F. Nascimento, M. Blom, M. Björkhage, A. Källberg, P. Löfgren, P. Reinhed, S. Rosén, A. Simonsson, R. D. Thomas, S. Mannervik, H. T. Schmidt, and H. Cederquist, "Storing keV Negative Ions for an Hour: The Lifetime of the Metastable $^2P^o_{1/2}$ level in $^{32}S^-$", *Physical Review Letters* **114** (2015), p. 143003, DOI: 10.1103/PhysRevLett.114.143003.

[4] J. Bernard, G. Montagne, R. Brédy, B. Terpend-Ordacière, A. Bourgey, M. Kerleroux, L. Chen, H. T. Schmidt, H. Cederquist, and S. Martin, "A "table-top" electrostatic ion storage ring: Mini-Ring", *Review of Scientific Instruments* **79** (2008), p. 075109, DOI: 10.1063/1.2957609.

[5] P. F. Bernath, *Spectra of Atoms and Molecules*, 2nd ed., Oxford University Press, New York, 2005, 439 pp.

[6] C. Blondel, "Recent experimental achievements with negative ions", *Physica Scripta* **1995** (1995), p. 31, DOI: 10.1088/0031-8949/1995/T58/004.

[7] C. Blondel, W. Chaibi, C. Delsart, C. Drag, F. Goldfarb, and S. Kröger, "The electron affinities of O, Si, and S revisited with the photodetachment microscope", *The European Physical Journal D - Atomic, Molecular, Optical and Plasma Physics* **33** (2005), p. 335, DOI: 10.1140/epjd/e2005-00069-9.

[8] S. N. Bose, "Plancks Gesetz und Lichtquantenhypothese", *Zeitschrift für Physik* **26** (1924), p. 178, DOI: 10.1007/BF01327326.

[9] L. M. Branscomb, S. J. Smith, and G. Tisone, "Oxygen Metastable Atom Production Through Photodetachment", *The Journal of Chemical Physics* **43** (1965), p. 2906, DOI: 10.1063/1.1697230.

[10] L. M. Branscomb, "Photodetachment Cross Section, Electron Affinity, and Structure of the Negative Hydroxyl Ion", *Physical Review* **148** (1966), p. 11, DOI: 10.1103/PhysRev.148.11.

[11] L. M. Branscomb, D. S. Burch, S. J. Smith, and S. Geltman, "Photodetachment Cross Section and the Electron Affinity of Atomic Oxygen", *Physical Review* **111** (1958), p. 504, DOI: 10.1103/PhysRev.111.504.

[12] L. M. Branscomb and S. J. Smith, "Experimental Cross Section for Photodetachment of Electrons from H^- and D^-", *Physical Review* **98** (1955), p. 1028, DOI: 10.1103/PhysRev.98.1028.

[13] C. Breitenfeldt, "Cooling of anionic metal clusters stored in an electrostatic ion beam trap", PhD thesis, Ernst-Moritz-Arndt-Universität Greifswald, 2016.

[14] F. Breyer, P. Frey, and H. Hotop, "High resolution photoelectron spectrometry of negative ions: Rotational transitions in laser-photodetachment of OH^-, SH^-, SD^-", *Zeitschrift für Physik A Atoms and Nuclei* **300** (1981), p. 7, DOI: 10.1007/BF01412609.

[15] J. M. Brown, J. T. Hougen, K.-P. Huber, J. W. C. Johns, I. Kopp, H. Lefebvre-Brion, A. J. Merer, D. A. Ramsay, J. Rostas, and R. N. Zare, "The labeling of parity doublet levels in linear molecules", *Journal of Molecular Spectroscopy* **55** (1975), p. 500, DOI: 10.1016/0022-2852(75)90291-X.

[16] A. Cable, M. Prentiss, and N. P. Bigelow, "Observations of sodium atoms in a magnetic molasses trap loaded by a continuous uncooled source", *Optics Letters* **15** (1990), p. 507, DOI: 10.1364/OL.15.000507.

[17] L. D. Carr, D. DeMille, R. V. Krems, and J. Ye, "Cold and ultracold molecules: science, technology and applications", *New Journal of Physics* **11** (2009), p. 055049, DOI: 10.1088/1367-2630/11/5/055049.

[18] R. J. Celotta, R. A. Bennett, and J. L. Hall, "Laser photodetachment determination of the electron affinities of OH, NH_2, NH, SO_2, and S_2", *The Journal of Chemical Physics* **60** (1974), p. 1740, DOI: 10.1063/1.1681268.

[19] R. J. Celotta, R. A. Bennett, J. L. Hall, M. W. Siegel, and J. Levine, "Molecular Photodetachment Spectrometry. II. The Electron Affinity of O_2 and the Structure of O_2^-", *Physical Review A* **6** (1972), p. 631, DOI: 10.1103/PhysRevA.6.631.

[20] Y.-P. Chang, F. Filsinger, B. G. Sartakov, and J. Küpper, "CMIstark: Python package for the Stark-effect calculation and symmetry classification of linear, symmetric and asymmetric top wavefunctions in dc electric fields", *Computer Physics Communications* **185** (2014), p. 339, DOI: 10.1016/j.cpc.2013.09.001.

[21] J. Deiglmayr, A. Göritz, T. Best, M. Weidemüller, and R. Wester, "Reactive collisions of trapped anions with ultracold atoms", *Physical Review A* **86** (2012), p. 043438, DOI: 10.1103/PhysRevA.86.043438.

[22] J. Doyle, B. Friedrich, R. V. Krems, and F. Masnou-Seeuws, "Quo vadis, cold molecules?", *The European Physical Journal D - Atomic, Molecular, Optical and Plasma Physics* **31** (2004), p. 149, DOI: 10.1140/epjd/e2004-00151-x.

[23] M. Drewsen and A. Brøner, "Harmonic linear Paul trap: Stability diagram and effective potentials", *Physical Review A* **62** (2000), p. 045401, DOI: 10.1103/PhysRevA.62.045401.

[24] M. A. van Eijkelenborg, M. E. M. Storkey, D. M. Segal, and R. C. Thompson, "Sympathetic cooling and detection of molecular ions in a Penning trap", *Physical Review A* **60** (1999), p. 3903, DOI: 10.1103/PhysRevA.60.3903.

[25] F. O. Ellison, "Intensities of Vibrational and Rotational Spectra of Charged Diatomic Molecules", *The Journal of Chemical Physics* **36** (1962), p. 478, DOI: 10.1063/1.1732535.

[26] P. C. Engelking, "Strong electron-dipole coupling in photodetachment of molecular negative ions: Anomalous rotational thresholds", *Physical Review A* **26** (1982), p. 740, DOI: 10.1103/PhysRevA.26.740.

[27] P. Forck, M. Grieser, D. Habs, A. Lampert, R. Repnow, D. Schwalm, A. Wolf, and D. Zajfman, "Dissociative recombination of cold HD^+ at the Test Storage Ring", *Physical Review Letters* **70** (1993), p. 426, DOI: 10.1103/PhysRevLett.70.426.

[28] D. Gerlich and M. Smith, "Laboratory astrochemistry: studying molecules under inter- and circumstellar conditions", *Physica Scripta* **73** (2006), p. C25, DOI: 10.1088/0031-8949/73/1/N05.

[29] S. Gewurtz, H. Lew, and P. Flainek, "The Electronic Spectrum of HF^+", *Canadian Journal of Physics* **53** (1975), p. 1097, DOI: 10.1139/p75-139.

[30] F. Goldfarb, C. Drag, W. Chaibi, S. Kröger, C. Blondel, and C. Delsart, "Photodetachment microscopy of the P, Q, and R branches of the OH^-(v=0) to OH(v=0) detachment threshold", *The Journal of Chemical Physics* **122** (2005), p. 014308, DOI: 10.1063/1.1824904.

[31] M. Grieser, R. von Hahn, S. Vogel, and A. Wolf, "The phase slip factor of the electrostatic cryogenic storage ring CSR", *Journal of Physics: Conference Series* **874** (2017), p. 012049, DOI: 10.1088/1742-6596/874/1/012049.

[32] R. von Hahn, A. Becker, F. Berg, K. Blaum, C. Breitenfeldt, H. Fadil, F. Fellenberger, M. Froese, S. George, J. Göck, M. Grieser, F. Grussie, E. A. Guerin, O. Heber, P. Herwig, J. Karthein, C. Krantz, H. Kreckel, M. Lange, F. Laux, S. Lohmann, S. Menk, C. Meyer, P. M. Mishra, O. Novotný, A. P. O'Connor, D. A. Orlov, M. L. Rappaport, R. Repnow, S. Saurabh, S. Schippers, C. D. Schröter, D. Schwalm, L. Schweikhard, T. Sieber, A. Shornikov, K. Spruck, S. Sunil Kumar, J. Ullrich, X. Urbain, S. Vogel, P. Wilhelm, A. Wolf, and D. Zajfman, "The cryogenic storage ring CSR", *Review of Scientific Instruments* **87** (2016), p. 063115, DOI: 10.1063/1.4953888.

[33] H. Haken and H. C. Wolf, *Molekülphysik und Quantenchemie - Einführung in die experimentellen und theoretischen Grundlagen*, 5th ed., Springer-Verlag Berlin Heidelberg, 2006, 531 pp.

[34] D. Hauser, S. Lee, F. Carelli, S. Spieler, O. Lakhmanskaya, E. S. Endres, S. S. Kumar, F. Gianturco, and R. Wester, "Rotational state-changing cold collisions of hydroxyl ions with helium", *Nature Physics* **11** (2015), p. 467, DOI: 10.1038/nphys3326.

[35] A. N. Heays, N. de Oliveira, B. Gans, K. Ito, S. Boyé-Péronne, S. Douin, K. M. Hickson, L. Nahon, and J. C. Loison, "High-resolution one-photon absorption spectroscopy of the $D^2\Sigma^- \rightarrow X^2\Pi$ system of radical OH and OD", *Journal of Quantitative Spectroscopy and Radiative Transfer* **204** (2018), p. 12, DOI: 10.1016/j.jqsrt.2017.08.021.

[36] W. Heisenberg, "Über den anschaulichen Inhalt der quantentheoretischen Kinematik und Mechanik", *Zeitschrift für Physik* **43** (1927), p. 172, DOI: 10.1007/BF01397280.

[37] G. Herzberg, *Molecular Spectra and Molecular Structure*, 2nd ed., vol. I. Spectra of Diatomic Molecules, Krieger Publishing Company, Malabar, Florida, 1950, 660 pp.

[38] E. Hill and J. H. Van Vleck, "On the Quantum Mechanics of the Rotational Distortion of Multiplets in Molecular Spectra", *Physical Review* **32** (1928), p. 250, DOI: 10.1103/PhysRev.32.250.

[39] R. K. Hinkley, J. A. Hall, T. E. H. Walker, and W. G. Richards, "Λ doubling in $^2\Pi$ states of diatomic molecules", *Journal of Physics B: Atomic and Molecular Physics* **5** (1972), p. 204, DOI: 10.1088/0022-3700/5/2/016.

[40] P. Hlavenka, R. Otto, S. Trippel, J. Mikosch, M. Weidemüller, and R. Wester, "Absolute photodetachment cross section measurements of the O^- and OH^- anion", *The Journal of Chemical Physics* **130** (2009), p. 061105, DOI: 10.1063/1.3080809.

[41] H. Hotop, T. A. Patterson, and W. C. Lineberger, "High-Resolution Photodetachment Study of Se^- Ions", *Physical Review A* **8** (1973), p. 762, DOI: 10.1103/PhysRevA.8.762.

[42] H. Hotop, T. A. Patterson, and W. C. Lineberger, "High resolution photodetachment study of OH^- and OD^- in the threshold region 7000-6450 Å", *The Journal of Chemical Physics* **60** (1974), p. 1806, DOI: 10.1063/1.1681279.

[43] G. Ito, T. Furukawa, H. Tanuma, J. Matsumoto, H. Shiromaru, T. Majima, M. Goto, T. Azuma, and K. Hansen, "Cooling Dynamics of Photoexcited C_6^- and C_6H^-", *Physical Review Letters* **112** (2014), p. 183001, DOI: 10.1103/PhysRevLett.112.183001.

[44] R. Johansson, *Python package for calculating wavefunctions for 1D and 2D potentials*, original-date: 2013-03-11T04:47:48Z, 2017, URL: https://github.com/jrjohansson/wavefunction (visited on 09/17/2017).

[45] C. J. Johnson, B. B. Shen, B. L. J. Poad, and R. E. Continetti, "Photoelectron-photofragment coincidence spectroscopy in a cryogenically cooled linear electrostatic ion beam trap", *Review of Scientific Instruments* **82** (2011), p. 105105, DOI: 10.1063/1.3641875.

[46] B. Kern, D. Strelnikov, P. Weis, A. Böttcher, and M. M. Kappes, "IR Absorptions of C_{60}^+ and C_{60}^- in Neon Matrixes", *The Journal of Physical Chemistry A* **117** (2013), p. 8251, DOI: 10.1021/jp4054605.

[47] C. Krantz, O. Novotný, A. Becker, S. George, M. Grieser, R. von Hahn, C. Meyer, S. Schippers, K. Spruck, S. Vogel, and A. Wolf, "Single-particle detection of products from atomic and molecular reactions in a cryogenic ion storage ring", *Nuclear Instruments and Methods in Physics Research Section A: Accelerators, Spectrometers, Detectors and Associated Equipment* **851** (2017), p. 92, DOI: 10.1016/j.nima.2017.01.050.

[48] M. Lange, M. Froese, S. Menk, J. Varju, R. Bastert, K. Blaum, J. R. C. López-Urrutia, F. Fellenberger, M. Grieser, R. von Hahn, O. Heber, K.-U. Kühnel, F. Laux, D. A. Orlov, M. L. Rappaport, R. Repnow, C. D. Schröter, D. Schwalm, A. Shornikov, T. Sieber, Y. Toker, J. Ullrich, A. Wolf, and D. Zajfman, "A cryogenic electrostatic trap for long-time storage of keV ion beams", *Review of Scientific Instruments* **81** (2010), p. 055105, DOI: 10.1063/1.3372557.

[49] L. C. Lee and G. P. Smith, "Photodissociation and photodetachment of molecular negative ions. VI. Ions in $O_2/CH_4/H_2O$ mixtures from 3500 to 8600 Å", *The Journal of Chemical Physics* **70** (1979), p. 1727, DOI: 10.1063/1.437690.

[50] J. P. Maillard, J. Chauville, and A. W. Mantz, "High-resolution emission spectrum of OH in an oxyacetylene flame from 3.7 to 0.9 μm", *Journal of Molecular Spectroscopy* **63** (1976), p. 120, DOI: 10.1016/0022-2852(67)90139-7.

[51] M. C. McCarthy, C. A. Gottlieb, H. Gupta, and P. Thaddeus, "Laboratory and Astronomical Identification of the Negative Molecular Ion C_6H^-", *The Astrophysical Journal Letters* **652** (2006), p. L141, DOI: 10.1086/510238.

[52] J. Meija, T. B. Coplen, M. Berglund, W. A. Brand, B. P. De, M. Gröning, N. E. Holden, J. Irrgeher, R. D. Loss, T. Walczyk, and T. Prohaska, "Atomic weights of the elements 2013 (IUPAC Technical Report)", *Pure and Applied Chemistry* **88** (2016), p. 265, DOI: 10.1515/pac-2015-0305.

[53] S. Menk, S. Das, K. Blaum, M. W. Froese, M. Lange, M. Mukherjee, R. Repnow, D. Schwalm, R. von Hahn, and A. Wolf, "Vibrational autodetachment of sulfur hexafluoride anions at its long-lifetime limit", *Physical Review A* **89** (2014), p. 022502, DOI: 10.1103/PhysRevA.89.022502.

[54] C. Meyer, A. Becker, K. Blaum, C. Breitenfeldt, S. George, J. Göck, M. Grieser, F. Grussie, E. A. Guerin, R. von Hahn, P. Herwig, C. Krantz, H. Kreckel, J. Lion, S. Lohmann, P. M. Mishra, O. Novotný, A. P. O'Connor, R. Repnow, S. Saurabh, D. Schwalm, L. Schweikhard, K. Spruck, S. Sunil Kumar, S. Vogel, and A. Wolf, "Radiative Rotational Lifetimes and State-Resolved Relative Detachment Cross Sections from Photodetachment Thermometry of Molecular Anions in a Cryogenic Storage Ring", *Physical Review Letters* **119** (2017), p. 023202, DOI: 10.1103/PhysRevLett.119.023202.

[55] R. Middleton, "A versatile high intensity negative ion source", *Nuclear Instruments and Methods in Physics Research* **214** (1983), p. 139, DOI: 10.1016/0167-5087(83)90580-X.

[56] S. P. Møller, "ELISA, and electrostatic storage ring for atomic physics", *Nuclear Instruments and Methods in Physics Research Section A: Accelerators, Spectrometers, Detectors and Associated Equipment* **394** (1997), p. 281, DOI: 10.1016/S0168-9002(97)00673-6.

[57] C. Monroe, W. Swann, H. Robinson, and C. Wieman, "Very cold trapped atoms in a vapor cell", *Physical Review Letters* **65** (1990), p. 1571, DOI: 10.1103/PhysRevLett.65.1571.

[58] E. A. Moore and W. G. Richards, "A Reanalysis of the $A^2\Sigma^+$ - $X^2\Pi_i$ System of OH", *Physica Scripta* **3** (1971), p. 223, DOI: 10.1088/0031-8949/3/5/005.

[59] R. S. Mulliken and A. Christy, "Λ-type doubling and electron configuration in diatomic molecules", *Physical Review* **38** (1931), p. 87, DOI: 10.1103/PhysRev.38.87.

[60] Y. Nakano, Y. Enomoto, T. Masunaga, S. Menk, P. Bertier, and T. Azuma, "Design and commissioning of the RIKEN cryogenic electrostatic ring (RICE)", *Review of Scientific Instruments* **88** (2017), p. 033110, DOI: 10.1063/1.4978454.

[61] D. M. Neumark, K. R. Lykke, T. Andersen, and W. C. Lineberger, "Laser photodetachment measurement of the electron affinity of atomic oxygen", *Physical Review A* **32** (1985), p. 1890, DOI: 10.1103/PhysRevA.32.1890.

[62] A. P. O'Connor, A. Becker, K. Blaum, C. Breitenfeldt, S. George, J. Göck, M. Grieser, F. Grussie, E. A. Guerin, R. von Hahn, U. Hechtfischer, P. Herwig, J. Karthein, C. Krantz, H. Kreckel, S. Lohmann, C. Meyer, P. M. Mishra, O. Novotný, R. Repnow, S. Saurabh, D. Schwalm, K. Spruck, S. Sunil Kumar, S. Vogel, and A. Wolf, "Photodissociation of an Internally Cold Beam of CH^+ Ions in a Cryogenic Storage Ring", *Physical Review Letters* **116** (2016), p. 113002, DOI: 10.1103/PhysRevLett.116.113002.

[63] S. M. O'Malley and D. R. Beck, "Lifetimes and branching ratios of excited states in La^-, Os^-, Lu^-, Lr^-, and Pr^-", *Physical Review A* **81** (2010), p. 032503, DOI: 10.1103/PhysRevA.81.032503.

[64] A. Ostendorf, C. B. Zhang, M. A. Wilson, D. Offenberg, B. Roth, and S. Schiller, "Sympathetic Cooling of Complex Molecular Ions to Millikelvin Temperatures", *Physical Review Letters* **97** (2006), p. 243005, DOI: 10.1103/PhysRevLett.97.243005.

[65] R. Otto, A. v. Zastrow, T. Best, and R. Wester, "Internal state thermometry of cold trapped molecular anions", *Physical Chemistry Chemical Physics* **15** (2013), p. 612, DOI: 10.1039/C2CP43186F.

[66] D. Pegg, "Photodetachment", *Springer Handbook of Atomic, Molecular, and Optical Physics*, Springer, New York, 2006, p. 891, DOI: 10.1007/978-0-387-26308-3_60.

[67] S. Petrie and E. Herbst, "Some Interstellar Reactions Involving Electrons and Neutral Species: Attachment and Isomerization", *The Astrophysical Journal* **491** (1997), p. 210, DOI: 10.1086/304941.

[68] M. Planck, "Ueber das Gesetz der Energieverteilung im Normalspectrum", *Annalen der Physik* **309** (1901), p. 553, DOI: 10.1002/andp.19013090310.

[69] E. L. Raab, M. Prentiss, A. Cable, S. Chu, and D. E. Pritchard, "Trapping of Neutral Sodium Atoms with Radiation Pressure", *Physical Review Letters* **59** (1987), p. 2631, DOI: 10.1103/PhysRevLett.59.2631.

[70] A. R. P. Rau and U. Fano, "Theory of Photodetachment near Fine-Structure Thresholds", *Physical Review A* **4** (1971), p. 1751, DOI: 10.1103/PhysRevA.4.1751.

[71] N. H. Rosenbaum, J. C. Owrutsky, L. M. Tack, and R. J. Saykally, "Velocity modulation laser spectroscopy of negative ions: The infrared spectrum of hydroxide OH^-", *The Journal of Chemical Physics* **84** (1986), p. 5308, DOI: 10.1063/1.449941.

[72] J. Sandström, G. Haeffler, I. Kiyan, U. Berzinsh, D. Hanstorp, D. J. Pegg, J. C. Hunnell, and S. J. Ward, "Effect of polarization on photodetachment thresholds", *Physical Review A* **70** (2004), p. 052707, DOI: 10.1103/PhysRevA.70.052707.

[73] S. Schippers, "Electron-ion merged-beam experiments at heavy-ion storage rings", *Nuclear Instruments and Methods in Physics Research Section B: Beam Interactions with Materials and Atoms* **350** (2015), p. 61, DOI: 10.1016/j.nimb.2014.12.050.

[74] S. Schlemmer, T. Kuhn, E. Lescop, and D. Gerlich, "Laser excited N_2^+ in a 22-pole ion trap: experimental studies of rotational relaxation processes", *International Journal of Mass Spectrometry* **185-187** (1999), p. 589, DOI: 10.1016/S1387-3806(98)14141-6.

[75] H. T. Schmidt, G. Eklund, K. C. Chartkunchand, E. K. Anderson, M. Kamińska, N. de Ruette, R. D. Thomas, M. K. Kristiansson, M. Gatchell, P. Reinhed, S. Rosén, A. Simonsson, A. Källberg, P. Löfgren, S. Mannervik, H. Zettergren, and H. Cederquist, "Rotationally Cold OH^- Ions in the Cryogenic Electrostatic Ion-Beam Storage Ring DESIREE", *Physical Review Letters* **119** (2017), p. 073001, DOI: 10.1103/PhysRevLett.119.073001.

[76] H. T. Schmidt, R. D. Thomas, M. Gatchell, S. Rosén, P. Reinhed, P. Löfgren, L. Brännholm, M. Blom, M. Björkhage, E. Bäckström, J. D. Alexander, S. Leontein, D. Hanstorp, H. Zettergren, L. Liljeby, A. Källberg, A. Simonsson, F. Hellberg, S. Mannervik, M. Larsson, W. D. Geppert, K. G. Rensfelt, H. Danared, A. Paál, M. Masuda, P. Halldén, G. Andler, M. H. Stockett, T. Chen, G. Källersjö, J. Weimer, K. Hansen, H. Hartman, and H. Cederquist, "First storage of ion beams in the Double Electrostatic Ion-Ring Experiment: DESIREE", *Review of Scientific Instruments* **84** (2013), p. 055115, DOI: 10.1063/1.4807702.

[77] H. T. Schmidt, H. Cederquist, J. Jensen, and A. Fardi, "Conetrap: A compact electrostatic ion trap", *Nuclear Instruments and Methods in Physics Research Section B: Beam Interactions with Materials and Atoms* **173** (2001), p. 523, DOI: 10.1016/S0168-583X(00)00415-8.

[78] P. A. Schulz, R. D. Mead, P. L. Jones, and W. C. Lineberger, "OH^- and OD^- threshold photodetachment", *The Journal of Chemical Physics* **77** (1982), p. 1153, DOI: 10.1063/1.443980.

[79] P. A. Schulz, R. D. Mead, and W. C. Lineberger, "Rotational intensities in photodetachment and photoionization", *Physical Review A* **27** (1983), p. 2229, DOI: 10.1103/PhysRevA.27.2229.

[80] E. S. Shuman, J. F. Barry, and D. DeMille, "Laser cooling of a diatomic molecule", *Nature* **467** (2010), p. 820, DOI: 10.1038/nature09443.

[81] M. W. Siegel, R. J. Celotta, J. L. Hall, J. Levine, and R. A. Bennett, "Molecular Photodetachment Spectrometry. I. The Electron Affinity of Nitric Oxide and the Molecular Constants of NO^-", *Physical Review A* **6** (1972), p. 607, DOI: 10.1103/PhysRevA.6.607.

[82] I. W. M. Smith, "Laboratory Astrochemistry: Gas-Phase Processes", *Annual Review of Astronomy and Astrophysics* **49** (2011), p. 29, DOI: 10.1146/annurev-astro-081710-102533.

[83] J. R. Smith, J. B. Kim, and W. C. Lineberger, "High-resolution threshold photodetachment spectroscopy of OH^-", *Physical Review A* **55** (1997), p. 2036, DOI: 10.1103/PhysRevA.55.2036.

[84] B. S. D. R. Vamhindi and M. Nsangou, "Accurate ab initio potential energy curves and spectroscopic properties of the low-lying electronic states of OH^- and SH^- molecular anions", *Molecular Physics* **114** (2016), p. 2204, DOI: 10.1080/00268976.2016.1191690.

[85] J. H. Van Vleck, "On σ-Type Doubling and Electron Spin in the Spectra of Diatomic Molecules", *Physical Review* **33** (1929), p. 467, DOI: 10.1103/PhysRev.33.467.

[86] S. Vogel, "Developments at an Electrostatic Cryogenic Storage Ring for Electron-Cooled keV Energy Ion Beams", PhD thesis, University Heidelberg, 2016.

[87] T. E. H. Walker, P. M. Dehmer, and J. Berkowitz, "Rotational band shapes in photoelectron spectroscopy: HF and DF", *The Journal of Chemical Physics* **59** (1973), p. 4292, DOI: 10.1063/1.1680624.

[88] C. W. Walter, N. D. Gibson, D. J. Matyas, C. Crocker, K. A. Dungan, B. R. Matola, and J. Rohlén, "Candidate for Laser Cooling of a Negative Ion: Observations of Bound-Bound Transitions in La^-", *Physical Review Letters* **113** (2014), p. 063001, DOI: 10.1103/PhysRevLett.113.063001.

[89] S. Watanabe and C. H. Greene, "Atomic polarizability in negative-ion photodetachment", *Physical Review A* **22** (1980), p. 158, DOI: 10.1103/PhysRevA.22.158.

[90] H. J. Werner, P. Rosmus, and E. A. Reinsch, "Molecular properties from MCSCF-SCEP wave functions. I. Accurate dipole moment functions of OH, OH^-, and OH^+", *The Journal of Chemical Physics* **79** (1983), p. 905, DOI: 10.1063/1.445867.

[91] R. Wester, "Radiofrequency multipole traps: tools for spectroscopy and dynamics of cold molecular ions", *Journal of Physics B: Atomic, Molecular and Optical Physics* **42** (2009), p. 154001, DOI: 10.1088/0953-4075/42/15/154001.

[92] E. P. Wigner, "On the Behavior of Cross Sections Near Thresholds", *Physical Review* **73** (1948), p. 1002, DOI: 10.1103/PhysRev.73.1002.

[93] A. Wolf, K. G. Bhushan, I. Ben-Itzhak, N. Altstein, D. Zajfman, O. Heber, and M. L. Rappaport, "Lifetime measurement of He^- using an electrostatic ion trap", *Physical Review A* **59** (1999), p. 267, DOI: 10.1103/PhysRevA.59.267.

[94] D. Zajfman, O. Heber, L. Vejby-Christensen, I. Ben-Itzhak, M. Rappaport, R. Fishman, and M. Dahan, "Electrostatic bottle for long-time storage of fast ion beams", *Physical Review A* **55** (1997), R1577, DOI: 10.1103/PhysRevA.55.R1577.

[95] O. Zatsarinny and K. Bartschat, "Low-energy photodetachment of O^-", *Physical Review A* **73** (2006), p. 022714, DOI: 10.1103/PhysRevA.73.022714.

My publications

[32] R. von Hahn, A. Becker, F. Berg, K. Blaum, C. Breitenfeldt, H. Fadil, F. Fellenberger, M. Froese, S. George, J. Göck, M. Grieser, F. Grussie, E. A. Guerin, O. Heber, P. Herwig, J. Karthein, C. Krantz, H. Kreckel, M. Lange, F. Laux, S. Lohmann, S. Menk, C. Meyer, P. M. Mishra, O. Novotný, A. P. O'Connor, D. A. Orlov, M. L. Rappaport, R. Repnow, S. Saurabh, S. Schippers, C. D. Schröter, D. Schwalm, L. Schweikhard, T. Sieber, A. Shornikov, K. Spruck, S. Sunil Kumar, J. Ullrich, X. Urbain, S. Vogel, P. Wilhelm, A. Wolf, and D. Zajfman, "The cryogenic storage ring CSR", *Review of Scientific Instruments* **87** (2016), p. 063115, DOI: 10.1063/1.4953888.

[47] C. Krantz, O. Novotný, A. Becker, S. George, M. Grieser, R. von Hahn, C. Meyer, S. Schippers, K. Spruck, S. Vogel, and A. Wolf, "Single-particle detection of products from atomic and molecular reactions in a cryogenic ion storage ring", *Nuclear Instruments and Methods in Physics Research Section A: Accelerators, Spectrometers, Detectors and Associated Equipment* **851** (2017), p. 92, DOI: 10.1016/j.nima.2017.01.050.

[54] C. Meyer, A. Becker, K. Blaum, C. Breitenfeldt, S. George, J. Göck, M. Grieser, F. Grussie, E. A. Guerin, R. von Hahn, P. Herwig, C. Krantz, H. Kreckel, J. Lion, S. Lohmann, P. M. Mishra, O. Novotný, A. P. O'Connor, R. Repnow, S. Saurabh, D. Schwalm, L. Schweikhard, K. Spruck, S. Sunil Kumar, S. Vogel, and A. Wolf, "Radiative Rotational Lifetimes and State-Resolved Relative Detachment Cross Sections from Photodetachment Thermometry of Molecular Anions in a Cryogenic Storage Ring", *Physical Review Letters* **119** (2017), p. 023202, DOI: 10.1103/PhysRevLett.119.023202.

[62] A. P. O'Connor, A. Becker, K. Blaum, C. Breitenfeldt, S. George, J. Göck, M. Grieser, F. Grussie, E. A. Guerin, R. von Hahn, U. Hechtfischer, P. Herwig, J. Karthein, C. Krantz, H. Kreckel, S. Lohmann, C. Meyer, P. M. Mishra, O. Novotný, R. Repnow, S. Saurabh, D. Schwalm, K. Spruck, S. Sunil Kumar, S. Vogel, and A. Wolf, "Photodissociation of an Internally Cold Beam of CH^+ Ions in a Cryogenic Storage Ring", *Physical Review Letters* **116** (2016), p. 113002, DOI: 10.1103/PhysRevLett.116.113002.

Danksagung

An dieser Stelle möchte ich mich bei allen bedanken, die mich in der Zeit meiner Doktorarbeit unterstützt haben.

Besonders danke ich Prof. Dr. Andreas Wolf für die Möglichkeit, über die ersten experimentellen Messungen am kalten Tieftemperatur-Speicherring promovieren zu dürfen. Die Diskussionen mit ihm über physikalische Probleme ermöglichte es mir neue Ideen und methodischen Verfahren zu entwickeln. Zudem wäre ohne seine Unterstützung eine so zügige Publikation der Ergebnisse der vorliegenden Arbeit nicht möglich gewesen.

Gleichfalls danke ich Prof. Dr. Matthias Weidemüller, dass er sich bereit erklärt hat, diese Doktorarbeit zu begutachten.

Dr. Sebastian George danke ich besonders für die jahrelange Betreuung und die detaillierten Anmerkungen zu meinen wissenschaftlichen Texten. Sein Vertrauen in meine freie Arbeitsweise hat mich stets ermutigt.

Meinem ehemaligen Bürokollegen Dr. Christian Breitenfeldt danke ich für die fachlichen Einweisungen in die physikalischen Experimente. Zusammen mit ihm und Jürgen Göck hatte ich zudem hilfreiche physikalische sowie erfrischende nichtwissenschaftliche Diskussionen. Felix Nüßlein danke ich für seine Unterstützung beim Laseraufbau und die alltägliche gegenseitige Kaffeezufuhr. Dem ganzem (ehemaligen und derzeitigen) CSR-Team unter der Leitung von Dr. Robert von Hahn, Prof. Dr. Klaus Blaum und Prof. Dr. Andreas Wolf möchte ich für die angenehme Arbeitsatmosphäre und erfolgreiche Zusammenarbeit danken.

Zudem danke ich meiner Freundin Julia und meiner Familie, die mich in meiner Promotionszeit begleitet, mit großem Interesse meine Arbeit verfolgt und auch mir in der einen oder anderen Situation Rückhalt gegeben haben.